NONLINEAR AVO INVERSION BASED ON ZOEPPRITZ EQUATIONS AND ITS APPLICATIONS

A Dissertation

by

UN YOUNG LIM

Submitted to the Office of Graduate and Professional Studies of
Texas A&M University
in partial fulfillment of the requirements for the degree of

DOCTOR OF PHILOSOPHY

Chair of Committee,	Richard L. Gibson, Jr.
Co-Chair of Committee,	Nurul Kabir
Committee Members,	Yuefeng Sun
	Hiroko Kitajima
	Michael King
Head of Department,	Michael Pope

August 2019

Major Subject: Geophysics

ABSTRACT

Amplitude Variation with Offset (AVO) inversion is an effective method to estimate elastic parameters of target subsurface layers. However, most conventional AVO inversions are based on linear approximations of Zoeppritz equations assuming weak contrasts and seismic isotropy. For this reason, conventional AVO inversions cannot correctly estimate elastic parameters of some geologically important formations (e.g., organic-rich shale, formations beneath salt-dome or carbonate, etc.) which are highly anisotropic and often surrounded by hard layers generating strong contrasts. To overcome this challenge, I apply a non-linear AVO inversion based on exact Zoeppritz solutions for seismic reflection amplitudes. In the dissertation, I will describe how the non-linear inversion can efficiently be implemented and how it can be beneficial for both conventional and unconventional reservoir characterization. Specifically, I will show inversion results applying the inversion with models that represent strong contrasts and strong anisotropy. Direct outputs of the inversion are three contrast parameters between overlying and underlying layers and one background values. However, with an assumption that the model parameters of the overlying (or underlying) layer are known, the proposed AVO inversion can accurately determine horizontal and vertical P-wave and S-wave velocities of target layers of the models. Therefore, seismic anisotropy of the models can also be determined. In addition, this inversion provides a benefit to differentiate density from acoustic impedance. Based on the results, I will propose a workflow to define geomechanical properties (i.e., Young's modulus and Poisson's ratio), and total organic carbon (TOC) content of target layers. Furthermore, I develop a new inversion method to improve the Zoeppritz AVO inversion by jointly using PP- and converted PS-seismic reflections together. This joint inversion provides better estimations of S-wave velocity, shear impedance and the ratio of background P-wave and S-wave velocities. Lastly, I apply the inversion into more complicate field seismic data in order to demonstrate the superiority of the method compared to linear inversions. With the given field example, I also introduce a new seismic attribute, ΔV_P, in order to more practically estimate seismic

anisotropy from real seismic data. The ΔV_P attribute is well correlated with values of gamma-ray (GR) log, which can assess the amount of shale contents and that should be highly correlated to seismic anisotropy. Therefore, the effectiveness of the attribute for inference of seismic anisotropy can indirectly be verified. In summary, the non-linear Zoeppritz AVO inversion provides better estimations of elastic parameters for such challenging situations: strong contrasts in properties, and strong anisotropy in seismic velocities. With the proposed workflow and attribute based on the inversion results, further estimations of seismic anisotropy, geomechanical properties, and TOC can also be possible. On the basis of the study, the inversion can consequently contribute to the well placement, stimulated reservoir volume (SRV), and the completion design for both conventional and unconventional reservoirs.

DEDICATION

To my Lord, Jesus Christ, and his lovely daughter, my wife

ACKNOWLEDGMENTS

My Ph.D. research is a quite long journey. Sometimes it was calm, but many times, it swung and fluctuated like the seismic traces I encounter every day. Therefore, it has not been trivial for me to reach this point. As a researcher, I have been sailing across an unknown research problem and always trying to cast my anchor on the right place to answer it. However, I failed countlessly and didn't even know what I really wanted to solve at the very beginning of my voyage. Although my research problem became more clear as time went by, I still faced many obstacles that made me lethargic. Nonetheless, I am now finally standing to close this important chapter in my life and to open a new chapter to explore another world. The only way I got through the many obstacles that I encountered during my Ph.D. research was to luckily receive so many advice and help from others. Therefore, I would like to take this opportunity to express my deep appreciation to those that supported me along this journey.

First and foremost, I would like to extend my sincere gratitude to my advisor Dr. Richard Gibson who has guided and supported me through my five-years of Ph.D. research. Dr. Gibson literally taught everything to me: from fundamental theory in seismology and basic knowledge in geophysics to writing styles, how to code, how to deliver ideas to an audience, and most importantly how to think as a scientist. Aside from his academic and professional support, I also learned many invaluable wisdoms of life from him. Dr. Gibson's integrity, care, and love for family and students always set a great example and had a positive impact on me, as I am a father of two children also. From his everyday life, Dr. Gibson showed me how important it is to learn every day throughout our entire life. He is a truly respectful professor.

I also want to thank my co-advisor Dr. Nurul Kabir. Without his advice, this dissertation would not have been possible. In particular, the main method presented in this dissertation research, the nonlinear Zoeppritz inversion, could have not been established without him. I also received many intuitive research ideas from him about how the method can be applied for reservoir characterization. Whenever I needed advice, he was always willing to meet with me.

I am grateful to my committee members Drs. Yuefeng Sun, Hiroko Kitajima, and Michael King for their excellent teaching, support, and inspiration. Specifically, Dr. Yuefeng Sun helped me to understand the nonlinear relationship between parameters in the Zoeppritz equations, which had to be clearly understood in order for me to raise an important question in the dissertation. In addition, I have learned fundamental knowledge about geomechanics from Dr. Hiroko Kitajima's 'Experimental Rock Deformation' class. This knowledge was crucial for me when I applied the proposed inversion into unconventional reservoir characterization. Dr. Michael King also provided great feedback on my preliminary results which allowed me to correct weak points in my research and to strengthen the underlying logic in my methodologies.

In addition, I have to express my deep appreciation to the professors in the Chevron Basin Modeling Center of Research Excellence program (CBM CoRE). These include Drs. Mauro Becker, Andrea Micieli Romero, and Alan Yu. I also appreciate the director of Berg-Hughes Center, Dr. Mukul Bhatia, and Drs. Barry Katz and Tess Menotti from the Hydrocarbon Charge Modeling and Geochemistry Team at Chevron ETC for their sincere support. I have been selected as a recipient of the Chevron fellowship by Berg-Hughes Center as of the fall semester in 2015 until now. During this time I have received financial support including the fellowships, travel grants for many conference presentations, and training grants to accumulate necessary technologies for the dissertation. This financial support allowed me to completely focus on my dissertation research without concerning financial hardships. Above all, I must appreciate Dr. Mauro Becker, the program director of the CBM CoRE, and the sincere advice that he has given me every day, even today. He is one of the most respectful, professional, and kind person that I have ever met. He comes early to the center and always helps all members with his genuine heart. Therefore, I truly believe that everyone who can receive his advice will eventually achieve their desired goals. I hope to become a professional like him one day and contribute towards other's successes also.

I would like to thank the students in my two research groups (i.e., Dr. Richard Gibson's Seismic Research Team, and CBM CoRE) for their helpful discussion, conversation, and companion with me: Kai Gao, Dehan Zhu, Jungrak Son, Mikhail Artemyev, Haider Abdulaal, Qifan Liu,

Kathy Zhang, Edith Sotelo Gamboa, Yongchae Cho, Milan Brankovic, Abdullah Mahrous, April Rider, Eduardo Alvarez, Andros Alexiou, Bassam Alzayer, Sihyung Kim, Ji Hyun Yang, and Dr. Byoung Yeop Kim (in Seismic Research Team), Carlos Varady Mago, Ibrahim Al Atwah, Caitlyn Kelly, Maria Gutierrez Azuaje, Ryan Wilcoxson, Sherif Abdelmoneim, Paul Barth, Fahd Almalki, Stephen Aldridge, Anindito Satrio Baskoro, and Rachel Hoar (in CBM CoRE).

From now, I am heartily expressing my appreciation to my family, and my Lord, Jesus Christ. Firstly, I am thankful for mine and my wife's parents. Without their support and sacrifice, I couldn't have dreamed of studying Geophysics here at Texas A&M University. If this dissertation could give something back to them, my Ph.D. period will be more than meaningful. Special thanks also go to my two lovely children, my brave son Juhwan, and my tiny princess Yoonha. Their innocent smiles and lovely faces enrich my daily life. Without their love, I could not be recharged from every day's long and tired research. Most importantly, I appreciate my wife, Minsung, for her endless support and love to me and our family. Whenever I got lost in my direction, she was always willing to be my North, my South, my East and West. When I began to teeter as I walked, falling almost daily, I, therefore, said to her "Pick me up!" as a person who keeps falling, my wife kept raising me up! Above all, with her every day's prayer for me and our family, she guided me to my Lord, Jesus Christ. Therefore, I believe she deserves my love and respect. Last, but not least, I have to appreciate God, who is my Lord, to lead my life on his road, who opened my heart to pay attention to what he has been saying to me and gave me endless life.

Finally, Drs. Gibson, Kabir and I thank CGG for the release of the Gulf of Mexico data presented in the dissertation. Furthermore, we acknowledge Chevron for an admission to use their dataset including ultrasonic measurements, logs, and geochemical analyses for a well located in the Permian basin. The views expressed in this dissertation are the views of the author and do not necessarily reflect the views of CGG and Chevron. We also acknowledge that CGG's Hampson-Russell AVO software was used for comparison purposes in this research.

CONTRIBUTORS AND FUNDING SOURCES

Contributors

This work was supported by a dissertation committee consisting of Professors Richard L. Gibson, Jr., Nurul Kabir, Yuefeng Sun, and Hiroko Kitajima of the Department of Geology & Geophysics, and Professor Michael King of the Department of Petroleum Engineering.

The seismic data and well dataset including ultrasonic measurements, logs, and geochemical analyses used for demonstrating the effectiveness of proposed methods in Chapters 2 and 4 were provided by CGG (for the seismic data) and Chevron (for the well dataset), respectively. All the work conducted for the dissertation was completed by the student independently.

In order to generate correct anisotropic AVO response from models presented in the dissertation, Professor Gibson's `ANPRX 3.5` is applied with his permission. All the other results of seismic inversion are created by using the self-developed program. For the derivation of the gradients of exact PP- and converted PS-reflections in Zoeppritz equations, the symbolic calculation functions in `Mathematica` are applied. `Mathematica` is also used for the development of the nonlinear Zoeppritz AVO inversion and plotting the graphs and figures in the dissertation. Lastly, the dissertation is written by using LaTeX.

Funding Sources

Graduate study was supported by the Chevron fellowship from the Chevron Basin Modeling Center of Research Excellence (CBM CoRE) program in Berg-Hughes Center for Petroleum and Sedimentary Systems, Texas A&M University. The study was also partially supported by the Lechner Graduate Scholarship from the Office of Graduate and Professional Studies (OGAPS) Lechner Graduate Grant Program, and the Texas A&M Energy Institute Fellowship from the Texas A&M Energy Institute.

NOMENCLATURE

AVO	Amplitude Variation with Offset
CMP	Common-midpoint
GOM	Gulf of Mexico
GR	Gamma-ray
FWI	Full-waveform Inversion
HI	Hydrogen Index
HRS	HampsonRussell Software
NMO	Nomal-moveout
RMS	Root-mean-square
SEM	Scanning Electron Microscope
SNR	Signal-to-noise Ratio
SRV	Stimulated Reservoir Volume
TOC	Total Organic Carbon content
VTI	Vertical Transverse Isotropy
AI ($= Z_P$)	Acoustic Impedance
SI ($= Z_S$)	Shear Impedance
$R_{PP}(\theta)$	P-wave reflection amplitude for incident angle θ
$R_{PS}(\theta)$	Converted PS-wave (i.e., reflected SV-wave) reflection amplitude for incident angle θ
$T_{PP}(\theta)$	Transmitted P-wave reflection amplitude for incident angle θ
$T_{PS}(\theta)$	Transmitted PS-wave (i.e., transmitted SV-wave) reflection amplitude for incident angle θ
$_1$ (Subscript 1)	Upper medium

$_2$ (Subscript 2)	Lower medium
$\theta\ (=\theta_1)$	Incident or reflected angles for P-wave
θ_2	Reflected angles for converted PS-wave
$\bar{\theta}$	Average of incident and transmitted angles for P-wave (i.e., $(\theta_1+\theta_2)/2$)
ϕ_1	Refracted or transmitted angles for P-wave
ϕ_2	Transmitted angles for converted PS-wave
c_{ij}	Elastic stiffness coefficient in Voigt notation, $i,j = 1,2,\ldots,6$
$\alpha\ (=V_P)$	P-wave velocity of medium
$\beta\ (=V_S)$	S-wave velocity of medium
ρ	Mass density of medium
ε, γ, δ	Thomsen parameters
λ, μ	$Lam\acute{e}$ parameters
k	Bulk modulus
E	Young's modulus
ν	Poisson's ratio
$\Delta\alpha$	Difference in P-wave velocities (i.e., $\alpha_2-\alpha_1$)
$\Delta\beta$	Difference in S-wave velocities (i.e., $\beta_2-\beta_1$)
$\Delta\rho$	Difference in P-wave velocities (i.e., $\rho_2-\rho_1$)
$\Delta\nu$	Difference in Poisson's ratios (i.e., $\nu_2-\nu_1$)
$\bar{\alpha}$	Average P-wave velocities (i.e., $(\alpha_1+\alpha_2)/2$)
$\bar{\beta}$	Average S-wave velocities (i.e., $(\beta_1+\beta_2)/2$)
$\bar{\rho}$	Average P-wave velocities (i.e., $(\rho_1+\rho_2)/2$)
$\bar{\nu}$	Average Poisson's ratios (i.e., $(\nu_1+\nu_2)/2$)
x	Model vector

y	State vector
z	Data vector
v	Output vector
ω	Multiplier vector (or weighting factor)
φ	A mapping from a domain vector to a range vector
M	Observation operator
R	Object function
$\mathbb{R}$	The set of real numbers
$\|\quad\|$	L_2- norm
$\mathcal{L}$	The Lagrangian of an objective function
δ	The total derivative of a function
∂	The partial derivative of a function
∇	The gradient of a function (i.e., the vector of partial derivatives)

TABLE OF CONTENTS

Page

LIST OF FIGURES

FIGURE Page

LIST OF TABLES

TABLE Page

1. INTRODUCTION

1.1 Motivation

Seismic inversion is a fundamental task in geophysical studies to characterize elastic properties of subsurface layers such as seismic wave velocity, density as well as impedance. Among many seismic inversion methods, Amplitude Variation with Offset (AVO) inversion is an effective method to estimate the properties of target layers in reservoir conditions (Castagna and Backus, 1993). If AVO inversion can successfully estimate the parameters of target formations, additional physical constraints to understand the target reservoirs (e.g., porosity, types of saturated fluid, geomechanical properties, organic abundance, etc.) can also be inferred (Castagna and Backus, 1993; Connolly, 1999; Hilterman, 2001; Chopra et al., 2013).

When a seismic wave strikes a boundary between two layers at a non-zero angle of incidence, P-wave to S-wave conversion occurs and the reflection coefficient becomes a function of the properties of the layers (i.e., P-wave and S-wave velocities, and density). This conversion generates energy partitioning at a reflection point on the boundary, and indeed, following four different waves are consequently generated: reflected P-wave and S-wave, and transmitted P-wave and S-wave. The equations from which the variations of the amplitude of each wave can be derived with plane wave assumption are named after the Zoeppritz equations (Zoeppritz, 1919). Most of AVO analyses are developed based on the Zoeppritz equations since it can provide analytical solutions of amplitudes for P-wave and converted PS-wave reflections that are normally achieved and utilized from a typical seismic survey.

Nonetheless, the direct application of the Zoeppritz equations for inversion of the elastic properties from observed AVO data is not a trivial problem due to the fact that the target elastic parameters are non-linearly coupled in the equations. Therefore, most conventional AVO inversions are implemented with linearized approximations of Zoeppritz equations such as Aki and Richards (1980), Wiggins et al. (1983), Shuey (1985), and Fatti et al. (1994). However, linearization means

loss of completeness, although they are elaborately developed and some of them have been applying as standard tools for AVO inversion. For example, Fatti et al. (1994)'s three-terms equation is a linearized approximation of PP reflection that has been widely being used to decouple P-wave velocity and density from acoustic impedance. In addition, Hampson et al. (2005) developed a simultaneous inversion by introducing the regional rock property relationship estimated from well-logs into Fatti's equation. This made up for the weak points of Fatti's equation: unstableness of inverted solutions. Therefore, the simultaneous inversion is well known as the mostly applied standard AVO inversion tool for the oil and gas industry nowadays. However, it is known that these approximation methods may still provide spurious results since the linearization can only successfully be achieved by assuming weak contrasts in the parameters and seismic isotropy. As a result, conventional AVO inversions cannot correctly estimate elastic parameters of some geologically important formations which are highly anisotropic and often surrounded by hard layers to generate strong contrasts. For example, organic-rich shale formations in unconventional reservoirs are often anisotropic, with a correlation between anisotropy and Total Organic Carbon (TOC) content (Vernik and Nur, 1992; Carcione, 2001; Carcione et al., 2011; Sondhi, 2011; Sone, 2012; Sayers et al., 2015). Especially, Vernik and Nur (1992) showed organic materials in shale is one of the major source of the anisotropy. Sone (2012) found that organic materials in shale exhibited a low aspect ratio (the ratio between smallest and largest dimensions). Since solid organic materials are usually more compliant, they are distributed more heterogeneous and their shape corresponds to lower aspect ratio than other minerals in shale, as depicted in Figure 1.1 Consequently it has a significant effect on the seismic reflection amplitudes as shown in Carcione (2001) and Sayers et al. (2015). Therefore, neglecting the shale anisotropy may cause incorrect estimation of rock properties. Although Rüger (1997) proposed an AVO equation for P-wave reflection coefficients in anisotropic media, it only provides an accurate solution based on the assumption of weak contrast and weak anisotropy; the level of weak anisotropy is generally defined as $10 \sim 20\%$ difference in seismic velocities by Thomsen (1986). However, the anisotropy level of organic-rich shale can easily exceed the weak anisotropy definition and reaches up to 40% (Vernik, 2016). In addition,

if target layers are surrounded by carbonates or salt-domes, it relates to strong contrasts even in conventional reservoirs. For this reason, AVO inversion based on linearized equations does not produce correct results when target reservoirs have strong contrasts and strong anisotropy (Lavaud et al., 1999; Lim et al., 2017). Figure 1.2 illustrates examples of the failure of linearized methods to estimate the correct variation of amplitude on target boundaries. The first example (Figure 1.2(a)) corresponds to the case of strong contrast generated from a boundary between two isotropic media: Austin Chalk and Upper Eagle Ford (the case of 0 kerogen volume fraction). Model values are described in Table 2.1. As depicted, there is a significant discrepancy between estimations (from Fatti's three terms approximation) and correct solutions (from the Zoeppritz equation) in the far angle range over 30°. This discrepancy will eventually lead to incorrect estimation of V_P and ρ. Even worse in anisotropy case (Figure 1.2(b)) that an organic-rich shale is underlain by a limestone layer, deviations of estimation from correct solution start right after normal incidence angle, which is 0°. Table 3.1 listed corresponding model values (Kerogen volume fraction: 0.2). Estimations and solutions are computed by the Rüger (1997)'s linearized approximation for weak anisotropy and a paraxial ray tracing (Gibson et al., 1991). In this case, only acoustic impedance can be estimated correctly. On the other hand, estimations of all other parameters will be wrong. This is an important motivation for developing a reliable way to utilize the full Zoeppritz equation on AVO inversion so that the AVO inversion can accurately obtain V_P, V_S, and ρ without any further assumptions.

Another particularly difficult challenge is density estimation (Dębski and Tarantola, 1995) from AVO inversion. Even if the non-linear inversion using the exact Zoeppritz equation is possible, a very wide AVO angle range that close to critical angle is still required in order to invert density correctly (Lavaud et al., 1999). This is due to the fact that the contrast of density contributes to the AVO curve mostly at the near angle range. On the other hand, the contrast of P-wave velocity contributes to the AVO curve along with all the range of incident angles. Therefore, when far angle range data is available, decoupling density and P-wave velocity from inverted acoustic impedance could only be possible with a conventional PP reflection survey. The only exception is a situation

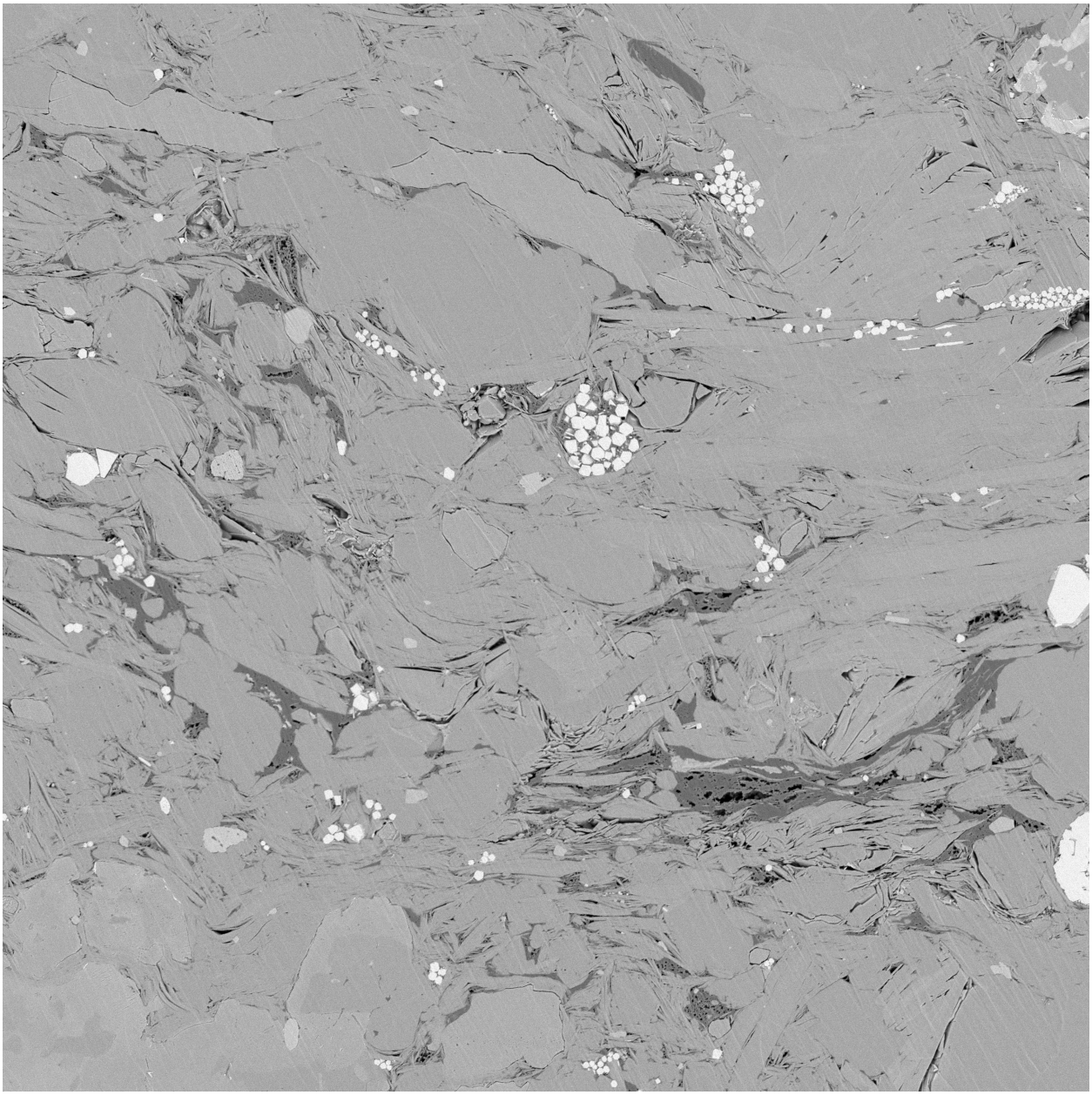

Figure 1.1: A Scanning Electron Microscope (SEM) image of shale. Heterogeneity of the distribution of organic content (dark grey) in shale is clearly observed. It also shows the aspect ratio of organic content is much lower than other minerals.

that density contrast across an interface is larger than P-wave velocity contrast such that gas is highly saturated in a high porous sand (Kabir et al., 2005; Behura et al., 2010). However, the long offset acquisition is first costly, and pre-processing to get stable reflection amplitudes in far angle

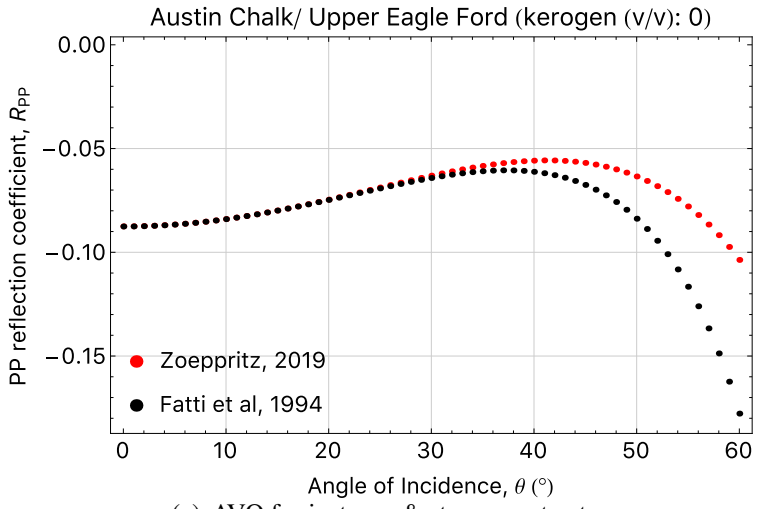

(a) AVO for isotropy & strong contrast

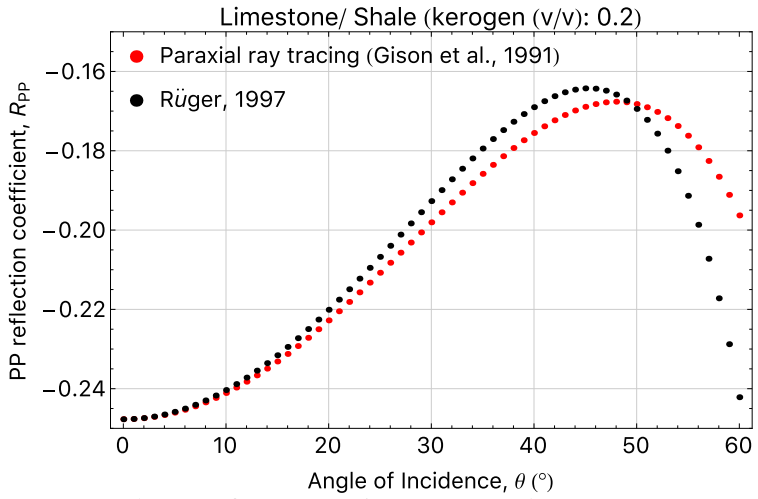

(b) AVO for strong anisotropy & weak contrast

Figure 1.2: Comparisons of AVO responses (reflection coefficients). The analytical solution of AVO generated by Zoeppritz (1919)'s equation is compared to an estimation from Fatti et al. (1994) (a). In addition, two different anisotropic AVO responses are computed by Gibson et al. (1991)'s paraxial ray tracing and Rüger (1997)'s linearized approximation (b).

ranges is secondly a big challenge due to more noisy conditions and NMO-stretch (Hilterman, 2001; Yoo and Gibson Jr, 2005; Lim, 2014). In addition, most of the linearized AVO approach requires to know the background the ratio of averaged P-wave and S-wave velocities between two target layers, $\frac{\bar{V}_P}{\bar{V}_S}$, which is related to another physical parameter called Poisson's ratio. Even though variability of the background parameter is less than other target parameters such as den-

sity, P-wave and S-wave velocities in nature at reservoir condition, a major change in the P-wave amplitude coefficient as a function of offset can be caused by a significant change in Poisson's ratio, as Ostrander (1984) showed. Therefore, if the background parameter is not correctly assumed in advance, any linearized inversions will eventually provide inaccurate estimations. Combining amplitudes of PP- and converted PS-reflections jointly for AVO inversion with a multicomponent survey may contribute to overcoming the aforementioned challenges. As shown in numerous previous studies with the joint inversion scheme (Margrave et al., 2001; Kurt, 2007; Lim et al., 2018), the addition of PS-AVO information has the potential to stabilize and improve the results of inversion even with limited AVO angle range and without the prerequisite information, background $\frac{\bar{V}_P}{\bar{V}_S}$. This is another important motivation to develop the nonlinear Zoeppritz AVO inversion not only with PP-reflection but also with converted PS-reflection together.

As briefly mentioned at the beginning of this section, elastic properties, that can be estimated from AVO inversion, can also be linked to further estimation of additional physical constraints of target subsurface layer such as porosity, types of saturated fluid and lithology (Shuey, 1985; Gardner and Forel, 1987; Smith and Gidlow, 1987; Rutherford and Williams, 1989; Verm and Hilterman, 1995; Goodway et al., 1997). However, most of rock property estimations only targeted typical high porous rocks: mainly sandstone and often carbonates, before unconventional shale has emerged as a viable energy resource. Nonetheless, accurate characterization of source rock properties became increasingly important in the last decade, since shale is now not only treated as source rock but also as a reservoir in the unconventional petroleum system. Consequently, the estimation of properties of shales from seismic data is important for the development of unconventional reservoirs. In particular, seismic anisotropy and geomechanical properties (i.e., Young's modulus and Poisson's ratio) are key parameters that have a direct influence on the effective hydraulic fracturing, defining landing zones of horizontal wells. If AVO inversion can successfully estimate parameters such as P-wave and S-wave velocities and density for target shale formations, their geomechanical properties such as Young's modulus and Poisson's ratio can also be determined (Chopra et al., 2013). Zong et al. (2013) and Payne and Meyer (2017) showed examples of

how AVO inversion can infer a representative value of geomechanical properties with the assumption of seismic isotropy. Organic-rich shale formations are, however, often anisotropic (Vernik and Nur, 1992; Johnston and Christensen, 1995; Sondergeld et al., 2000); this means that not only seismic wave velocities but also geomechanical properties have the anisotropic characteristic. Sayers et al. (2015) also showed that the level of anisotropy increases when the volume fraction of total organic carbon content (TOC) in shale increases. However, although the effect of the TOC on the seismic anisotropy of unconventional reservoir was demonstrated over two decades, little attention has been paid to the estimation of seismic anisotropy using AVO inversion. If the determination of seismic anisotropy is possible, it may be achievable to further estimation of geomechanical properties as well as their anisotropy.

Estimation of total organic carbon (TOC) content of shale is also important since hydrocarbon sweet spots can generally be characterized by high TOC in unconventional plays. Solid organic matter in shale is generally referred to as kerogen and its fractional content is measured from core samples with a Rock-Eval pyrolysis device and typically reported as TOC (Jarvie et al., 2007; Huc, 2013). Although there are many different versions of the Rock-Eval pyrolysis differently developed by Durand and Espitalie (1976), Espitalié et al. (1977), Price (1983), and Durand et al. (1987), the device generally includes combustion and pyrolysis ovens together with hydrocarbon and CO_2 detectors. The output from the Rock-Eval can be used for extracting such data from core samples: TOC, the petroleum potential of the rock, the type of kerogen, and its thermal maturity. However, this direct measurement is only possible with expensive coring and laboratory treatments and thus quite costly. Whereas, petrophysical correlation methods based on wireline logs such as Schmoker (1979) and Passey et al. (1990) have been widely used for indirect TOC measurement. Once the indirect estimation is calibrated by direct TOC measurements in reference wells, geostatistical interpolation methods can further be applied to estimate its lateral variation. In addition, changes in TOC in shale can be detected from the surface seismic response, since the organic portion of shale influences its elastic properties such as P-wave and S-wave velocities, and density (Chopra et al., 2013). When a sound relationship between TOC and elastic properties of shale is

built, TOC can be inferred from estimated elastic properties by seismic inversion. Løseth et al. (2011) and Altowairqi et al. (2017) estimate TOC from inverted acoustic impedance, which is the product of P-wave velocity and density. However, if density and P-wave velocity are decoupled from acoustic impedance, it may be possible to more reliably infer TOC from density, since density is more directly governed by the organic portion of shale than any other elastic properties that can be estimated from seismic inversion (Schmoker, 1979; Vernik, 2016). In addition, determination of the level of anisotropy can also be linked to TOC estimation as discussed before. Again, AVO inversion may make important contributions to such tasks if the estimation of density and seismic anisotropy is possible. This is the last motivation for proposing workflows based on results from the nonlinear Zoeppritz AVO inversion in order to infer seismic anisotropy, geomechanical properties, and TOC of target layers so that the AVO inversion can eventually contribute toward both conventional and unconventional reservoir characterization.

1.2 Literature review

The Zoeppritz equation is a set of equations that describe the partitioning of seismic wave energy at an interface, typically a boundary between two different layers of rock. Zoeppritz (1919) solved the amplitudes of reflected and transmitted waves using the continuation of stress and displacement across in both the normal and tangential directions across an interface between two layers, which gives the equations with respect to the angle of incidence, densities, and elastic moduli. It can be expressed as the following matrix:

$$\begin{bmatrix} R_{PP}(\theta_1) \\ R_{PS}(\theta_1) \\ T_{PP}(\theta_1) \\ T_{PS}(\theta_1) \end{bmatrix} = \begin{bmatrix} -\sin\theta_1 & -\cos\phi_1 & \sin\theta_2 & \cos\phi_2 \\ \cos\theta_1 & -\sin\phi_1 & \cos\theta_2 & -\sin\phi_2 \\ \sin 2\theta_1 & \frac{V_{P1}}{V_{S1}}\cos 2\phi_1 & \frac{\rho_2 V_{S2}^2 V_{P1}}{\rho_1 V_{S1}^2 V_{P2}}\cos 2\phi_1 & \frac{\rho_2 V_{S2} V_{P1}}{\rho_1 V_{S1}^2}\cos 2\phi_2 \\ -\cos 2\phi_1 & \frac{V_{S1}}{V_{P1}}\sin 2\phi_1 & \frac{\rho_2 V_{P2}}{\rho_1 V_{P1}}\cos 2\phi_2 & -\frac{\rho_2 V_{S2}}{\rho_1 V_{P1}}\sin 2\phi_2 \end{bmatrix}^{-1} \begin{bmatrix} \sin\theta_1 \\ \cos\theta_1 \\ \sin 2\theta_1 \\ \cos 2\phi_1 \end{bmatrix}, \quad (1.1)$$

where R_{PP}, R_{PS}, T_{PP} and T_{PS} are the reflected P-, reflected S-, transmitted P-, and transmitted S-wave amplitude coefficients. V_P, V_S, and ρ denote P-wave velocity, S-wave velocity, and density,

and subscripts 1 and 2 represent the upper and lower layers, respectively. Furthermore, when θ_1 represents the incident angle of P-wave, θ_2, ϕ_1, and ϕ_2 correspond to the angle of transmitted P-wave and the angle of reflected and transmitted S-wave. All angles are measured from the normal to the interface as the parameters are illustrated in Figure 1.3. Inverting the matrix form provides the exact amplitudes as a function of the angles described above. Figure 1.3 also illustrates the mode conversion for a P-wave incident on a planar boundary.

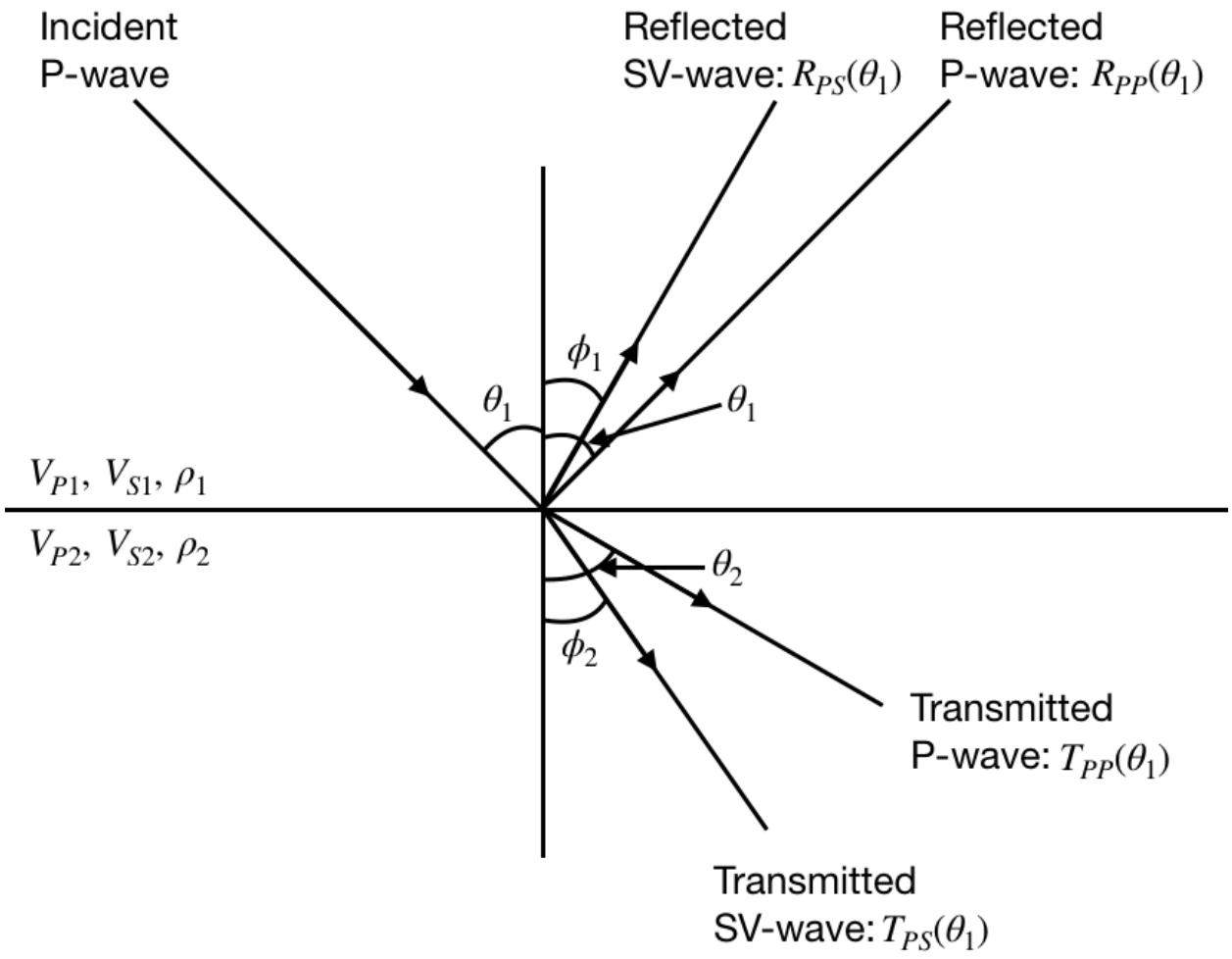

Figure 1.3: Mode conversion of an incident P-wave on the boundary between two elastic layers.

As illustrated in equations 1.1, target elastic parameters are non-linearly coupled in the equa-

tions. Therefore, to invert the parameters with direct application of the Zoeppritz equations stably is not a trivial problem. In order to avoid the mathematical unstableness of the inversion, many researchers developed linear approximations of the Zoeppritz equation, especially for P-wave reflection. These linear approximations apparently provide such advantages: the decoupling of variables and insights to predict how AVO as a function of rock properties. Although there are numerous linearized approximations, each equation emphasizes different aspects of the rock properties. Following equations are good examples of the point:

$$R_{PP}(\theta) = \frac{1}{2}\ln\left(\frac{\alpha_2\rho_2\cos\theta_1}{\alpha_1\rho_1\cos\theta_2}\right) + \left(\frac{\cos\theta_1}{\alpha_1}\right)^2(\beta_1^2-\beta_2^2)\left(2+\frac{\ln(\rho_2/\rho_1)}{\ln(\beta_2/\beta_1)}\right) \qquad \text{(Bortfeld, 1961)} \tag{1.2}$$

$$R_{PP}(\theta) = \frac{1}{2}\left(1-\frac{4\bar{\beta}^2}{\bar{\alpha}^2}\sin^2\bar{\theta}\right)\frac{\Delta\rho}{\bar{\rho}} + \frac{1}{2\cos^2\bar{\theta}}\frac{\Delta\alpha}{\bar{\alpha}} - \frac{4\bar{\beta}^2}{\bar{\alpha}^2}\frac{\Delta\beta}{\bar{\beta}}\sin^2\bar{\theta} \qquad \text{(Aki and Richards, 1980)} \tag{1.3}$$

$$R_{PP}(\theta) = NI_P + \left(A_0 NI_P + \frac{\Delta\nu}{(1-\bar{\nu})^2}\right)\sin^2\bar{\theta} + \frac{1}{2}\frac{\Delta\alpha}{\bar{\alpha}}(\tan^2\bar{\theta}-\sin^2\bar{\theta}), \qquad \text{(Shuey, 1985)}$$

$$\text{where } NI_P = \frac{1}{2}\left(\frac{\Delta\alpha}{\bar{\alpha}}+\frac{\Delta\rho}{\bar{\rho}}\right) \tag{1.4}$$

$$A_0 = B - 2(1+B)\left(\frac{(1-2\nu)}{(1-\nu)}\right)$$

$$B = \frac{\frac{\Delta\alpha}{\bar{\alpha}}}{\frac{\Delta\alpha}{\bar{\alpha}}+\frac{\Delta\rho}{\bar{\rho}}}$$

Here α, β, ρ, and ν indicate P-wave velocity, S-wave velocity, density, and Poisson's ratio and subscripts 1 and 2 represent the upper and lower layers, respectively. $\bar{\alpha}$, $\bar{\beta}$, $\bar{\rho}$, and $\bar{\nu}$ are averages of parameters of underlying and overlying layers. In addition, the Δ symbol denotes subtraction between the parameters of two layers. Bortfeld (1961)'s equation 1.2 emphasizes on the fluid and rigidity terms to provide an insight for interpretation of fluid-substitution problems. Specifically, the first and second terms correspond to the effects of saturated fluid and rock rigidity, respectively. Sequentially, Aki and Richards (1980)'s equation 1.3 emphasis on how P- and S-wave

velocities and density contribute to the variation of amplitude. On the other hand, Shuey (1985) provided an insight of angle dependence by modifying Aki and Richards (1980)'s equation. The first term relates to near angle range, and second and third terms are dependent on middle and far angle ranges, respectively. Shuey (1985) showed how the estimates of Poisson's ratio could easily be extracted from limited AVO ranges, zero offset to mid-angle, by fitting only the first two terms of equation 1.4 to observed AVO data in a CDP gather. This formulation was further utilized for a cross-plot application in terms of Poisson's ratio (ν) versus the natural logarithm of acoustic impedance ($\ln(\rho\alpha)$). Therefore, Shuey (1985)'s approach was the first practical method that suggested for extracting lithology information from seismic data with the extracted acoustic impedance and Poisson's ratio from seismic and the cross-plot from well-log data. In succession to Shuey (1985), authors as Gardner and Forel (1987), Smith and Gidlow (1987), Rutherford and Williams (1989), Verm and Hilterman (1995), Ross (1995), Castagna and Swan (1997), Goodway et al. (1997), and Castagna et al. (1998) continuously developed AVO analyses that link inverted elastic properties to rock properties. Above all, Smith and Gidlow (1987) and Goodway et al. (1997) developed AVO attributes named after the fluid factor and the fluid discriminant ($\lambda\rho$), respectively. The attributes theoretically provide discrimination of pore-fluid content from AVO with an assumption of $\frac{\bar{V_P}}{\bar{V_S}} = 2$. Rutherford and Williams (1989) proposed a new classification of the AVO curves (AVO Classes 1, 2, and 3) to assist in the recognition of hydrocarbon-saturated formations and relate the classes to AVO anomalies. The classification only depends on the contrast in acoustic impedance between the target sand reservoir and its surrounding shales. Later, the classification scheme for AVO anomalies was completed with further modifications by Ross (1995) and Castagna and Swan (1997) as following:

- Class 1 for high impedance sand with decreasing AVO
- Class 2 for near-zero impedance contrast
- Class 2p for similar to 2, but with polarity change
- Class 3 for low impedance sand with increasing AVO

- Class 4 for low impedance sand with decreasing AVO

Impedances and trends of AVO (i.e., decrease or increase of AVO) in the classification generally correspond to intercepts and gradients (or slopes) of typical AVO curves. After the classification, an AVO cross-plotting, that plots AVO intercept (A) against gradient (B), was developed by Castagna and Swan (1997) and Castagna et al. (1998). In addition, Verm and Hilterman (1995) and Goodway et al. (1997) proposed a different type of crossplots using parameters (normal-incident reflection coefficient, Poisson's ratio, $\lambda\rho$, and $\mu\rho$), that inverted from linear AVO inversions, for further estimation of rock-properties and lithology discrimination. Verm and Hilterman (1995)'s cross-plotting, named the color-crossplot, assign specified colors to bins of a crossplot in which the point of normal-incident reflection coefficient and Poisson's ratio fails. Then, targets of interest are defined by transferring the colors to output trace at corresponding time samples in seismic data. Goodway et al. (1997)'s the $\lambda\rho$ and $\mu\rho$ crossplot has been being used as an industry standard crossplot to discriminate target pore-fluid content, lithology, even higher TOC from the background. This approach is based on physical properties of λ and ρ due to the fact that λ, the incompressibility, is sensitive to pore fluid but ρ, the rigidity, is whereas sensitive to the rock matrix. Since it is not possible to decouple the effects of density from λ and μ with the AVO equations described above, cross-plotting $\lambda\rho$ and $\mu\rho$ is chosen a method to minimize the density effect. $\lambda\rho$ and $\mu\rho$ can be computed from values of acoustic and shear impedances inverted from the linear AVO inversions as following:

$$\begin{aligned} \mu\rho &= Z_S^2 = (\rho V_S)^2 \\ \lambda\rho &= Z_P^2 - 2Z_S^2 = (\rho V_P)^2 - 2(\rho V_S)^2, \end{aligned} \tag{1.5}$$

where Z_P and Z_S are acoustic and shear impedances, respectively.

Even though above linear methods successfully applied for the estimation of certain rock properties, reservoir characterization by AVO inversion has still limited mainly due to the following

assumptions as mentioned by Hilterman (2001):

- Small angle variation: Linear approximations of the Zoeppritz equation are only adequate to about 30° incident angle.
- Weak contrast: Incident and transmitted angles are approximately equal.
- Third-order terms in equations 1.2, 1.3, and 1.4 are insignificant out to about 30° incident angle.

For example, the extraction of density from AVO inversion was thought to be unstable and challenging (Dębski and Tarantola, 1995). Nonetheless, some efforts pushing toward stable density inversion has continuously been being made by Fatti et al. (1994), Hampson et al. (2005), Lavaud et al. (1999), Kabir et al. (2005), and Behura et al. (2010), since density may include crucial information about the presence and saturation of hydrocarbon. Especially, Fatti et al. (1994)'s three-terms equation is a linearized approximation of PP reflection that has been widely being used to decouple P-wave velocity and density from acoustic impedance. Following is its formulation:

$$
\begin{aligned}
R_{PP}(\theta) &= c_1 R_P(0^\circ) + c_2 R_S(0^\circ) + c_3 R_D, \qquad (1.6)\\
\text{where} \quad c_1 &= 1 + \tan^2\theta \\
c_2 &= -8K\sin^2\theta \\
c_3 &= 2K\sin^2\theta - \frac{1}{2}\tan^2\theta \\
K &= \left[\frac{\bar{V_P}}{\bar{V_S}}\right]^2 \\
R_P(0^\circ) &= \frac{1}{2}\{\frac{\Delta V_P}{\bar{V_P}} + \frac{\Delta\rho}{\bar{\rho}}\} \\
R_S(0^\circ) &= \frac{1}{2}\{\frac{\Delta V_S}{\bar{V_S}} + \frac{\Delta\rho}{\bar{\rho}}\} \\
R_D &= \frac{\Delta\rho}{\bar{\rho}}.
\end{aligned}
$$

The decoupling can be achieved by inverting two impedance contrasts (R_P and R_S) and one den-

sity contrast (R_D) when wide AVO angle ranges are available. Since the coefficients in the equation are not equal in size, the solutions for contrasts of shear impedance (R_S) and density (R_D) can be unstable at small angles. Therefore, Hampson et al. (2005) presented a simultaneous inversion in order to enhance the stableness of inversion. Firstly, they assumed a linear relationship between the logarithm of P-impedance and both S-impedance and density that can be analyzed from well-logs that deployed in the target reservoir. Then, they applied the known regional rock property relationship between target variables into Fatti et al. (1994)'s three-terms equation. The simultaneous inversion is now one of the most used industry standard tools for AVO inversion due to its stableness. However, the above linearized approximation can only successfully provide accurate solution of P-wave reflection by assuming weak contrasts in the parameters, small angle of incidence, and seismic isotropy. Although succeeded high-order approximations as in Ursin and Dahl (1992), Wang (1999), and Ursenbach (2002) improved the accuracy to larger angles, any approximations listed above fail to generate correct amplitude at angles near the critical angle, compared to the Zoeppritz equation. Lavaud et al. (1999) showed that crucial information resides near the critical angle, especially for correct density extraction. Therefore, the utilization of the Zoeppritz equation is necessary in order to precisely invert target parameters.

Aiming this objective, Lavaud et al. (1999) developed a nonlinear inversion by applying a reformulation of the Zoeppritz equation and an adjoint state technique. They first rewrote the Zoeppritz equation in terms of a background and three contrast parameters in P-wave and S-wave velocities and density. Then, the adjoint state technique by Burger and Chavent (1979) was applied to efficiently compute the gradient of an object function composed of the non-linearly coupled parameters. This approach makes the nonlinear inversion possible and stable. Therefore, target parameters can more accurately be determined by the nonlinear inversion than other linear inversions. Later, Lim et al. (2017) applied the nonlinear Zoeppritz inversion into the characterization of unconventional shale, which is a highly anisotropic medium. Details of Lavaud et al. (1999)'s method and some parts of results in Lim et al. (2017) will be discussed in later sections of the dissertation. Zhu and McMechan (2012) also presented another nonlinear inversion based on the Zoeppritz equation

in a different reformulation. Zhi et al. (2013, 2016) followed Zhu and McMechan (2012)'s approach for further applications. However, the general approach of Zhu and McMechan (2012) and Zhi et al. (2013, 2016) are the same on Lavaud et al. (1999)'s original approach.

Although above mentioned nonlinear inversions promise better estimation than other linear inversions, it is still challenging to extract accurate density information. This requires a very long offset survey that should reach to critical angles if conventional P-wave reflection is only considered as input data for AVO inversion. Also, a prerequisite information, the background ratio of averaged P-wave and S-wave velocities, $\frac{\bar{V_P}}{\bar{V_S}}$, has to be concisely known before any inversions. In order to avoid the costly long offset survey, many researchers applied joint inversion approaches using additional information besides PP reflection: converted PS seismic reflection (Margrave et al., 2001; Kurt, 2007; Hampson and Russell, 2013; Zhi et al., 2013; Lim et al., 2018). Although Margrave et al. (2001) applied a linearized approximation to the PP- and PS-AVO, their joint inversion results were superior to invert the fractional contrasts in acoustic and shear impedances when they were compared to the results using PP reflection alone. This is due to the fact that the ambiguities in the PP-AVO are reduced with in addition to PS-AVO information. However, the addition of data generally requires more computation efforts. Kurt (2007) proposed a generalized linear inversion (GLI) as a mathematical tool to jointly use PP- and PS-reflections together. The proposed GLI was combined with a bootstrapping method of statistical analysis that results in limiting repeat of the inversion and reducing the computational time. In addition, Hampson and Russell (2013) expanded their simultaneous inversion presented in Hampson et al. (2005) to the joint inversion approach. Above all, Lim et al. (2018) applied a nonlinear joint AVO inversion based on the exact Zoeppritz equation into an anisotropic model of Eagle Ford shale. The results showed that the joint inversion provides an accurate estimation of horizontal P- and S-wave velocities by decoupling density from impedances. The background parameter, $\frac{\bar{V_P}}{\bar{V_S}}$, also correctly inverted without any prior assumption. A noticeable accomplishment is that the results are achieved with an accessible AVO angle range ($0^\circ \sim 40^\circ$) that can be obtained from a general seismic acquisition. On the other hand, it also showed that both conventional linear inversions and the nonlinear inversion using PP reflection

only fail to estimate S-wave velocity and the background parameter, especially. Details of the method and the analyses in Lim et al. (2018) will be discussed in section 3 of the dissertation.

Although most sedimentary rocks are observed to be anisotropic from many experiments, most seismic applications based on elasticity theory were developed under the assumption of isotropy (Thomsen, 2014). However, it is known that if a seismic wave with a wavelength longer than target layers thickness propagates through a layered sequence of isotropic or VTI media, the wave behaves as if it propagates in a homogeneous but anisotropic medium, as Backus (1962) proved. Therefore, there is a fundamental discrepancy between reality and seismic applications. Thomsen (1986) accounted for the effects of seismic anisotropy in the seismic method. He first defined the level of anisotropy with the following three parameters, that named after the Thomsen parameters:

$$\begin{aligned} \varepsilon &= \frac{c_{11} - c_{33}}{2c_{33}} \\ \gamma &= \frac{c_{66} - c_{44}}{2c_{44}} \\ \delta &= \frac{(c_{13} + c_{44})^2 - (c_{33} - c_{44})^2}{2c_{33}(c_{33} - c_{44})}, \end{aligned} \tag{1.7}$$

where c_{ij} are elastic stiffness coefficient in the conventional *Voigt* two-index notation (Auld, 1973; Nye, 1985) and defined with P and S velocities at 0°, 45°, and 90° as:

$$\begin{aligned} c_{11} &= \rho V_P^2(90^\circ) \\ c_{33} &= \rho V_P^2(0^\circ) \\ c_{44} &= \rho V_S^2(0^\circ) \\ c_{66} &= \rho V_{SH}^2(90^\circ) \\ c_{12} &= c_{11} - 2c_{66} \\ c_{13} &= -c_{44} + \sqrt{4\rho^2 V_P^4(45^\circ) - 2\rho V_P^2(45^\circ)(c_{11} + c_{33} + 2c_{44}) + (c_{11} + c_{44})(c_{33} + c_{44})} \end{aligned} \tag{1.8}$$

In a weak anisotropy situation, that corresponds to defined $10 \sim 20\%$ difference between horizon-

tal and vertical velocities, the set of equations 1.7 can be modified as follows:

$$\begin{aligned}
\varepsilon &\approx \frac{V_P(90^\circ) - V_P(0^\circ)}{V_P(0^\circ)} \\
\gamma &\approx \frac{V_{SH}(90^\circ) - V_{SH}(0^\circ)}{V_{SH}(0^\circ)} \\
\delta &\approx 4\left[\frac{V_P(45^\circ) - V_P(0^\circ)}{V_P(0^\circ)}\right] - \varepsilon
\end{aligned} \tag{1.9}$$

Bork et al. (1997) and Hilterman (2001) provided examples with anisotropic forward modeling in order to show significant differences between the AVO responses with and without anisotropy. Especially, Bork et al. (1997) related VTI anisotropy to the unusual AVO anomalies they observed in the Gulf of Mexico and Trinidad. More importantly, they also emphasized that a new seismic inversion tool that can handle anisotropy should be developed. Rüger (1997) proposed following AVO equation for P-wave reflection coefficients in a TI media:

$$R_{PP}^{TI}(\theta) = A + B\sin^2\theta + C\sin^2\theta\tan^2\theta, \tag{1.10}$$

$$\text{where} \quad A = \frac{1}{2}\frac{\Delta Z(0^\circ)}{\bar{Z}(0^\circ)}$$

$$B = \frac{1}{2}\left\{\frac{\Delta V_P(0^\circ)}{\bar{V_P}(0^\circ)} - \left[\frac{2\bar{V_S}(0^\circ)}{\bar{V_P}(0^\circ)}\right]^2\frac{\Delta G(0^\circ)}{\bar{G}(0^\circ)} + \Delta\delta\right\}$$

$$C = \frac{1}{2}\left[\frac{\Delta V_P(0^\circ)}{\bar{V_P}(0^\circ)} + \Delta\varepsilon\right]$$

$$Z = \rho V_P$$

$$G = \rho V_S^2$$

$$\varepsilon = \frac{V_P(90^\circ) - V_P(0^\circ)}{V_P(0^\circ)}$$

$$\delta = 4\left[\frac{V_P(45^\circ) - V_P(0^\circ)}{V_P(0^\circ)}\right] - \varepsilon$$

Here Z, G, ρ, V_P, V_S, ε, and δ denote acoustic impedance, shear modulus, density, P- and S-wave

velocities, and Thomsen's parameters (Thomsen, 1986), respectively. In addition, ΔV_P and $\bar{V}_P$ represent the difference and average of parameters of underlying and overlying layers (similarly for other parameters). However, the above formulation can only provide an accurate estimation based on the assumptions of weak contrast and Thomsen (1986)'s weak anisotropy, although many analyses of organic-rich shale were conducted with the equation (Goodway et al., 2010; Sayers, 2013; Mesdag, 2016). The level of weak anisotropy is generally defined as about a $10 \sim 20\%$ difference in seismic velocities as defined in Thomsen (1986). Therefore, much research is still necessary to appropriately understand seismic anisotropy and make it a viable exploration tool.

To overcome the above challenges in AVO inversion and analysis, the present research investigates a non-linear AVO inversion using the full Zoeppritz equation that originally proposed by Lavaud et al. (1999). The main reason to select the method between Lavaud et al. (1999) and Zhu and McMechan (2012) is that Lavaud et al. (1999)'s formulation can theoretically compute the derivatives of reflection coefficient to the target parameter beyond the critical angle of incidence, although a practical usage of angle range above the critical angle is still challenging. On the other hand, Zhu and McMechan (2012)'s reformulation only considers non-critical PP reflection.

The first approach considers the exam of the behaviors of the nonlinear inversion using PP-reflection only. The behaviors are analyzed with a theoretical anisotropic model mainly based on experimental measurements from Tosaya (1983), Lo et al. (1986), Johnston and Christensen (1995), Vernik and Liu (1997), Hornby (1998), Sondergeld et al. (2000), and dataset collected from a well at Delaware basin. In addition, the inversion is tested with field seismic data in the Gulf of Mexico (GOM). This research leads to the development of a new joint nonlinear Zoeppritz inversion by expanding Lavaud et al. (1999)'s method. It simultaneously utilizes P-wave reflection and converted PS-reflection together along with their exact solutions from the Zoeppritz equation. The superiority of the joint inversion compared to conventional inversion using PP-reflection only is shown by Sayers et al. (2015)'s Eagle Ford model. Lastly, I propose a new workflow to determine seismic anisotropy, geomechanical properties, and TOC with the Zoeppritz inversion. The workflows are tested with a simple two-layer synthetic model that generated from the dataset of

Delaware basin. Especially, a new seismic attribute I label ΔV_P is developed for the estimation of seismic anisotropy and tested with the GOM field data.

1.3 Outline and Contributions

1.3.1 Outline

In this dissertation, I develop a new AVO inversion method to estimate elastic properties in heterogeneous, anisotropic media (or isotropic media but generating strong reflectivity). The procedure and its application are described in three additional sections beyond this outline.

In Section 2, I first introduce the reformulation of P-wave reflection in Zoeppritz equations originally proposed by Lavaud et al. (1999) and the adjoint state technique (Burger and Chavent, 1979) which is a method to efficiently compute the gradient of an object function composed of nonlinearly coupled parameters. By applying the adjoint state technique to the reformulated reflection, the gradient of the exact P-wave reflection coefficient, which is a key to allow the nonlinear AVO inversion possible, can be computed. Even though the derivation of derivatives of the P-wave reflection was originally discussed in Lavaud et al. (1999), they described it with a wrong δS_1-term, which needs to be corrected for correct inversion. Therefore, this research will illustrate the derivation more in detail and will present the correct δS_1-term for accurate implementation. Then I apply the nonlinear AVO inversion to one theoretical example based on a synthetic anisotropic model of shale and one Gulf of Mexico (GOM) field data example. These results are compared to other inversion results from industry standard linear AVO inversion methods on Fatti et al. (1994) and HampsonRussell software's simultaneous inversion (Hampson et al., 2005). The comparison will verify the effectiveness of the nonlinear Zoeppritz AVO inversion.

In Section 3, I construct a new AVO inversion jointly using exact P-wave reflection and converted PS-reflection together. The method is developed in order to overcome typical technical challenges that traditional AVO inversion methods encounter such as 1) Sensitive to SNR (signal to noise ratio), 2) Longer source-receiver offset requirement for density inversion, 3) Reliable background ratio of P- and S-wave velocities estimation and 4) Incorrect S-wave velocity estima-

tion. The Joint inversion is also based on reformulations of Zoeppritz equations (Lavaud et al., 1999) and application of the adjoint state technique (Burger and Chavent, 1979) not only for P-wave reflection but also for converted PS-reflection. Therefore, the derivation of derivatives of the converted PS-reflection is newly discussed in the section. As a next step, I apply the Joint AVO inversion to a synthetic model of Eagle Ford, which is a case of strong contrast and weak anisotropy, and compare to results from other inversions such as Fatti et al. (1994)'s linearized three-terms inversion and the nonlinear Zoeppritz inversion using P-wave reflection only. These show that the Joint AVO inversion can provide benefits to overcome the technical challenges briefly described above.

In Section 4, I describe how the nonlinear Zoeppritz inversion can be applied to both conventional and unconventional reservoir characterization. I first apply the inversion to a synthetic model developed with data of Avalon shale, which is an organic-rich shale example of the Delaware Permian basin. Specifically, I conduct a sensitivity test with various source-receiver offsets (i.e., angles of incident) and provide a detailed analysis of the inversion results. Then, I propose a workflow based on the analysis to estimate seismic anisotropy, geomechanical properties, and organic abundance of organic-rich shale. I also introduce a new seismic anisotropy attribute related to the workflow. The effectiveness of the attribute is demonstrated with the GOM field data and verified with a gamma-ray log of vertical well located in the field.

In conclusion, I will summarize the nonlinear AVO inversion, and also discuss some possible improvements and further applications based on the current work.

1.4 Contributions

The research products of this dissertation will contribute to the definition of well placement, evaluate the stimulated reservoir volume (SRV), and support completion design for both conventional and unconventional reservoirs. Specifically, the nonlinear Zoeppritz AVO inversion will provide an accurate estimation of elastic parameters and their anisotropy of target reservoirs under more challenging conditions such as strong contrast and strong anisotropy. Especially, new PP- and PS-Joint AVO inversion based on Zoeppritz equations can contribute to overcoming many techni-

cal challenges into which conventional AVO method using PP-reflection only inherently bring. Better estimation of S-wave velocity, shear impedance, and Poisson's ratio can be a good example. In addition, this method does not require background ratio of P- and S-wave velocities (i.e., $\frac{\bar{V_P}}{\bar{V_S}}$) as prerequisite information before inversion. By the combination of inverted parameters with workflows proposed and described in this dissertation, we can furthermore infer important constraints such as seismic anisotropy, geomechanical properties, and TOC which evaluate both completion and reservoir qualities. In summary, this methodology has a direct influence on the drilling and development of unconventional reservoirs by identifying sweet spots and locations for effective hydraulic fracturing. Consequently, the research products can be beneficial for economically hydrocarbon exploration and production.

2. NONLINEAR AVO INVERSION BASED ON ZOEPPRITZ EQUATIONS*

2.1 Introduction

Seismic inversion is a fundamental task in geophysical studies to characterize elastic properties of subsurface layers such as seismic wave velocity, density as well as impedance. Among many seismic inversion methods, Amplitude Variation with Offset (AVO) inversion is an effective method to estimate the properties of target layers in reservoir conditions (Castagna and Backus, 1993). If AVO inversion can successfully estimate the parameters of target formations, additional physical constraints to understand the target reservoirs (e.g., porosity, types of saturated fluid, geomechanical properties, organic abundance, and etc.) can also be inferred (Castagna and Backus, 1993; Connolly, 1999; Hilterman, 2001; Chopra et al., 2013).

A general procedure of the AVO inversion is briefly summarized below:

1. Input AVO data is typically observed and collected in common-midpoint (CMP) gather from a seismic acquisition.

2. The CMP gather is converted from the domain of source-receiver offset to the domain of incident angle.

3. The observed data is compared to theoretically modeled AVO curves.

4. Minimize the error between observed and modeled variation of the reflection amplitudes (i.e., AVO) in order to estimate target parameters.

For the modeling part, the Zoeppritz equations are generally considered to represent the reflection coefficients, since they can provide analytical solutions of amplitudes for P-wave and converted PS-wave reflections with the plane wave assumption (Zoeppritz, 1919). Nonetheless, the direct application of the Zoeppritz equations for the inversion is not a trivial problem due to the

*Part of this chapter is reprinted with permission from "Inference of geomechanical properties of shales from avo inversion based on the zoeppritz equations" by Lim, U. Y., R. Gibson, N. Kabir, and D. Zhu, 2017. SEG Technical Program Expanded Abstracts 2017, 728-732, Copyright [2017] by Society of Exploration Geophysicists.

fact that the target elastic parameters are non-linearly coupled in the equations. Therefore, most conventional AVO inversions are implemented with linearized approximations of the Zoeppritz equations (Aki and Richards, 1980; Wiggins et al., 1983; Shuey, 1985; Fatti et al., 1994) instead of the Zoeppritz equations themselves. However, linearization results in a less accurate representation of wave behavior. They can only estimate the variation of reflection coefficient along with offset to an acceptable level of accuracy when target reservoirs have weak contrasts in properties, seismic isotropy, and relatively small range of incident angle. As a result, conventional AVO inversions cannot correctly estimate elastic parameters of some geologically important formations which are highly anisotropic and often surrounded by hard layers generating strong contrasts. For example, organic-rich shale formations are often characterized as being anisotropic (Vernik and Nur, 1992; Sondergeld et al., 2000). Sayers et al. (2015) also shows that the level of anisotropy increases when the volume fraction of total organic content (TOC) in shale increases. However, accurate characterization of shale is increasingly important as unconventional resources serve as an economically viable energy source. Although Rüger (1997) proposed an AVO equation for P-wave reflection coefficients in anisotropic media, it only provides an accurate solution based on the assumption of weak contrast and weak anisotropy; the level of weak anisotropy is generally defined as $10 \sim 20\%$ difference in seismic velocities by Thomsen (1986). However, the anisotropy level of organic-rich shale can easily exceed the weak anisotropy definition and reaches up to 40% (Vernik, 2016). In addition, a strong contrast is present, if target layers are surrounded by carbonates or salt-domes, in conventional petroleum systems. For this reason, AVO inversion based on linearized equations does not produce correct results when target reservoirs have strong contrasts and strong anisotropy (Lavaud et al., 1999; Lim et al., 2017). It is mainly due to the fact that many linear approximations are only adequate to about 30° incident angle and do not estimate correct reflection coefficients above the angle. This is directly related to the difficulty of extraction of density from AVO inversion, since the decoupling of density and P-wave velocity from estimated acoustic impedance requires correct estimation of AVO by near at critical angle (Dębski and Tarantola, 1995; Lavaud et al., 1999).

Although there have been many efforts to increase accuracy to a larger angle, most of which are based on high-order approximations (Ursin and Dahl, 1992; Wang, 1999; Ursenbach, 2002), all these approximations fail to generate correct amplitude at angles near the critical angle, compared to the Zoeppritz equation. Besides inaccurate estimation of AVO in the far angle range, the linear inversions listed above require other assumptions before inversion. For example, Fatti et al. (1994)'s three-terms inversion needs to accurately define the ratio between P-wave and S-wave velocities in advance. Although Fatti et al. (1994)'s approach is improved in the simultaneous inversion proposed by Hampson et al. (2005), their method needs to additionally assume a linear relationship between the logarithm of P-impedance and both S-impedance and density. Therefore, the utilization of the Zoeppritz equation is necessary in order to precisely invert target parameters without any prerequisite assumptions.

Following the objective of apply Zoeppritz (1919)'s complete idea, Lavaud et al. (1999) developed a nonlinear inversion by applying a reformulation of the Zoeppritz equation and an adjoint state technique. They first rewrote the Zoeppritz equation in terms of one background and three contrast parameters in P-wave and S-wave velocities and density. Then, the adjoint state technique by Burger and Chavent (1979) was applied to efficiently compute the gradient of an object function composed of the non-linearly coupled parameters. This approach makes the nonlinear inversion possible and stable when using the exact Zoeppritz equations. Therefore, target parameters can more accurately be determined by the nonlinear inversion than linearized inversions. Details of Lavaud et al. (1999)'s method will be discussed later in the section. Zhu and McMechan (2012) also presented another nonlinear inversion based on the Zoeppritz equation in a different reformulation. Zhi et al. (2013, 2016) followed Zhu and McMechan (2012)'s approach for further applications. However, the general approach of Zhu and McMechan (2012) and, Zhi et al. (2013, 2016) are variation of Lavaud et al. (1999)'s original approach.

To overcome the above challenges in AVO inversion, I apply a non-linear AVO inversion using the full Zoeppritz equation as originally proposed by Lavaud et al. (1999). The main reason to select Lavaud et al. (1999)'s method instead of Zhu and McMechan (2012) is that Lavaud et al.

(1999)'s formulation can theoretically compute the derivatives of reflection coefficient to the target parameter beyond the critical angle of incidence, although a practical usage of angle range above the critical angle is still challenging. However, Zhu and McMechan (2012)'s reformulation only considers non-critical PP reflection.

In this section, I examine and explain systematic trends of the inversion results for organic-rich shale in order to investigate the feasibility of the non-linear Zoeppritz AVO inversion for the characterization of anisotropic media. Following, I first theoretically analyze linearized isotropic and anisotropic AVO equations to identify what quantities are determined by isotropic AVO inversion in this context and how they are related to properties of an anisotropic target shale. Considering that the degree of anisotropy is controlled by the amount of kerogen in shale, the analysis will provide a clear interpretation and physical significance of the isotropic inversion on anisotropic media. In addition, I describe details of the chosen non-linear Zoeppritz AVO inversion and show how it can achieve more accurate results using the inversion instead of linearized approximations. This topic is mainly composed of descriptions for two methods: reformulation of P-wave reflection in Zoeppritz equations (Lavaud et al., 1999) and adjoint state technique (Burger and Chavent, 1979). I sequentially present the modeling and inversion results that validate the trends identified from the theoretical analysis and show the superiority of the AVO inversion based on the full Zoeppritz solutions to characterize anisotropic shale compared with other linearized methods. I will also briefly discuss how the inversion is further applicable for the estimation of anisotropy and geomechanical properties of organic-rich shale. For the above inversion conclusions, simple two-layer models are used. The models are developed from an analysis of experimental measurements for 11 shale formations from different basins in the world. Lastly, I provide a field data example. Although the data does not target unconventional shale, this example shows how the non-linear Zoeppritz inversion can contribute to better density estimation than a linearized inversion.

2.2 Theory: Inversion Behavior Analysis

Inversion of far-offset seismic reflection data will have improved accuracy if the exact (Zoeppritz) reflection coefficient equation is modeled rather than a linearized approximation, especially

in the presence of strong contrast boundaries. Below I will summarize the approach used to achieve this goal, but first I will utilize some simpler expressions to infer what quantities are determined by inversion of reflection coefficient equations that assume isotropy when the target formation is instead anisotropic. This is directly relevant to the determination of elastic properties of shale reservoirs since many target shale formations have seismic anisotropy related to organic content. To answer this question, I consider a model with the following properties:

- A vertical transverse isotropic (VTI) shale layer is overlain by an isotropic layer.
- P- and S-wave velocities, and density, for the isotropic layer are known and values for the anisotropic layer are unknown.

First I note that both the PP reflection coefficient expression for isotropic media described by Wiggins et al. (1983) and the solution from Rüger (1997) that considers the VTI medium have the same form,

$$R_{PP}(\theta) = A + B\sin^2\theta + C\sin^2\theta\tan^2\theta. \tag{2.1}$$

For the isotropic case, the coefficients are (Wiggins et al., 1983)

$$\begin{aligned} A &= \frac{1}{2}\frac{\Delta Z}{\bar{Z}} = \frac{1}{2}\frac{\Delta(\rho V_P)}{(\rho\bar{V}_P)} \\ B &= \frac{1}{2}\frac{\Delta V_P}{\bar{V}_P} - 4\left[\frac{\bar{V}_S}{\bar{V}_P}\right]^2\frac{\Delta V_S}{\bar{V}_S} - 2\left[\frac{\bar{V}_S}{\bar{V}_P}\right]^2\frac{\Delta\rho}{\bar{\rho}} \\ C &= \frac{1}{2}\frac{\Delta V_P}{\bar{V}_P}. \end{aligned} \tag{2.2}$$

The same coefficients for the anisotropic layer have more complex forms (Rüger, 1997)

$$
\begin{aligned}
A &= \frac{1}{2}\frac{\Delta Z(0^\circ)}{\bar{Z}(0^\circ)} \\
B &= \frac{1}{2}\left\{\frac{\Delta V_P(0^\circ)}{\bar{V_P}(0^\circ)} - \left[\frac{2\bar{V_S}(0^\circ)}{\bar{V_P}(0^\circ)}\right]^2 \frac{\Delta G(0^\circ)}{\bar{G}(0^\circ)} + \Delta\delta\right\} \\
C &= \frac{1}{2}\left[\frac{\Delta V_P(0^\circ)}{\bar{V_P}(0^\circ)} + \Delta\varepsilon\right] \\
Z &= \rho V_P \\
G &= \rho V_S^2 \\
\varepsilon &= \frac{V_P(90^\circ) - V_P(0^\circ)}{V_P(0^\circ)} \\
\delta &= 4\left[\frac{V_P(45^\circ) - V_P(0^\circ)}{V_P(0^\circ)}\right] - \varepsilon.
\end{aligned}
\tag{2.3}
$$

Here Z, G, ρ, V_P, V_S, ε, and δ denote acoustic impedance, shear modulus, density, P- and S-wave velocities, and Thomsen's parameters (Thomsen, 1986), respectively. In addition, ΔV_P and $\bar{V}_P$ represent the difference and average of parameters of underlying and overlying layers (similarly for other parameters).

If a set of measured amplitudes is fit to equation 2.1, the interpretation of the coefficient C will depend on which model is used. I can examine the implications by setting the values of C for the two cases to be equal, using a superscript ISO for the isotropic result, and VTI for values from the Rüger (1997) equation:

$$
\frac{\Delta V_P^{ISO}}{\bar{V_P^{ISO}}} = \frac{\Delta V_P^{VTI}(0^\circ)}{\bar{V_P^{VTI}}(0^\circ)} + \varepsilon_2. \tag{2.4}
$$

Here $\Delta\varepsilon$ is the same as the value of the parameter for the shale only, ε_2 since the upper layer is isotropic. Substituting the expression for ε from equation 2.3 and setting

$$
V_{P2}^{VTI}(90^\circ) = V_{P2}^{VTI}(0^\circ)/(1+\varepsilon_2), \tag{2.5}
$$

it can be shown that the estimated velocity for the lower layer determined by the isotropic inversion

is, to first order in ε,

$$V_{P2}^{EST} \approx V_{P2}^{VTI}(90^\circ) + \frac{\left[V_{P1}^{ISO} - V_{P2}^{VTI}(90^\circ)\right]^2}{4V_{P1}^{ISO}}\varepsilon_2 \tag{2.6}$$

Therefore, the inverted P-wave velocity for the lower layer is approximately equal to its horizontal P-wave velocity for small ε (weak anisotropy).

To develop a similar result for the inverted density, I compare AVO intercepts A in equations 2.3 and 2.2 to obtain

$$\rho_2^{EST} = \frac{V_{P2}^{VTI}(0^\circ)}{V_{P2}^{EST}}\rho_2^{VTI}, \tag{2.7}$$

where ρ_2^{EST} denotes the inverted density for the underlying layer. Using equation 2.5 and setting $V_{P2}^{EST} = V_{P2}^{VTI}(90^\circ)$ in equation 2.7, I approximate the inverted density as

$$\rho_2^{EST} \approx \frac{V_{P2}^{VTI}(0^\circ)}{V_{P2}^{VTI}(90^\circ)}\rho_2^{VTI} = \frac{1}{1+\varepsilon_2}\rho_2^{VTI}. \tag{2.8}$$

This illustrates that the inverted density will be underestimated with the anisotropy level of the P-wave velocity of the underlying VTI layer. This is expected since the horizontal velocity is generally larger than the vertical wave speed.

These results provide insights into the expected results from AVO analysis in the scenario I have selected. For the tests presented below, however, I will apply a general, non-linear inversion of the exact reflection coefficients. The purpose will be to verify the predictions based on the preceding analysis and to show the improved insights that are obtained from the nonlinear inversion compared to conventional linearized, approximate solutions. However, details of the chosen non-linear Zoeppritz AVO inversion will first be illustrated in the following part before presenting the tests.

2.3 Methodology

This section presents the chosen non-linear Zoeppritz AVO inversion, which is mainly composed of descriptions for two methods: reformulation of P-wave reflection in Zoeppritz equations (Lavaud et al., 1999) and adjoint state technique (Burger and Chavent, 1979). The above-mentioned reformulation makes the computation of the exact P-wave reflection coefficient possible. And the adjoint state technique is applied to differentiate the coefficient for the inversion.

2.3.1 Reformulation of Zoeppritz equations: R_{PP}

To implement the AVO inversion based on the Zoeppritz equations, I apply a nonlinear inversion of the exact reflection coefficients proposed by Lavaud et al. (1999). They rewrote the equations in terms of the following three contrast and one background parameters that allow more effective implementation of inversion:

$$\begin{aligned} e_p &= (\alpha_2^2 - \alpha_1^2)/(\alpha_2^2 + \alpha_1^2) && \text{(P-wave velocity contrast)} \\ e_s &= (\beta_2^2 - \beta_1^2)/(\beta_2^2 + \beta_1^2) && \text{(S-wave velocity contrast)} \\ e_d &= (\rho_2 - \rho_1)/(\rho_2 + \rho_1) && \text{(density contrast)} \\ \chi &= 2(\bar{\beta}^2)/(\bar{\alpha}^2), && \text{(background parameter)} \end{aligned} \tag{2.9}$$

where α, β, and ρ indicate P-wave velocity, S-wave velocity and density, and subscripts 1 and 2 represent the upper and lower layers, respectively. $\bar{\alpha}$ and $\bar{\beta}$ are averages of parameters of underlying and overlying layers. Then, the exact PP-reflection can be formulated as (Lavaud et al., 1999):

$$R_{PP} = \frac{P - Q}{P + Q}, \tag{2.10}$$

using the intermediate variables depicted below

$$
\begin{aligned}
e &= e_s + e_d \\
f &= 1 - e_d^2 \\
S_1 &= \chi(1 + e_p) \\
S_2 &= \chi(1 - e_p) \\
T_1 &= \frac{2}{1 - e_s} \\
T_2 &= \frac{2}{1 + e_s} \\
q^2 &= S_1 \sin^2\theta \\
M_1 &= \sqrt{S_1 - q^2} \\
M_2 &= \sqrt{S_2 - q^2} \\
N_1 &= \sqrt{T_1 - q^2} \\
N_2 &= \sqrt{T_2 - q^2} \\
D &= eq^2 \\
A &= e_d - D \\
K &= D - A \\
B &= 1 - K \\
C &= 1 + K \\
Q &= M_2(C^2 N_2 + f N_1) + 4q^2 A^2 \\
P &= M_1(B^2 N_1 + f N_2) + 4eDM_1 M_2 N_1 N_2
\end{aligned}
\tag{2.11}
$$

The value of this approach is that allows expressing the exact PP-reflection coefficients with only the above four parameters (e_p, e_s, e_d, and χ) instead of six (α_1, α_2, β_1, β_2, ρ_1 and ρ_2). This also makes it more straightforward to perform nonlinear inversion using the exact reflection coefficient solutions though the coefficient equation is still complicated.

2.3.2 Least-squares formulation of AVO inversion using R_{PP}

After the reformulation, I apply a least-squares approach to AVO inversions based on this new parameterization. I consider the inverse problem as the minimization of a residual error function E to characterize the least-squares error between measured and forward modeled (computed) PP-reflection coefficients as follows:

$$E(x) = \frac{1}{2} \sum_{i=1}^{N_{obs}} \| R^c_{i\ PP}(x) - R^m_{i\ PP} \|^2, \tag{2.12}$$

where $R^m_{i\ PP}$ and $R^c_{i\ PP}$ are the measured and forward modeled (computed) PP-reflection coefficients at the angle of incidence, θ_i, and N_{obs} is the number of angles of incidence.

To minimize the error, I apply a quasi-Newton method that requires computation of the ∇R_{PP} with respect to e_p, e_s, e_d, and χ. I overcome the difficulty in differentiating PP-reflection coefficients in equation 2.10 by use of the adjoint state technique (Burger and Chavent, 1979). The theory of the technique will be described below. For further description, I call *model vector* the vector

$$x = (e_p, e_s, e_d, \chi) \in \mathbb{R}^4 \tag{2.13}$$

of all quantities that are input to the calculation of R_{PP}, and *state vector* the vector

$$y = (e, f, S_1, S_2, \ldots, P, Q, R_{PP}) \in \mathbb{R}^{19} \tag{2.14}$$

that are made of all quantities in equations 2.10 and 2.11 one has to compute to solve the state equations. I also set up a *data vector*

$$z = (R^m_{1\ PP}, \ldots, R^m_{N_{obs}\ PP}) \in \mathbb{R}^{N_{obs}} \tag{2.15}$$

which is to be compared to the *output vector*

$$v = (R^c_{1\ PP}, \ldots, R^c_{N_{obs}\ PP}) \in \mathbb{R}^{N_{obs}} \tag{2.16}$$

of reflection coefficients computed by equation 2.10. Then I can write

$$v = M \begin{bmatrix} y_1 \\ . \\ . \\ . \\ y_{N_{obs}} \end{bmatrix}, \tag{2.17}$$

where y_i is given by for θ_i, $i = 1, \ldots, N_{obs}$ and M is an *observation operator*.

2.3.3 Adjoint state technique

The adjoint state technique (Burger and Chavent, 1979) is a method to efficiently compute the gradient of an object function composed of non-linearly coupled parameters. The gradient can be computed through the resolution of a linear adjoint equation that takes the parameters in a model vector and the intermediate quantities in a state vector for the evaluation of the object function.

To illustrate the essence of the adjoint state technique, let me define the object function, the model vector, the state vector, and the output vector as R, x, y, and v, respectively. In addition, a mapping φ is introduced by the following:

$$\varphi : x \rightsquigarrow v, \tag{2.18}$$

that is given by

$$\begin{aligned} x \in \mathbb{R}^n &\rightsquigarrow y \in Y \quad \text{(solution of } e_j(x,y) = 0) \\ y \in Y &\rightsquigarrow v = M(y) \in \mathbb{R}^{N_{obs}}, \end{aligned} \tag{2.19}$$

where Y, $e_j(x,y) = 0$, and $M(y)$ are an affine state-space of dimension p, a set of p state equation, and an observation operator, respectively. Then the Lagrangian of the objective function R is expressed as

$$\mathcal{L}(x,y,\omega) = R(x,v) + \sum_{j=1}^{p} e_j(x,y)\omega_j \quad \text{for any } x \in \mathbb{R}^n, y \in \mathbb{R}^p, v \in \mathbb{R}^{N_{obs}}, \omega \in \mathbb{R}^p \tag{2.20}$$

If y_x is defined as the solution for input model x, $e_j(x,y_x) = 0$ for all $j = 1,\ldots,p$ by definition. Hence, for any choice of the multiplier vector $\omega \in \mathbb{R}^p$, it obviously leads

$$R(x,v) = \mathcal{L}(x,y,\omega) \quad \text{for any } x \in \mathbb{R}^n \tag{2.21}$$

Differentiation of equation 2.21 with respect to x (for any fixed ω) gives

$$\delta R = \frac{\partial \mathcal{L}}{\partial x}\delta x + \frac{\partial \mathcal{L}}{\partial y}\delta y \tag{2.22}$$

The need for computing δy can be eliminated by taking advantage of the fact that any multiplier ω

can be used: ω can be chosen in such way that the second term in right-hand side of equation 2.22, $\frac{\partial \mathcal{L}}{\partial y}\delta y$, vanishes for any $\delta y \in \mathbb{R}^p$. This is the essence of the adjoint state technique where I can choose ω such that:

$$\frac{\partial \mathcal{L}}{\partial y}(x, y, \omega)\delta y = 0 \quad \text{for any } \delta y \in \mathbb{R}^p \tag{2.23}$$

Then equation 2.22 reduces to

$$\delta R = \frac{\partial \mathcal{L}}{\partial x}\delta x \quad \text{for any } \delta x \in \mathbb{R}^n \tag{2.24}$$

Consequently, the partial derivatives of the object function with respect to the model vector (i.e., $\nabla_x R$) can only be composed of the parameters in the model vector x and the multiplier ω, which satisfies the condition in equation 2.23.

2.3.4 Derivatives of R_{PP}

Once the model vector (x), the state vector (y), the data vector (z) and the output vector (v) are set as in equations 2.13, 2.14, 2.15, and 2.16, the solution of derivatives of R_{PP} is determined from the joint use of the reformulation and the adjoint state technique. The solution was originally discussed in Lavaud et al. (1999), but with the wrong δS_1-term. Specifically, they omitted the sinusoidal contribution of incident angle for the δS_1-term. Therefore, I correct the term and present the accurate solution of derivatives of R_{PP} with respect to the model vector as

$$\begin{aligned}
\frac{\partial R_{PP}}{\partial \chi} &= -(1+e_p)\omega_3 - (1-e_p)\omega_4 \\
\frac{\partial R_{PP}}{\partial e_p} &= \chi\omega_4 - \chi\omega_3 \\
\frac{\partial R_{PP}}{\partial e_s} &= -\omega_1 - \frac{2\omega_5}{(1-e_p)^2} + \frac{2\omega_6}{(1+e_s)^2} \\
\frac{\partial R_{PP}}{\partial e_d} &= -\omega_1 + 2e_d\omega_2 - \omega_3,
\end{aligned} \tag{2.25}$$

where ω_1, ω_2, ..., ω_6 are

$$
\begin{aligned}
\omega_1 =& \frac{q^2}{P+Q}\big[8Aq^2(-R_{PP}-1)+4BM_1N_1(1-R_{PP}) \\
& -4CM_2N_2(-R_{PP}-1)-4eM_1M_2N_1N_2(1-R_{PP})\big] \\
& -\frac{4DM_1M_2N_1N_2(1-R_{PP})}{P+Q} \\
\omega_2 =& \frac{M_2N_1(R_{PP}+1)-M_1N_2(1-R_{PP})}{P+Q} \\
\omega_3 =& \frac{\sin^2\theta}{2(P+Q)}\Big\{8A^2(R_{PP}+1)+8e(-2Aq^2R_{PP}-2Aq^2-BM_1N_1(R_{PP}-1) \\
& +CM_2N_2(R_{PP}+1)+eM_1M_2N_1N_2R_{PP}-eM_1M_2N_1N_2) \\
& -\frac{(R_{PP}-1)\big[B^2N_1+N_2(4DeM_2N_1+f)\big]}{M_1} \\
& +\frac{B^2(M_1-M_1R_{PP})-M_2(4DeM_1N_2(R_{PP}-1)+f(R_{PP}+1))}{N_1} \\
& +\frac{f(M_1-M_1R_{PP})-M_2\big[C^2(R_{PP}+1)+4DeM_1N_1(R_{PP}-1)\big]}{N_2} \\
& -\frac{N_2\big[C^2(R_{PP}+1)+4DeM_1N_1(R_{PP}-1)\big]+fN_1(R_{PP}+1)}{M_2}\Big\} \\
& +\frac{(R_{PP}-1)\big[B^2N_1+N_2(4DeM_2N_1+f)\big]}{2(P+Q)M_1} \\
\omega_4 =& \frac{N_2\big[C^2(R_{PP}+1)+4DeM_1N_1(R_{PP}-1)\big]+fN_1(R_{PP}+1)}{2M_2(P+Q)} \\
\omega_5 =& \frac{B^2(M_1-M_1R_{PP})-M_2\big[4DeM_1N_2(R_{PP}-1)+f(R_{PP}+1)\big]}{2(e_s-1)N_1(P+Q)} \\
\omega_6 =& \frac{M_2\big[C^2(R_{PP}+1)+4DeM_1N_1(R_{PP}-1)\big]+fM_1(R_{PP}-1)}{2(e_s+1)N_2(P+Q)}
\end{aligned}
\tag{2.26}
$$

And the solutions of ω_1, ω_2, ..., ω_6 are achieved by equating total derivative of variables (in equation 2.11) in following adjoint equation to zero:

$$
\begin{aligned}
&\delta R_{PP}\left[1+(P+Q)\omega_{19}\right]+\delta P\left[\omega_{17}-(1-R_{PP})\omega_{19}\right]+\delta Q\left[\omega_{18}+(1+R_{PP})\omega_{19}\right]\\
&+\delta C(\omega_{16}-2CM_2N_2\omega_{18})+\delta B(\omega_{15}-2BM_1N_1\omega_{17})\\
&+\delta K(\omega_{14}+\omega_{15}-\omega_{16})+\delta A(\omega_{13}+\omega_{14}-8Aq^2\omega_{18})\\
&+\delta D(\omega_{12}+\omega_{13}-\omega_{14}-4eM_1M_2N_1N_2\omega_{17})\\
&+\delta N_2\left[2N_2\omega_{11}-(fM_1+4DeM_1M_2N_1)\omega_{17}-C^2M_2\omega_{18}\right]\\
&+\delta N_1\left[2N_1\omega_{10}-(B^2M_1+4DeM_1M_2N_2)\omega_{17}-fM_2\omega_{18}\right]\\
&+\delta M_2\left[-4DeM_1N_1N_2\omega_{17}-(fN_1+C^2N_2)\omega_{18}+2M_2\omega_9\right]\\
&+\delta M_1\left[-(B^2N_1+fN_2+4DeM_2N_1N_2)\omega_{17}+2M_1\omega_8\right]\\
&+\delta q^2(\omega_7+\omega_8+\omega_9+\omega_{10}+\omega_{11}-e\omega_{12}-4A^2\omega_{18})\\
&+\delta T_2\left[(-\omega_{11}+(1+e_s)\omega_6\right]+\delta T_1\left[(-\omega_{10}+(1-e_s)\omega_5\right]\\
&+\delta S_2(\omega_4-\omega_9)+\delta S_1(\omega_3-\omega_8-\omega_7\sin^2\theta)\\
&+\delta f(-M_1N_2\omega_{17}-M_2N_1\omega_{18}+\omega_2)\\
&+\delta e(\omega_1-q^2\omega_{12}-4DM_1M_2N_1N_2\omega_{17})=0
\end{aligned}
\tag{2.27}
$$

2.3.5 Estimation of V_P, V_S, and ρ from e_P, e_S, and e_D

Once the background parameter, χ, and three contrast parameters, e_p, e_s, and e_d, are estimated by minimizing the residual error function (equation 2.12) with $\nabla_x R_{PP}$ (combination of equations 2.25 and 2.26), the P-wave and S-wave velocities, and density of an underlying layer can be derived from the inverted parameters with the assumption that the model parameters of an overlying layer are known as following:

$$
\begin{aligned}
V_{P2} &= \sqrt{\frac{1+e_p}{1-e_p}} \cdot V_{P1} \\
V_{S2} &= \sqrt{\frac{1+e_s}{1-e_s}} \cdot V_{S1} \\
\rho_2 &= \frac{1+e_d}{1-e_d} \cdot \rho_1
\end{aligned}
\tag{2.28}
$$

2.4 Synthetic Case Study

In order to investigate what quantities are determined by full Zoeppritz solutions for P-wave reflection amplitudes that assume isotropy when the target formation is instead anisotropic, I consider a model with the following properties:

- A vertical transverse isotropic (VTI) shale layer is overlain by an isotropic layer.
- P- and S-wave velocities, and density, for the isotropic layer are known and values for the anisotropic layer are unknown.

With these properties, five two-layer models are generated with different values of kerogen content as shown in Table 2.1. For the lower VTI shale layer, the chosen model varies with its kerogen content ranging from 0 to 0.4 kerogen volume fraction with an increment of 0.1. The purpose of the variation of organic abundance in the lower layer is to control the anisotropy level of given models. Specifically, organic matters are generally more soft and compliant than other minerals presented in shales. Therefore, their shapes and distribution are usually anisotropic and this consequently makes organic materials an important source of anisotropy in organic-rich shales.

Data used for the model generation are from two sources:

- A database of physical properties of ten different mudrocks in Vernik (2016).
- A vertical well in the Bone Spring formation and Avalon shale of the Delaware basin.

The first database includes measured physical properties under a high confining pressure of 50 to 70 (MPa) such as P-wave velocity, S-wave velocity, their anisotropy levels with Thomsen's

Model	Kerogen (v/v)	ρ (g/cm^3)	$V_P(0°)$ (km/s)	$V_P(90°)$ (km/s)	$V_S(0°)$ (km/s)	$V_{SH}(90°)$ (km/s)	ε	γ	δ
Upper Layer	0	2.63	5.05	5.05	2.90	2.90	0	0	0
Lower Layer	0	2.58	4.49	4.95	2.77	2.99	0.11	0.09	0.06
	0.1	2.42	4.04	4.62	2.49	2.81	0.17	0.15	0.08
	0.2	2.26	3.58	4.29	2.22	2.62	0.23	0.21	0.10
	0.3	2.11	3.13	3.97	1.95	2.43	0.30	0.28	0.12
	0.4	1.95	2.67	3.64	1.68	2.24	0.36	0.34	0.14

Table 2.1: Two-layer models for the testing AVO inversions using full Zoeppritz and linearized approximations. The lower layer represents the target shale with various kerogen content. Model values are derived from analyses for 11 shale formations. The upper layer is assumed as an isotropic limestone layer.

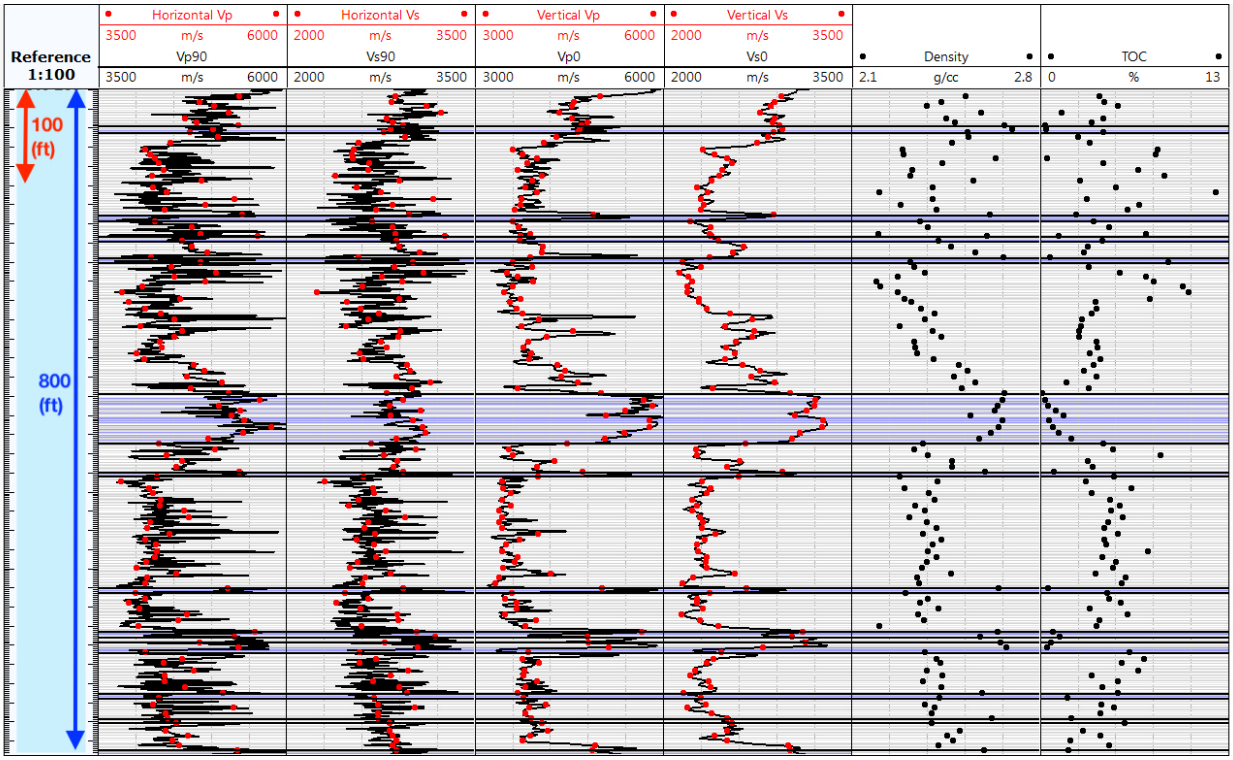

Figure 2.1: A well for Bone Spring formation and Avalon shale: $V_P(90°)$, $V_{SH}(90°)$, $V_P(0°)$, $V_S(0°)$, ρ, and TOC for 122 data points. Interbedded limestones are highlighted in blue.

parameters, bulk density, and kerogen volume fraction for ten different shale formations. The values are originally collected from Tosaya (1983); Lo et al. (1986); Johnston and Christensen

(1995); Vernik and Liu (1997); Hornby (1998); Sondergeld et al. (2000) and presented in Vernik (2016) later. Figure 2.1 shows a plot of the vertical well located at the Delaware basin, the west sub-basin of the Permian basin. It illustrates horizontal and vertical P-wave and S-wave velocities, density, and TOC for the interval considered in the model generation. The interbedded limestones with higher velocity (compared to shale) are clearly visible. Horizontal and vertical velocities are from ultrasonic measurements and open-hole logging respectively. Density and TOC values are achieved from tight rock analysis and Rock-Eval pyrolysis.

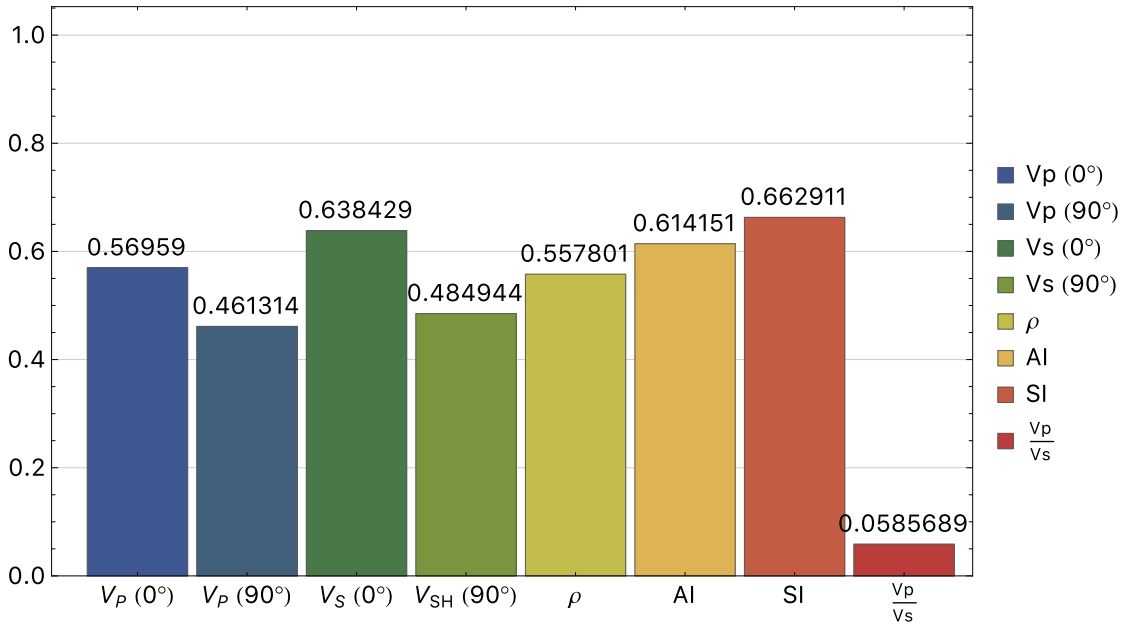

Figure 2.2: Absolute values of correlation coefficients between elastic parameters and TOC for 11 different shale formations. Note that all parameters are strongly correlated to TOC except the ratio between P- and S-wave velocities ($\frac{V_P}{V_S}$).

Velocities and density for the upper, isotropic layer of the presented model are from average values of interbedded limestones depicted in Figure 2.1. Anisotropy in the lower shale layer was determined from data from Vernik (2016) and values of the Avalon shale in the well. Since total organic carbon (TOC) content directly controls (and strongly correlated to) the elastic properties of shale as shown in Figure 2.2, I applied linear regression of the merged data to develop an empirical

model relating organic content to the density, velocities, and their anisotropy for the lower VTI shale layer. The chosen models sample the range of kerogen content in the velocity data set, ranging from 0 to 0.4 kerogen volume fraction with an increment of 0.1. The data and model values are depicted in Figures 2.3 (for P-wave velocity), 2.4 (for S-wave velocity), 2.5 (for density), and 2.6 (for seismic anisotropy). With the model values, exact anisotropic PP-reflection coefficients are computed by a paraxial ray tracing (Gibson et al., 1991), which effectively solves the two-point problem of finding the ray that connects exactly a specific source and receiver (Figure 2.7). It is possible due to the fact that the paraxial method can allow extrapolation of the information on a given ray to nearby receiver locations. The range of angle of incidence for the reflections is from 0° to 60°. These AVO curves provide test data for the AVO inversion.

Figure 2.8 compares inversion of the synthetic test data using both the nonlinear Zoeppritz approach and a more typical linearized AVO inversion based on the solution by Fatti et al. (1994), which is

$$R_{PP}(\theta) = c_1 R_P(0^\circ) + c_2 R_S(0^\circ) + c_3 R_D, \tag{2.29}$$

$$\begin{aligned}
\text{where} \quad c_1 &= 1 + \tan^2\theta \\
c_2 &= -8K \sin^2\theta \\
c_3 &= 2K \sin^2\theta - \frac{1}{2}\tan^2\theta \\
K &= \left[\frac{\bar{V_P}}{\bar{V_S}}\right]^2 \\
R_P(0^\circ) &= \frac{1}{2}\{\frac{\Delta V_P}{\bar{V_P}} + \frac{\Delta\rho}{\bar{\rho}}\} \\
R_S(0^\circ) &= \frac{1}{2}\{\frac{\Delta V_S}{\bar{V_S}} + \frac{\Delta\rho}{\bar{\rho}}\} \\
R_D &= \frac{\Delta\rho}{\bar{\rho}}.
\end{aligned}$$

Above Fatti et al. (1994)'s equation is a linearized approximation of PP reflection widely used to decouple P-wave velocity and density from acoustic impedance.

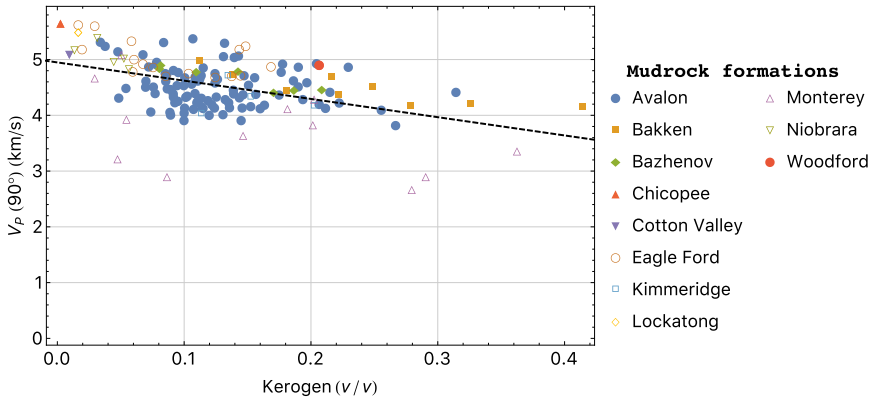

(a) Horizontal P-wave velocity, $V_P(90°)$

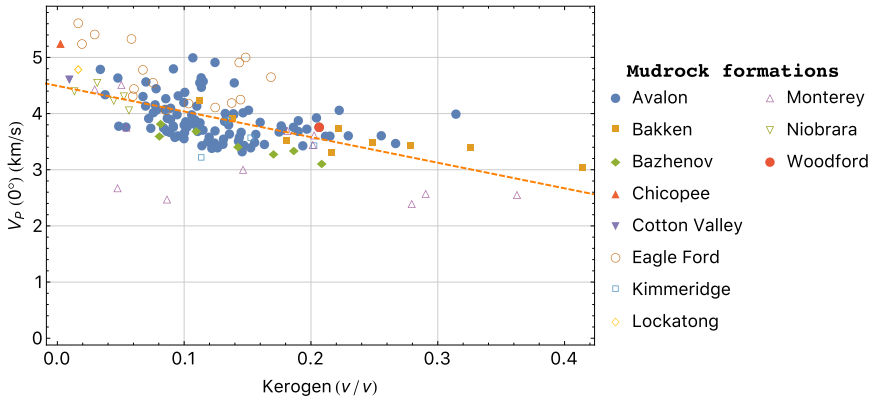

(b) Vertical P-wave velocity, $V_P(0°)$

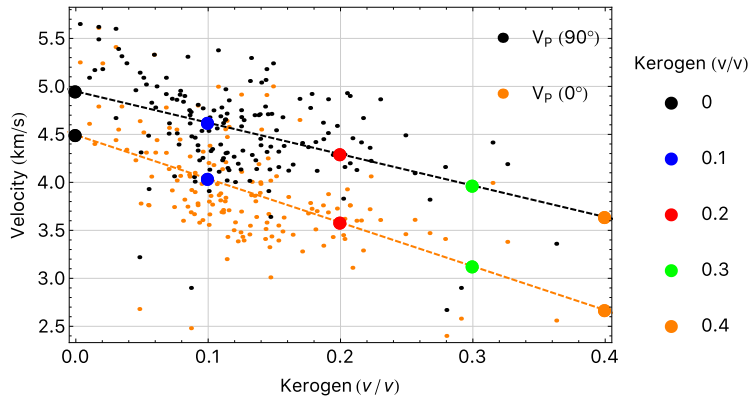

(c) $V_P(90°)$, $V_P(0°)$, and their model values

Figure 2.3: Horizontal and vertical P-wave velocities with respect to kerogen volume fraction and linear regression lines for model generation in Table 2.1. Data are from an ultrasonic measurement database for ten different shale formations (Vernik, 2016) and a vertical well for Avalon shale, Delaware basin. Note that the discrepancy between horizontal and vertical P-wave velocities increases with the increase in organic content. (i.e., Anisotropy of P-wave velocity increases.)

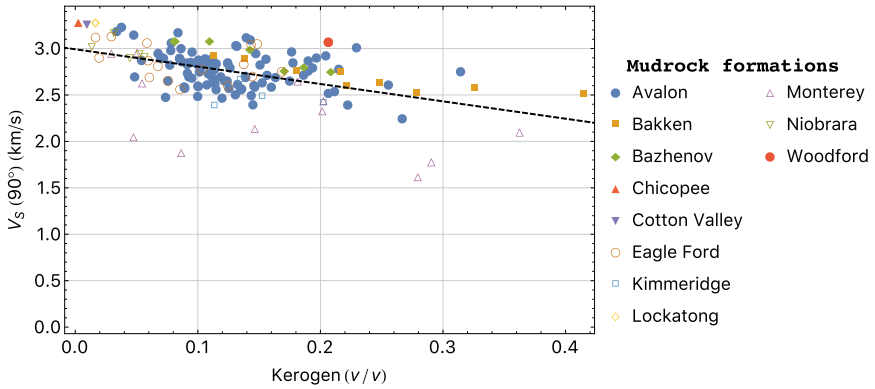

(a) Horizontal S-wave velocity, $V_S(90°)$

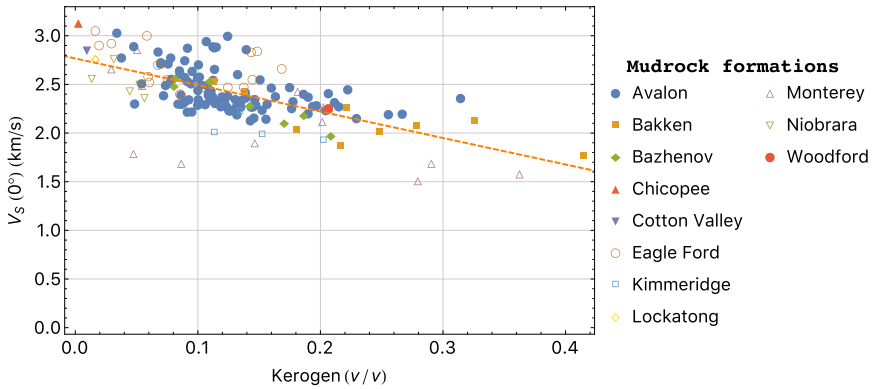

(b) Vertical S-wave velocity, $V_S(0°)$

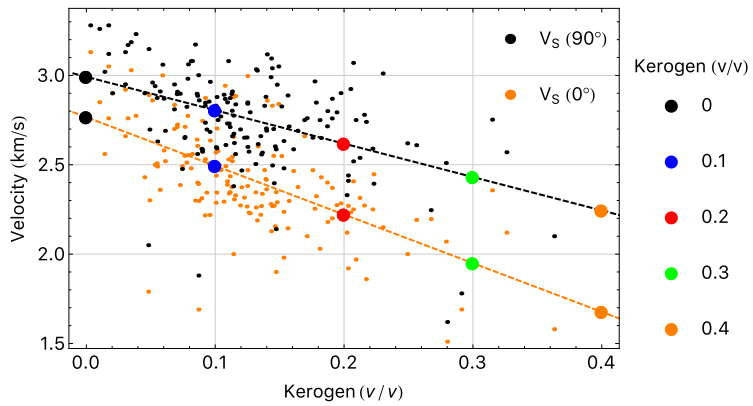

(c) $V_S(90°)$, $V_S(0°)$, and their model values

Figure 2.4: Horizontal and vertical S-wave velocities with respect to kerogen volume fraction and linear regression lines for model generation in Table 2.1. Data are from an ultrasonic measurement database for ten different shale formations (Vernik, 2016) and a vertical well for Avalon shale, Delaware basin. Note that the discrepancy between horizontal and vertical S-wave velocities increases with the increase in organic content. (i.e., Anisotropy of S-wave velocity increases.)

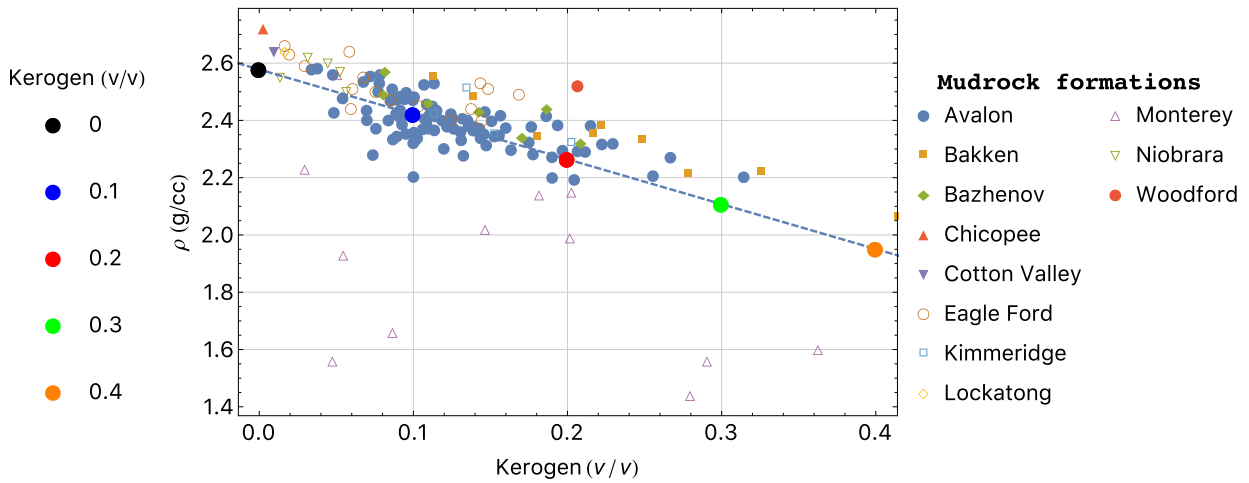

Figure 2.5: Density (ρ) and its model values. Note that model density values decrease with the increase in organic content.

Both methods accurately determine inverted acoustic (normal) impedance for all values of kerogen volume fractions. They also produce inverted velocity estimates that are close to the shale horizontal velocity for small amounts of kerogen and, therefore, low anisotropy. However, as the amount of kerogen increases, the linearized inversion produces velocity estimates that with increasingly large differences from both vertical and horizontal velocity values. The nonlinear result remains consistently close to the horizontal velocity. While the nonlinear inversion produces a density estimate that is too low, as expected from equation 2.8, the error is comparatively constant. In contrast, the linearized result has an increasing error as kerogen volume fraction increases.

Inverted parameters (i.e., P- and S-wave velocities, and density) from AVO inversions can also be used to estimate properties of interest for geomechanical analyses such as Young's modulus and Poisson's ratio. Estimated values for Young's modulus for the test models are shown in Figure 2.9(a), while Figure 2.9(b)) shows the Poisson's ratio estimates. The values are calculated by combinations of the inverted P- and S-wave velocities, and density depicted in Figure 2.8 with following general relationship among elastic constants and velocities in an isotropic medium (Birch, 1961):

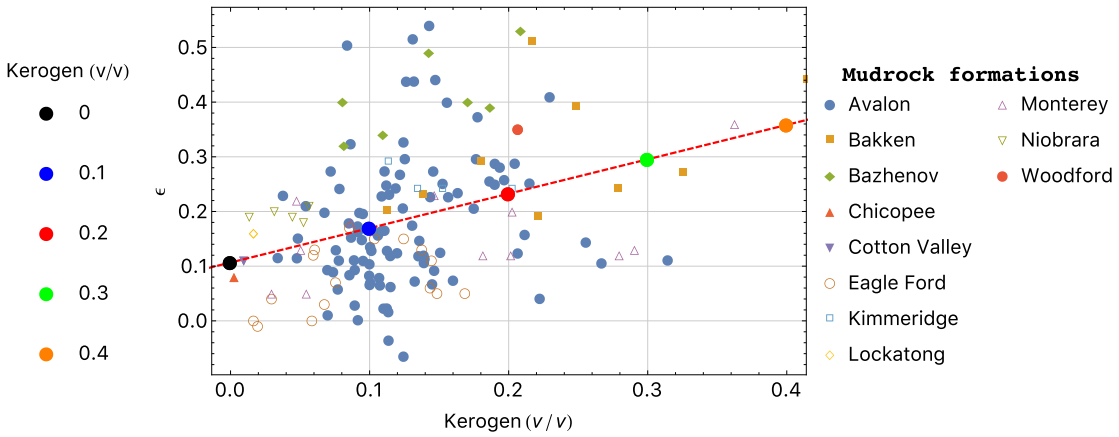

(a) ε

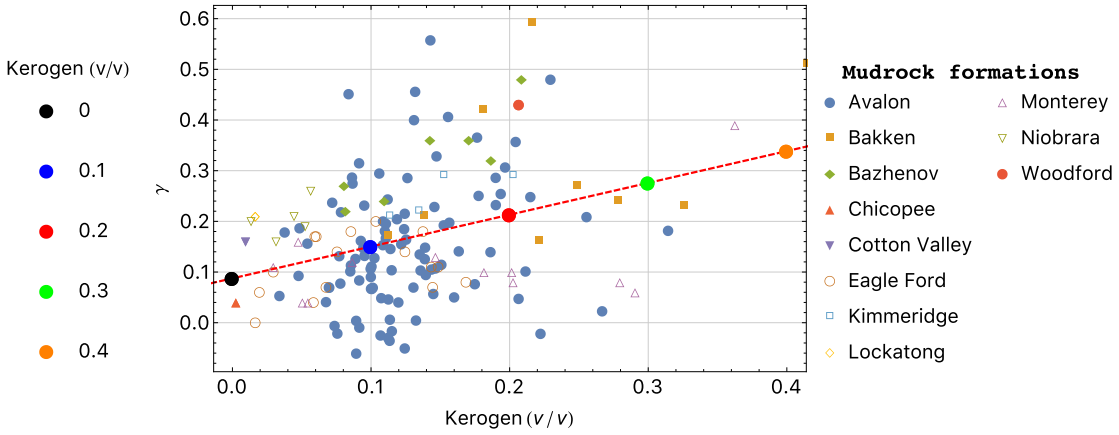

(b) γ

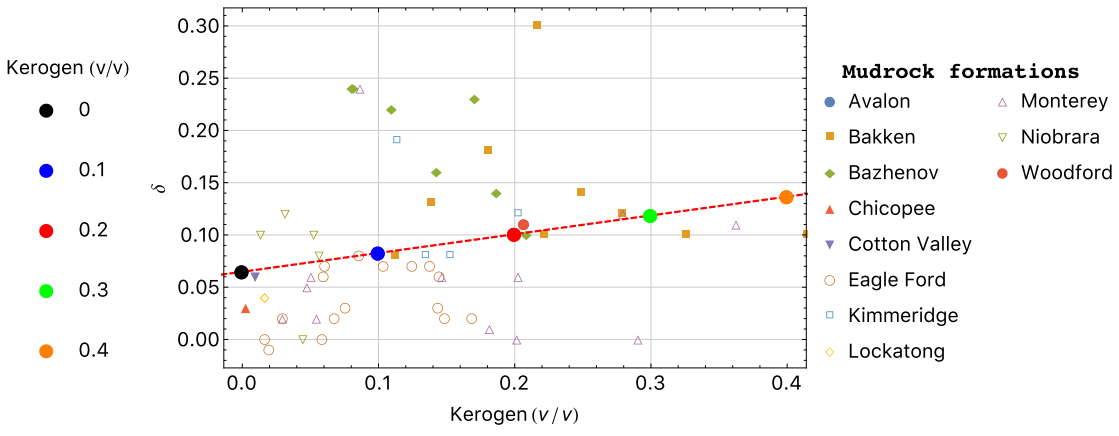

(c) δ

Figure 2.6: Measured Thomsen parameters and their model values: ε, γ, and δ. Note that model values increase with the increase in organic content.

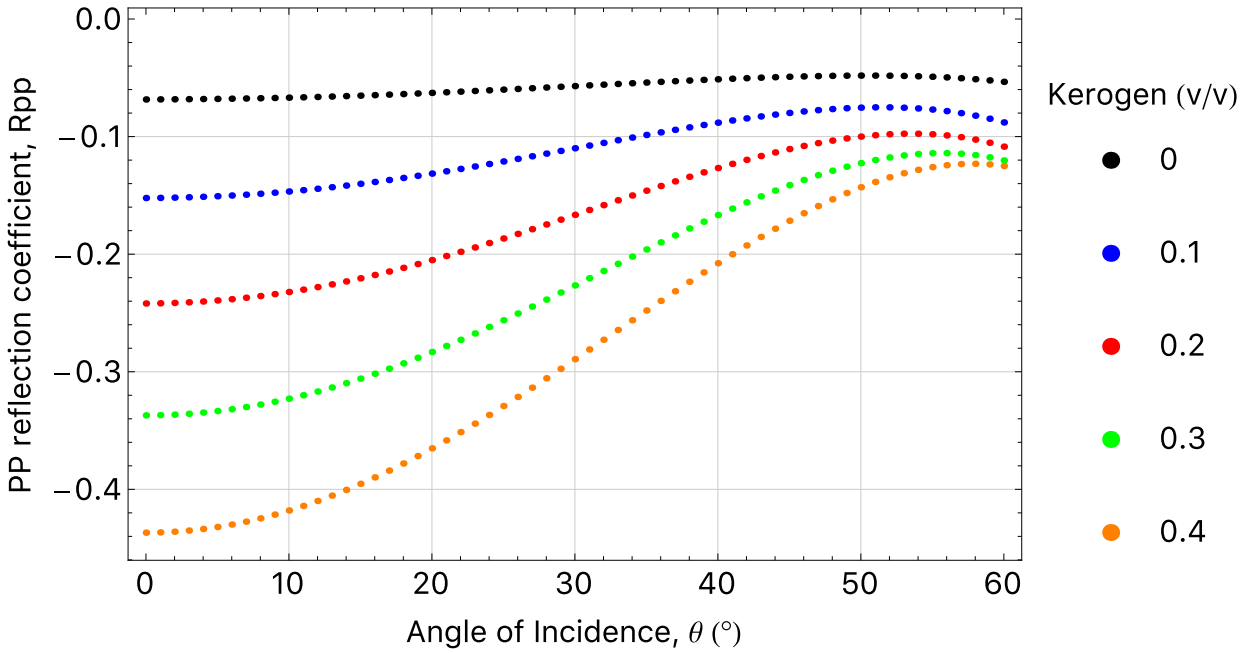

Figure 2.7: Exact anisotropic AVO responses (reflection coefficients) from the model interfaces in Table 2.1.

$$
\begin{aligned}
V_P &= \sqrt{\frac{\lambda + 2\mu}{\rho}} \\
V_S &= \sqrt{\frac{\mu}{\rho}} \\
\lambda &= ({V_P}^2 - 2{V_S}^2)\rho \\
\mu &= {V_S}^2\rho \\
k &= \lambda + \frac{2\mu}{3} \\
E &= \frac{9k\mu}{3\kappa + \mu} \\
\nu &= \frac{3k - E}{6k},
\end{aligned}
\tag{2.30}
$$

where V_P, V_S, λ, μ, k, E, and ν are compressional and shear velocities, *Lamé* parameters, bulk modulus, Young's modulus, and Poisson's ratio, respectively.

In order to determine model values of the geomechanical properties for the VTI models cor-

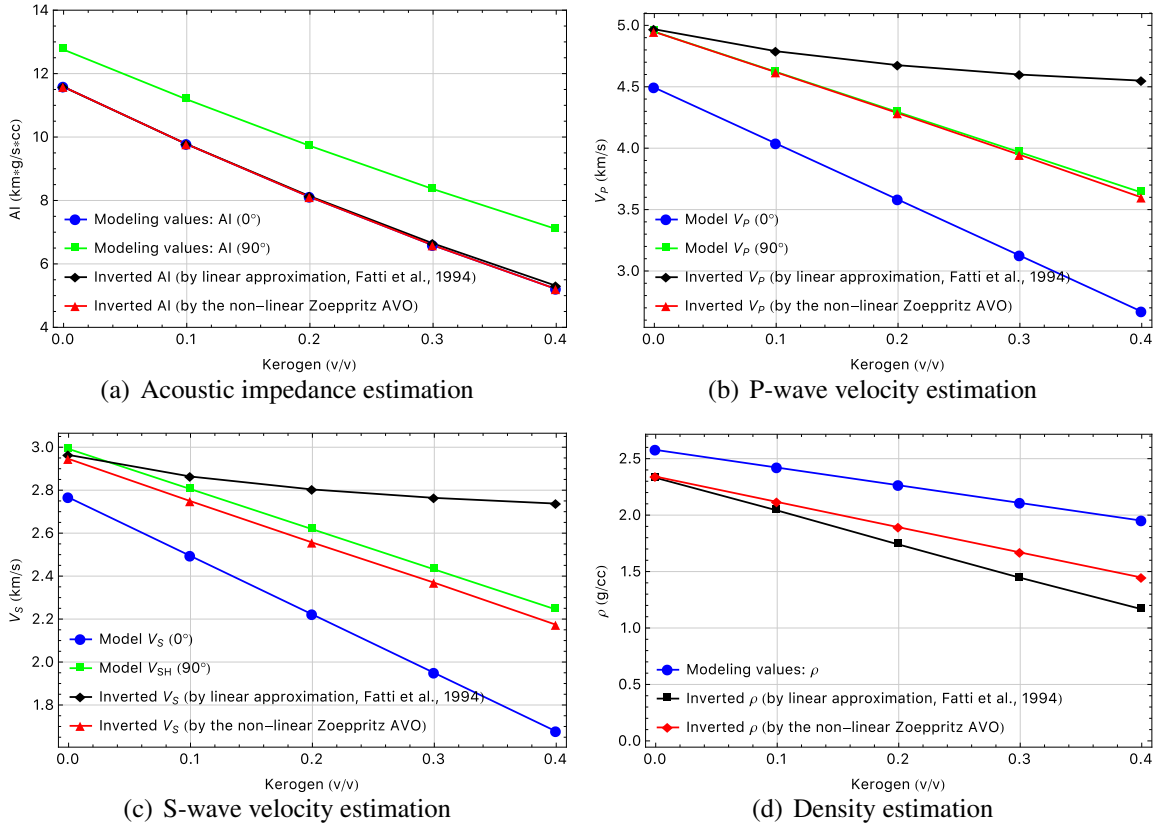

(a) Acoustic impedance estimation

(b) P-wave velocity estimation

(c) S-wave velocity estimation

(d) Density estimation

Figure 2.8: Estimated acoustic impedance, P-wave velocity and density from the nonlinear and linearized AVO inversions.

rectly, their five independent elastic stiffness coefficients first need to be computed. When the x_3 axis is the rotational symmetry axis, there are five non-vanishing coefficients such as $c_{11} = c_{22}$, $c_{12} = c_{21}$, c_{33}, $c_{44} = c_{55}$, $c_{13} = c_{31} = c_{23} = c_{32}$, and one additional $c_{66} = (c_{11} - c_{12})/2$ in the conventional *Voigt* two-index notation (Auld, 1973; Nye, 1985). Model elastic stiffness coefficients are converted from model density (ρ) and velocities (i.e., $V_P(0°)$, $V_P(90°)$, $V_P(45°)$, $V_{SH}(90°)$, and $V_S(0°) = V_{SH}(0°) = V_{SV}(0°)$) depicted in Table 2.1 with following equations:

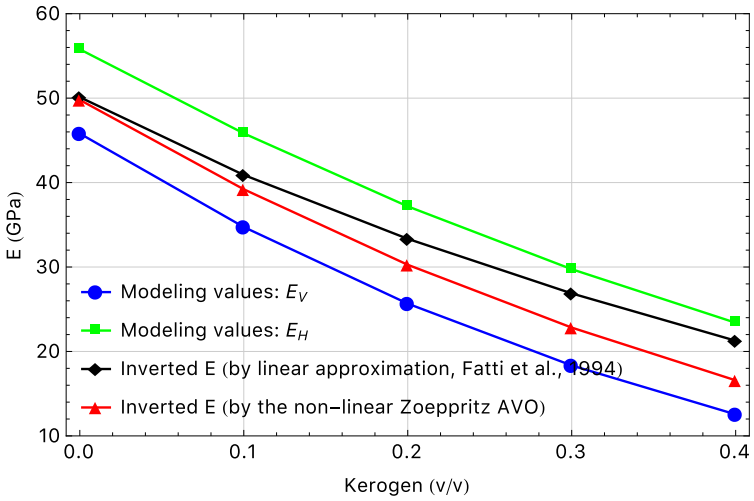

(a) Young's modulus estimation

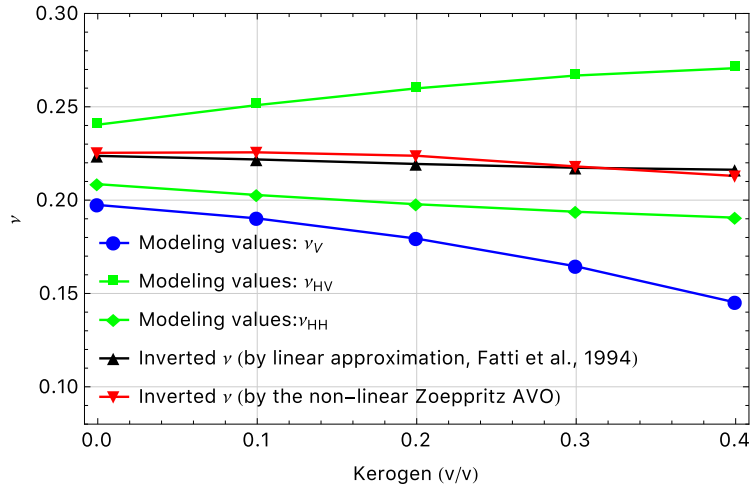

(b) Poisson's ratio estimation

Figure 2.9: Geomechanical properties results from AVO inversion.

$$
\begin{aligned}
c_{11} &= \rho V_P^2(90^\circ) \\
c_{12} &= c_{11} - 2\rho V_{SH}^2(90^\circ) \\
c_{33} &= \rho V_P^2(0^\circ) \\
c_{44} &= \rho V_S^2(0^\circ) \\
c_{13} &= -c_{44} + \sqrt{4\rho^2 V_P^4(45^\circ) - 2\rho V_P^2(45^\circ)(c_{11} + c_{33} + 2c_{44}) + (c_{11} + c_{44})(c_{33} + c_{44})}
\end{aligned}
\tag{2.31}
$$

Kerogen (v/v)	c_{11}	c_{12}	c_{13}	c_{33}	c_{44}
0	63.1	17.0	15.8	52.0	19.7
0.1	51.7	13.6	12.4	39.4	15.1
0.2	41.7	10.7	9.4	29.0	11.2
0.3	33.2	8.2	6.8	20.6	8.0
0.4	25.8	6.2	4.6	13.9	5.5

Table 2.2: Elastic stiffness coefficients for the lower VTI layers with respect to five different kerogen levels. Their unit is *GPa*.

Table 2.2 illustrates the model values of elastic stiffness coefficients. Then, model values of the geomechanical properties for the VTI models can finally be determined with the following equations that King (1964) and Banik et al. (2012) proposed:

$$\begin{aligned}
E_V &= \frac{c_{33}(c_{11}-c_{66})-c_{13}^2}{c_{11}-c_{66}} \quad (=E_3) \\
E_H &= \frac{4c_{66}(c_{33}(c_{11}-c_{66})-c_{13}^2)}{c_{11}c_{33}-c_{13}^2} \quad (=E_1=E_2) \\
\nu_V &= \frac{c_{13}}{2(c_{11}-c_{66})} \quad (=\nu_{31}=\nu_{32}) \\
\nu_{HV} &= \frac{2c_{13}c_{66}}{c_{11}c_{33}-c_{13}^2} \quad (=\nu_{13}=\nu_{23}) \\
\nu_{HH} &= \frac{c_{33}(c_{11}-2c_{66})-c_{13}^2}{c_{11}c_{33}-c_{13}^2} \quad (=\nu_{12}=\nu_{21})
\end{aligned} \tag{2.32}$$

While both inversion results show errors compared to true, anisotropic values, I note that the nonlinear approach does predict correctly the rate of change in Young's modulus with increasing the organic content. In contrast, both AVO approaches predict similar values of Poisson's ratio (Figure 2.9).

2.5 Field Case Study: Gulf of Mexico

2.5.1 Data

In this inversion application to field data, I used pre-stack seismic data along one 2D line, a part of the 3D dataset. The original 3D dataset includes 51 inlines (from No. 14500 to No. 15000 with the 10 increments) and 81 crosslines (from No. 1500 to No. 1580 with the 1 increment). Therefore, the full gird size of the 3D dataset is 4131. Among the lines, an inline (No. 14770) is chosen for testing the Zoeppritz AVO inversion. The line is composed of 81 common-midpoint (CMP) and the spacing between each two adjacent CMPs is 25 meters, and the length of the line is, therefore, 2 km. The data is sampled every 4 ms. In this example, the inversion is run from 2000 ms to 2800 ms. As a result, the total number of investigated samples in each trace is 201. As well as the seismic data, a nearby well at CMP No. 29 and an interpreted horizon in a gas-field are also investigated to characterize P-wave and S-wave velocities, and density. Figures 2.10 and 2.11 illustrate seismic data and well logs that are used in this study, respectively.

The field is located in the offshore Gulf of Mexico (GOM), specifically, the southeast of New Orleans, Louisiana. The field size is approximately 2 km by 1.25 km. One target reservoir sand in the field is the turbidite channel-levee sequence, which is named after 'M4 Sand T', and it is surrounded by shale formations. The sand is saturated with gas and condensate, and it is located at about 2550 ms below sea level at the well location as shown in Figures 2.10 and 2.11.

2.5.2 Pre-processing for AVO inversion

Typical pre-processing procedures for AVO inversion is first conducted as a preparation step. Following provides a summary of the procedures in a sequence with their parameters set for the study:

1. Angle Mute: Data for incident angles above 45° is muted to eliminate severely stretched traces by normal-moveout (NMO) correction. Incident angles are calculated by ray-tracing with a velocity field the generated from P-wave velocity log.

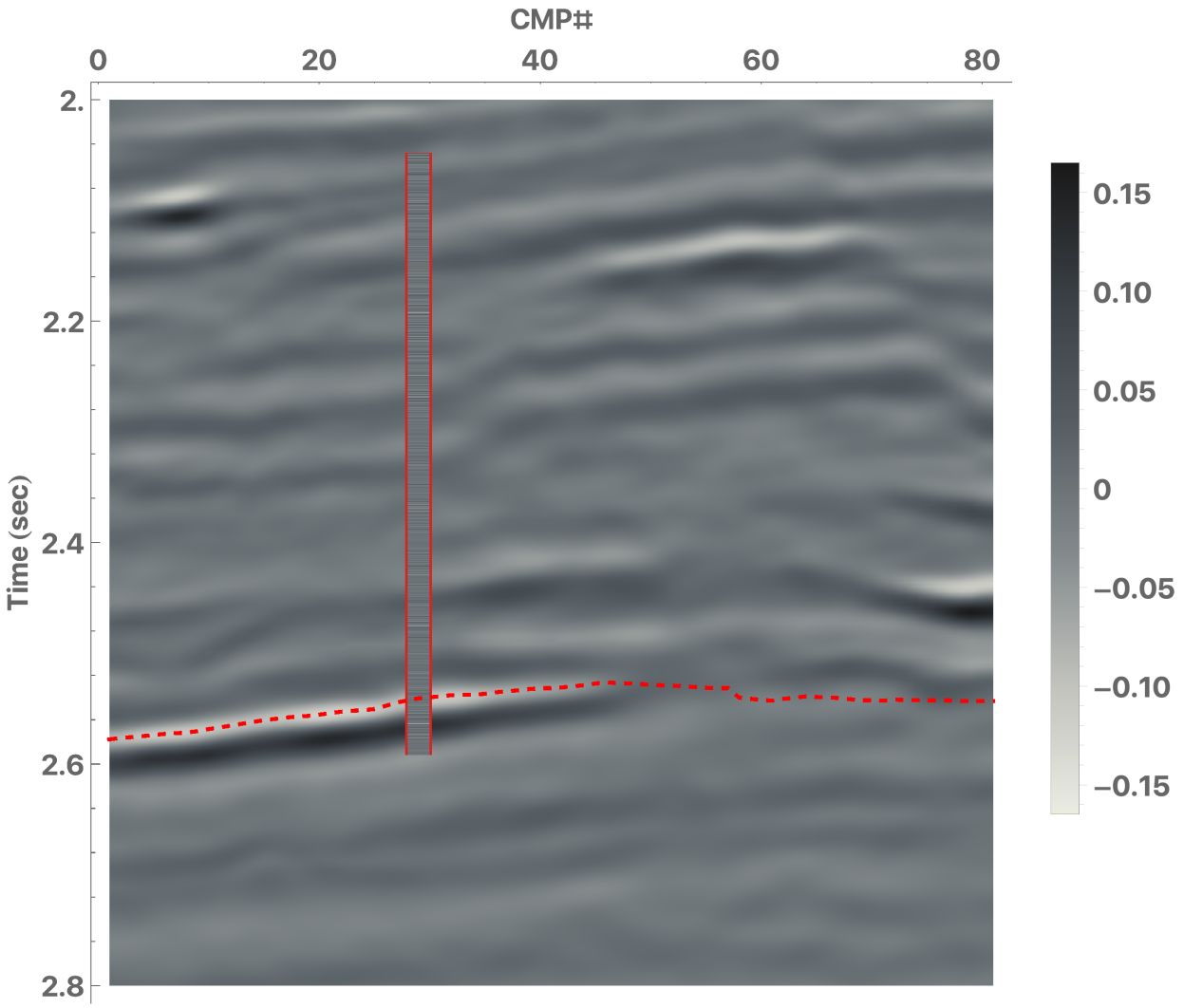

Figure 2.10: Investigated seismic data. Here, all 20 pre-stack common-angle gathers, that are used for the AVO inversion, are stacked together for a visualization purpose only. A horizon (M4 Sand T) indicated in red-dotted line and a well located at CMP No. 29 are also investigated along with the seismic data. The displayed log corresponds to reflectivity in log-scale.

2. Super Gather: In order to enhance the signal to noise ratio, super gathering, which is the process of forming average CMPs, is conducted with a rolling window 3 (inline) by 3 (xline).

3. Trim Statics: Trim statics is the process correcting for residual moveout errors and aligning reflections on the gathers. The process correlates each gather trace with the pilot trace using a specified sliding window, and calculates an optimal time shift to align target reflections. In

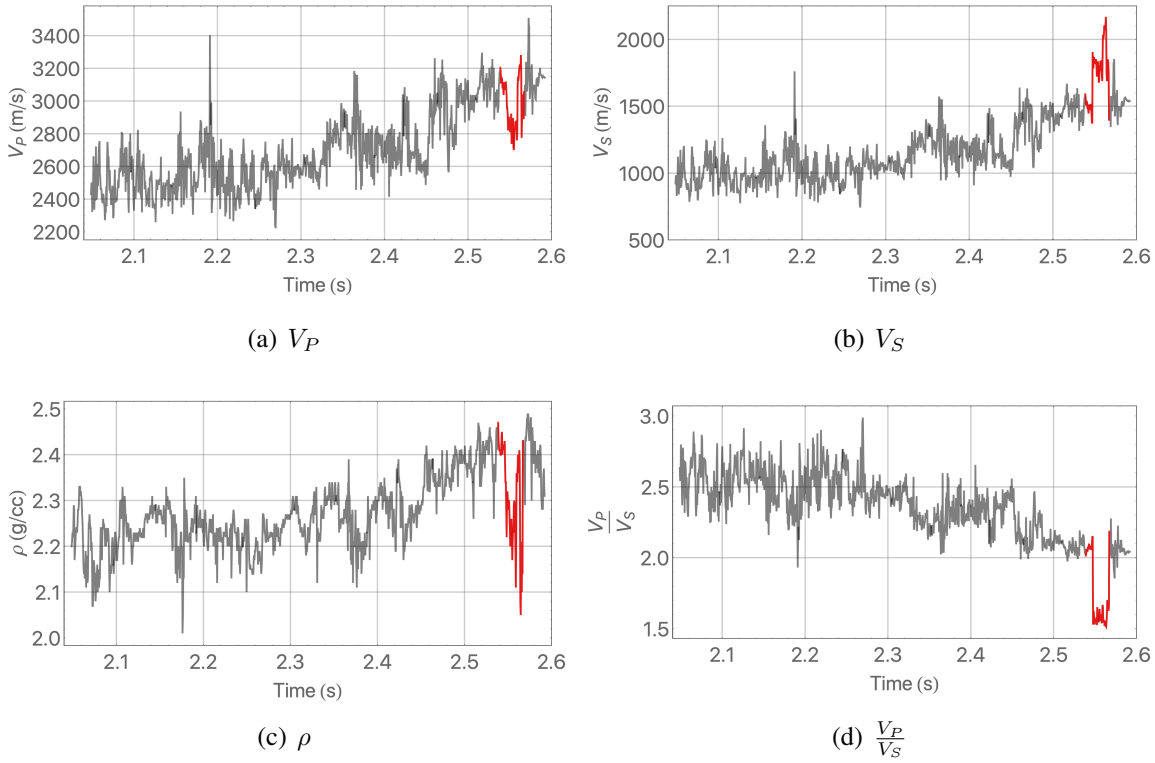

(a) V_P (b) V_S

(c) ρ (d) $\frac{V_P}{V_S}$

Figure 2.11: Logs for P-wave and S-wave velocities, density, and the ratio between P-wave and S-wave velocities. Location of target gas sand (M4 Sand T) is indicated in red.

this case, the length of the cross-correlation window is set as 80 ms with 16 ms maximum time shift.

4. Angle Gather: Lastly, an angle gather process is performed to transforms the input CMP gathers from the domain of source-receiver offset to the incident angle domain. For the process, the velocity field applied for angle mute is used again. Specifically, a total of 20 traces ranging from 4° to 42° with the 2° increments is used for the inversion on each CMP.

2.5.3 Initial Model and Inversion Results

Among many schemes for AVO inversions (e.g., recursive, band-limited, sparse-spike, model-based, and trace-based inversions), the scheme of model-based inversion is chosen for the example presented here. In the method, synthetic seismic traces are first modeled on CMP gathers by

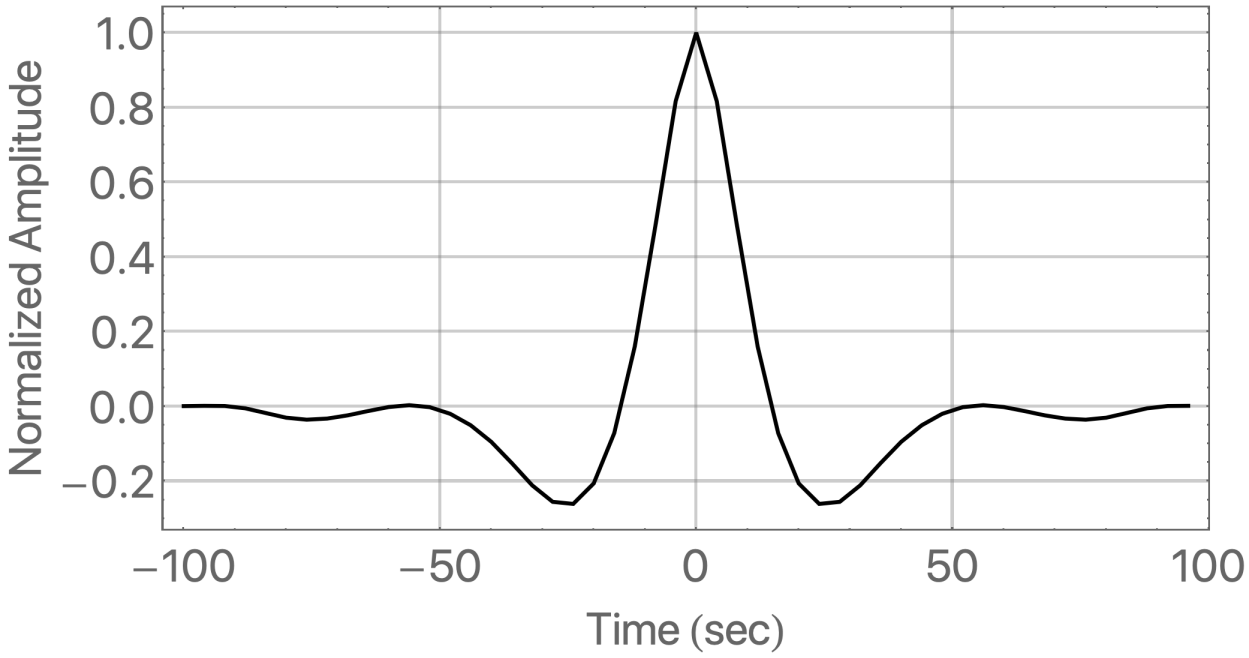

Figure 2.12: Wavelet extracted from seismic data. It is used for modeling of synthetic seismic traces and further inversion applications.

convolving a wavelet extracted from real data. Figure 2.12 shows the wavelet which was extracted from the seismic data and used for the forward modeling. Once model AVOs on CMP gathers are generated, they are compared to the real reflectivity variations. Then, their differences are used to iteratively update the model values (here, the contrast of P-wave and S-wave velocities, and density) in such a way as to better match the seismic data. After many iterations, the inversion may be possible to come up with a model that matches the data very well. However, there are infinitely many model pairs that will result in the same reflectivity as referred to as the problem of non-uniqueness (Russell, 1988).

In order to avoid the non-uniqueness, building a sound initial model before inversion is significantly important. Since the nonlinear Zoeppritz AVO inversion is also a model-based inversion and the reflection coefficients are formulated with the contrasts of P-wave and S-wave velocities, and density (i.e., e_P, e_S, e_D and χ) as described in equations 2.10 and 2.11, it is necessary to build initial models for P-wave and S-wave velocities, and density.

For the initial model building, the well logs in Figure 2.11 is used. The horizon in Figure 2.10 is also applied for the process in order to interpolate and assign the values of well logs to specified geometry along the seismic line. After the interpolation, a low-pass filter is applied to pass all frequencies up to 10 Hz and filters out all frequencies above 15 Hz. The results are shown in Figures 2.16(a) (for P-wave velocity), 2.16(d) (for S-wave velocity), and 2.16(g) (for density). Once the initial models for P-wave and S-wave velocities, and density are built, initial models for e_P, e_S, e_D and χ are also generated by equation 2.9 (Figures 2.13(a), 2.13(c), 2.13(e), and 2.13(g)).

Then, the Zoeppritz inversion starts with the initial model values and is run gather by gather for 300 iterations to minimize the misfit between model and real AVOs. Figures 2.13 depicts the initial and final models of e_P, e_S, e_D and χ. The final model of three contrasts are well conformed with the seismic structures illustrated in Figure 2.10, whereas the final model of χ is not improved from the corresponding initial model. This is due to the fact that the parameter χ is the least sensitive parameter to compute the correct reflection coefficient and is, therefore, served as a background parameter as defined as the ratio between P-wave and S-wave velocities in equation 2.9. Figures 2.14 and 2.15 present initial, final models, real seismic data, and the errors between final models and real seismic data on CMP gather and Common-angle gather, respectively. To show how well the final model fit the data, the CMP gather No. 29 related to the well location is chosen (Figure 2.14). In addition, three common angle gathers, which correspond to relatively near (10°), middle (20°), and far (30°) incident angles, are also selected (Figure 2.15). Both figures indicate that the inverted results by the Zoeppritz inversion can fit the data with high accuracy. Especially, Figure 2.14(e) shows that the root-mean-square (RMS) error between model and observed reflection at CMP No. 29 is almost converged to the smallest error after about 50 iterations.

Once e_P, e_S, e_D and χ are determined, P-wave and S-wave velocities, and density can further be estimated by recursively applying equation 2.28 to the low frequency models presented in Figures 2.16(a) (for P-wave velocity), 2.16(d) (for S-wave velocity), and 2.16(g) (for density). I compared the inversion results with those produced by commercial software, Hampson-Russell AVO (Version 10.3) using the model-based simultaneous inversion by Hampson et al. (2005). Specifi-

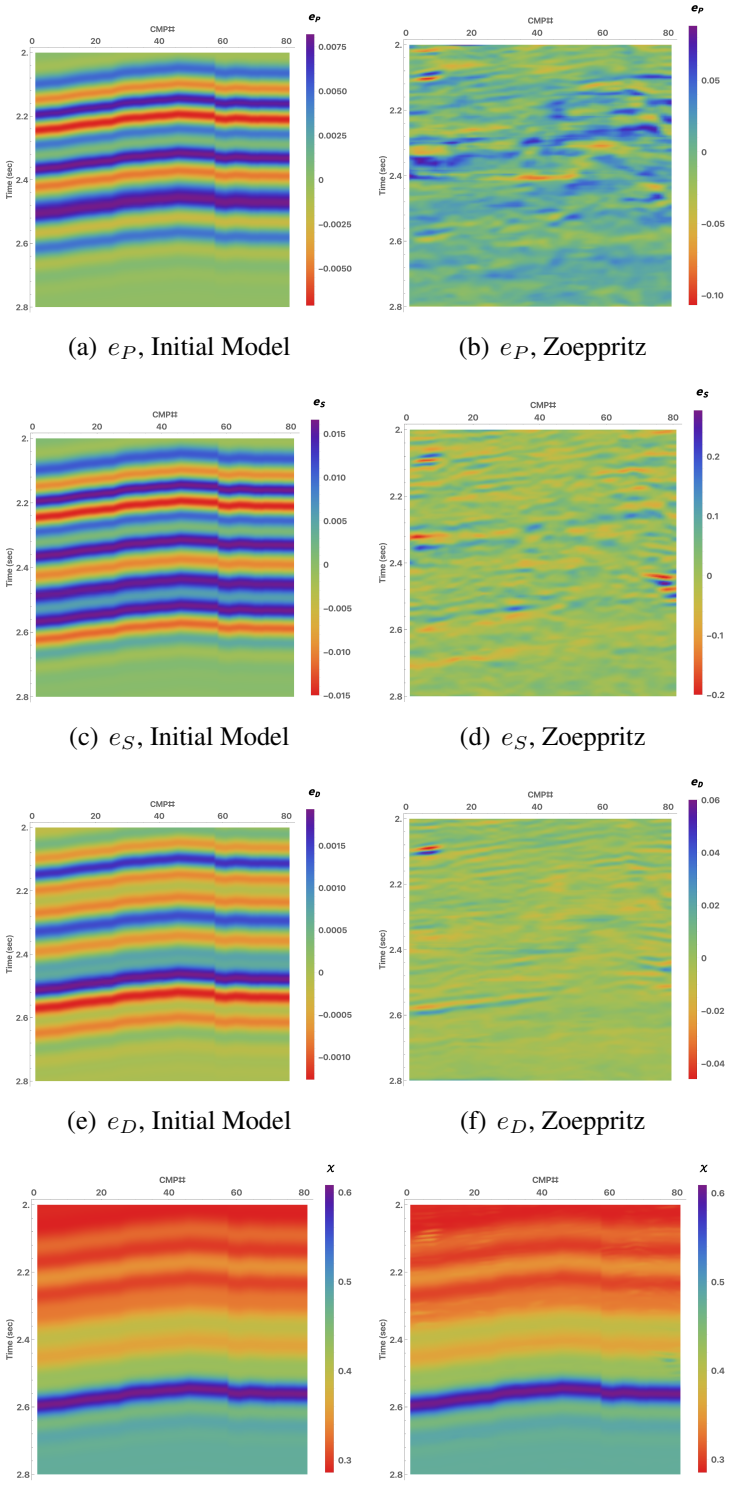

(a) e_P, Initial Model (b) e_P, Zoeppritz

(c) e_S, Initial Model (d) e_S, Zoeppritz

(e) e_D, Initial Model (f) e_D, Zoeppritz

(g) χ, Initial Model (h) χ, Zoeppritz

Figure 2.13: Initial Model and Inversion Results (e_P, e_S, e_D and χ).

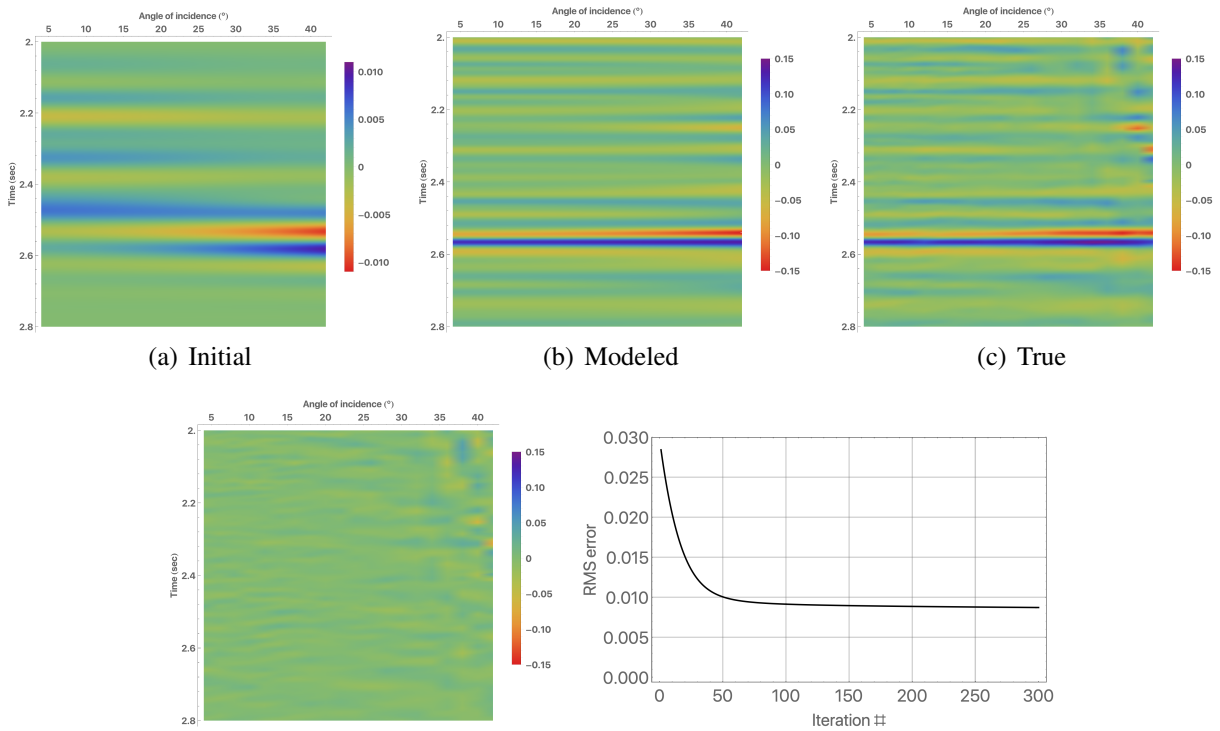

(a) Initial (b) Modeled (c) True

(d) Error (e) RMS error through iteration

Figure 2.14: Seismic CMP gathers at the well location, CMP No. 29, and RMS error through iteration.

cally, linear relationships between the logarithm of acoustic impedance and both shear impedance and density have to be assumed in order to implement the simultaneous inversion in the Hampson-Russell AVO. This background relationship can be illustrated as

$$\ln(Z_S) = 1.80\ln(Z_P) - 8.72 \tag{2.33}$$
$$\ln(\rho) = 0.31\ln(Z_P) - 2.23,$$

where Z_P, Z_S, and ρ are acoustic and shear impedances, and density, respectively. The coefficients in equation 2.33 were determined from log analyses, cross plotting, and consequent regression between set parameters. Deviations from the background relationships observed in seismic data will be used as input data and combined with Fatti's three-term equation (equation 2.29) for the Hampson-Russell's simultaneous inversion. In addition, a fixed background ratio between P-wave

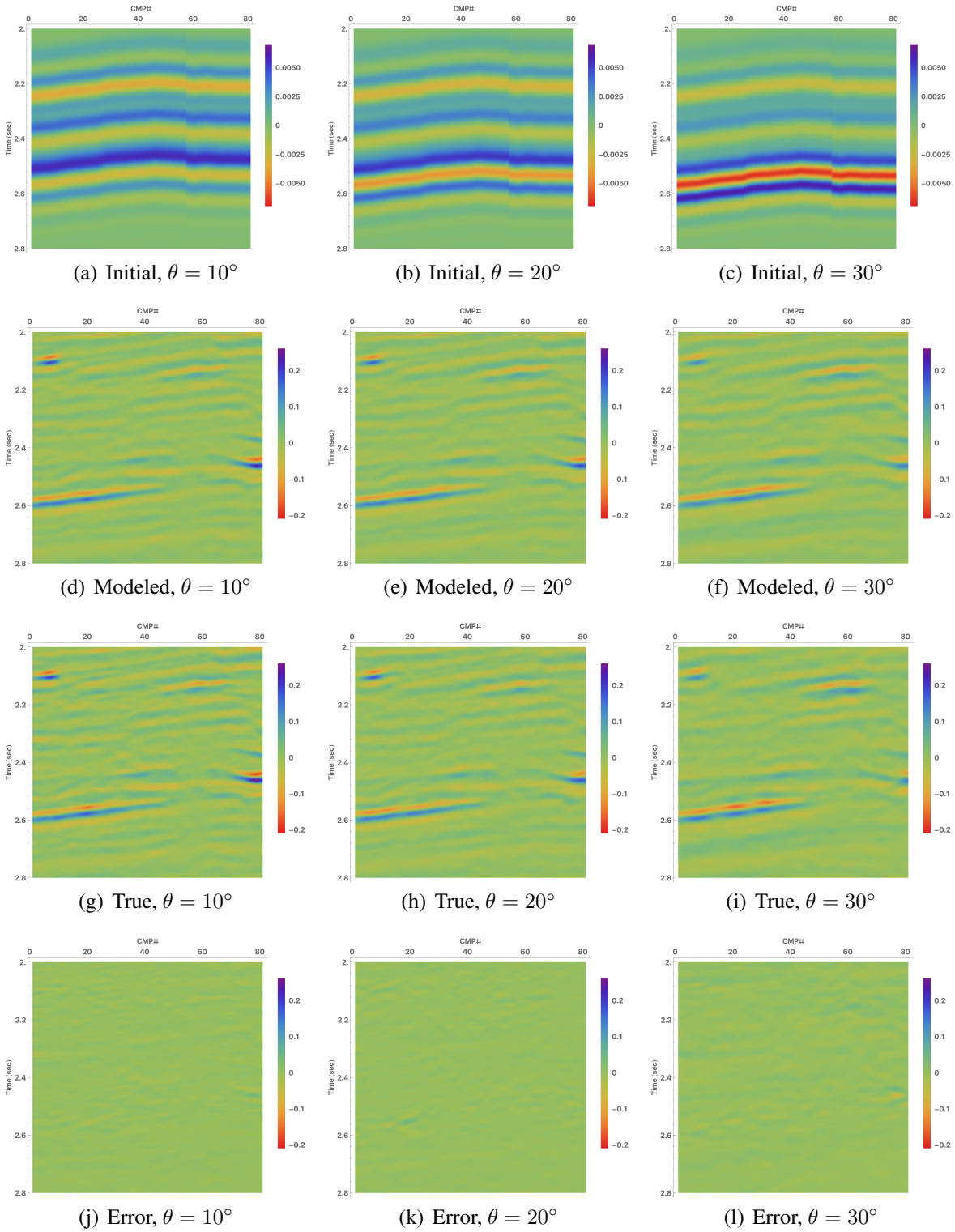

(a) Initial, $\theta = 10°$ (b) Initial, $\theta = 20°$ (c) Initial, $\theta = 30°$

(d) Modeled, $\theta = 10°$ (e) Modeled, $\theta = 20°$ (f) Modeled, $\theta = 30°$

(g) True, $\theta = 10°$ (h) True, $\theta = 20°$ (i) True, $\theta = 30°$

(j) Error, $\theta = 10°$ (k) Error, $\theta = 20°$ (l) Error, $\theta = 30°$

Figure 2.15: Seismic common-angle gathers at $\theta = 10°$, $\theta = 20°$, and $\theta = 30°$.

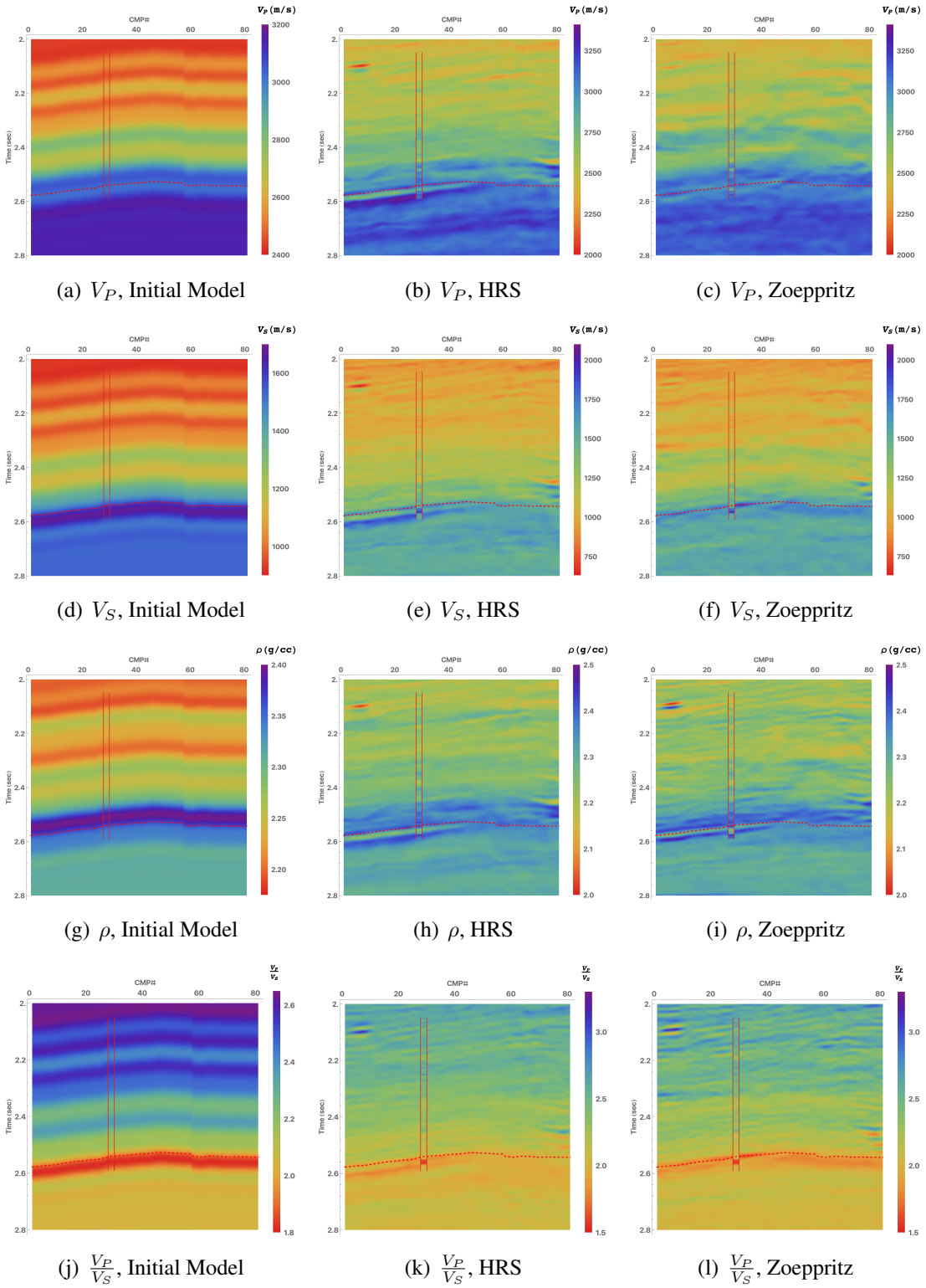

(a) V_P, Initial Model (b) V_P, HRS (c) V_P, Zoeppritz

(d) V_S, Initial Model (e) V_S, HRS (f) V_S, Zoeppritz

(g) ρ, Initial Model (h) ρ, HRS (i) ρ, Zoeppritz

(j) $\frac{V_P}{V_S}$, Initial Model (k) $\frac{V_P}{V_S}$, HRS (l) $\frac{V_P}{V_S}$, Zoeppritz

Figure 2.16: Comparison of inversion results from HRS and Zoppritz inversion.

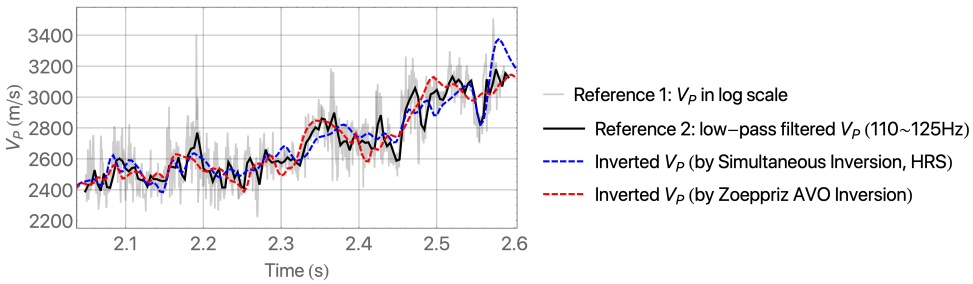

(a) V_P

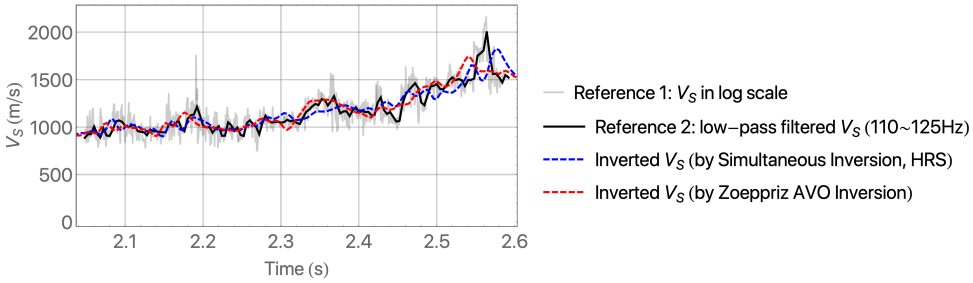

(b) V_S

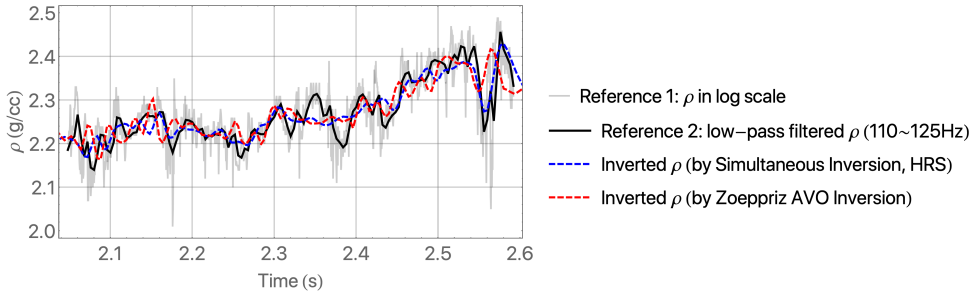

(c) ρ

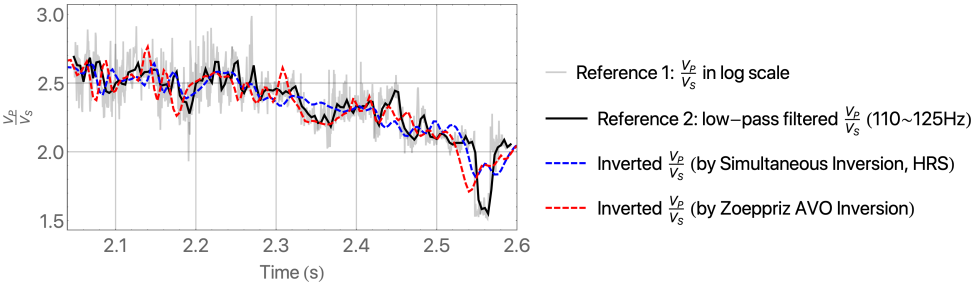

(d) $\frac{V_P}{V_S}$

Figure 2.17: QC plots. Seismic inversion results are compared to well logs and their low-pass filtered logs.

and S-wave velocities (i.e., $\frac{\bar{V_S}}{\bar{V_P}}$) is further assumed as 0.5 during the simultaneous inversion. On the other hand, such preliminary assumptions regarding parameter values are not necessary for the newly proposed Zoeppritz inversion. All other inversion input parameters (i.e., iteration number, the input range of angle of incidence, pre-whitening value, and etc.) are equal for both inversions except the linear relationships and the background ratio. The nonlinear Zoeppritz inversion results are shown in Figures 2.16(c) (for P-wave velocity), 2.16(f) (for S-wave velocity), and 2.16(i) (for density) along with Hampson-Russell's results (Figures 2.16(b), 2.16(e), and 2.16(h)). The Zoeppritz inversion and Hampson-Russell's results can validate each other since they are comparable. Both results show a decrease of density values. It is well matched to the location of the interpreted horizon, M4 Sand T, that indicates the target gas sand. These figures show that the gas reservoir is located around 2550 ms and is characterized by a relatively lower P-wave velocity and density. Right on the top of the gas sand is a surrounding shale formation which is the reservoir seal and characterized by a relatively higher P-wave and S-wave velocities, and density.

A noticeable observation in the comparison is that the general trends of the inverted results using Hampson-Russell are very similar for all three variables, P-wave and S-wave velocities, and density. It is mainly due to the fact that the simultaneous inversion still assumes linear relationships between parameters as described in equation 2.33. Although this allows the decoupling of P-wave velocity from inverted acoustic impedance by dividing inverted density values, a fixed background ratio of P-wave and S-wave velocities is being applied without any change during the whole process of the simultaneous inversion. Therefore, all three results for P-wave and S-wave velocities, and density are very similar. On the other hand, the general trends of the inversion results from the Zoeppritz inversion show more variability between the target parameters, although sudden decreases of their values are still observed at the top of the gas sand except for increased S-wave velocity. This variations are comparable to observations in logs (Figure 2.17). It is due to the fact that P-wave and S-wave velocities, and density are independently estimated from the inverted e_P, e_S, and e_D with the inversion.

Figure 2.17 shows the inversion results at the well location (CMP No. 29). Two different results

from the Zoeppritz inversion and Hampson-Russell are displayed. The accuracy of the inversions can be evaluated by overlaying them on the original logs and low-pass filtered log. Specifically, for the generation of low-pass filtered logs 110 Hz and 125 Hz are applied as low pass and high cut frequencies, respectively. It is due to the fact that the maximum frequency of the seismic data is about 125 Hz since the data is sampled in 4 ms as described before.

Although Hampson-Russell's results better match to the time locations of top and bottom of target gas-sand, it is mainly due to Hampson-Russell's additional processing steps that are further applied (e.g., well-correlation with stretch, squeeze, and time-shift, normalization of seismic and well-logs, and etc). However, the results from Zoeppritz inversion are better correlated to the well-logs, especially for density and S-wave velocity due to its higher accuracy to estimate AVO in far angle range and to determine the background ratio between P-wave and S-wave velocities. Table 2.3 provides the values of Pearson's correlation coefficient (Pearson, 1895) between the low-pass filtered logs and two inversion results for measurements of their linear correlations.

Parameters	Simultaneous Inversion (by Hampson-Russell)	Non-linear Zoeppritz
V_P	0.92	0.93
V_S	0.89	0.92
ρ	0.79	0.82
$\frac{V_P}{V_S}$	0.86	0.89

Table 2.3: Pearson's correlation coefficients between the low-pass filtered logs ($110 \sim 125$ Hz) and two inversion results described in Figure 2.17. Every value is round off to two decimal places.

2.6 Conclusions

In this section, I proposed a nonlinear AVO inversion based on exact Zoeppritz solutions for P-wave reflection amplitudes. The reformulation of the parameters in the Zoeppritz equation and application of an adjoint technique makes the nonlinear inversion possible. In contrast to traditional AVO inversions using a linearized approximation of the reflection, the inversion does not require any prerequisite assumptions such as the linear relationship between parameters, and the

background ratio between P- and S-wave velocities. Instead, the nonlinear Zoeppritz inversion can independently estimate contrasts of target parameters. It consequently leads to better estimation of P- and S-wave velocities, and density.

The given synthetic case study shows that, when a far offset AVO data is available, AVO inversion using the full Zoeppritz equation can characterize geophysical and geomechanical properties of possible target shales that are overlain by isotropic layers. Inverted P-wave and S-wave velocities are approximately equal to the horizontal velocities of the target shales, and inverted density is underestimated. Although the magnitude of the error increases with increasing velocity anisotropy, since the relationship between the magnitude and the anisotropy level of P-wave velocity is theoretically defined in the section, once the level of anisotropy can be determined by comparing inverted horizontal velocity and vertical values, accurate density estimation may also be possible. In addition, inverted geomechanical properties also have apparent systematic trends. The nonlinear approach correctly predicts the rate of change in Young's modulus and Poisson's ratio with increasing organic content.

In the given field case study, the nonlinear Zoeppritz inversion is compared to an industry standard software, Hampson-Russell AVO, using simultaneous inversion, for validation of the method. Both inversions can precisely define the target gas-sand with the decrease of parameters. The Zoeppritz inversion is implemented without any prerequisite assumptions (i.e., linear relationship between parameters, and background ratio of P-wave and S-wave velocities) that need to be applied in linear inversion in advance, Nonetheless, the nonlinear inversion provides better estimates for density and S-wave velocity than Hampson-Russell's simultaneous inversion. It is mainly due to its higher accuracy to estimate variations of reflection coefficients in far angle range and background ratio of P-wave and S-wave velocities.

Based on the above results, I conclude that the proposed nonlinear Zoeppritz inversion can consequently contribute toward both conventional and unconventional reservoir characterization by providing more accurate estimations of geophysical and geomechanical properties than compared linear methods.

3. PP- AND PS-JOINT AVO INVERSION BASED ON ZOEPPRITZ EQUATIONS*

3.1 Introduction

In the previous section, I introduced a new nonlinear AVO inversion based on exact Zoeppritz solutions for P-wave reflection amplitudes. As illustrated, the nonlinear Zoeppritz inversion promises better estimation of target parameters such as P-wave and S-wave velocities, density, and even the ratio of the velocities ($\frac{\bar{V}_P}{\bar{V}_S}$) than other linear inversions. Nonetheless, it is still challenging to separately estimate density and P-wave velocity from seismic data, when the length of source-receiver offset in pre-stack data, which will be used as input data for AVO inversion, is limited. This is due to the fact that the two parameters are strongly coupled in the variation of P-wave reflection along with the offset (i.e., AVO). Although the contrast of density mainly contributes to the AVO curve mostly at the near offset range, the contrast of P-wave velocity contributes to the AVO curve along with the whole range of the offset. Therefore, when far angle range data is available, decoupling density and P-wave velocity from inverted acoustic impedance could only be possible with conventional PP reflection survey (Dębski and Tarantola, 1995). The only exception is a situation that density contrast across an interface is larger than P-wave velocity contrast such that gas is highly saturated in a high porous sand (Kabir et al., 2005; Behura et al., 2010). Indeed, the long offset acquisition is first costly, and pre-processing to get stable reflection amplitudes in far angle ranges is secondly a big challenge due to more noisy conditions and NMO-stretch (Hilterman, 2001; Yoo and Gibson Jr, 2005; Lim, 2014).

In addition, most of the linearized AVO approach requires to know the background the ratio of averaged P-wave and S-wave velocities between two target layers, $\frac{\bar{V}_P}{\bar{V}_S}$, which is related to another physical parameter, namely the Poisson's ratio. Even though variability of the background parameter is less than other target parameters such as density, P-wave and S-wave velocities in nature at reservoir condition, a major change in the P-wave amplitude coefficient as a function of offset

*Part of this chapter is reprinted with permission from "Horizontal-velocity estimation from pp-and ps-joint avo inversion based on zoeppritz equations: Eagle ford case study" by Lim, U. Y., N. Kabir, and R. L. Gibson Jr, 2018. SEG Technical Program Expanded Abstracts 2018, 2422-2426, Copyright [2018] by Society of Exploration Geophysicists.

can be caused by a significant change in Poisson's ratio, as Ostrander (1984) showed. Therefore, if the background parameter is not correctly assumed in advance, any linearized inversions will eventually provide inaccurate estimations.

In order to overcome the challenges, many researchers applied joint inversion approaches using additional information besides PP reflection: converted PS seismic reflection (Margrave et al., 2001; Kurt, 2007; Hampson and Russell, 2013; Zhi et al., 2013; Lim et al., 2018), that can be achieved from a multicomponent survey. The addition of PS-AVO information has the potential to stabilize and improve the results of inversion even with limited AVO offset range and without the prerequisite information, background $\frac{\bar{V_P}}{\bar{V_S}}$. For example, Margrave et al. (2001) applied a linearized approximation to the PP- and PS-AVO, and their joint inversion results were superior to invert the fractional contrasts in acoustic and shear impedances when they were compared to the results using PP reflection alone. This is due to the fact that the ambiguities in the PP-AVO are reduced with in addition to PS-AVO information. Therefore, if the utilization of the nonlinear Zoeppritz AVO inversion is possible not only with P-wave reflection amplitude (as presented before) but also with additional converted PS-wave reflection, many improved results can be expected.

Besides the benefits mentioned above, the joint scheme with the nonlinear Zoeppritz inversion may contribute toward unconventional reservoir characterization by accurately estimating horizontal velocities of anisotropic source rock. It is increasingly important as oil- or gas-shale serves as a viable unconventional energy resource. Once horizontal velocities are determined, it can be continued to further source rock characterization such as inference of seismic anisotropy, geomechanical properties, and organic abundance of shale. As shown in the previous section, the nonlinear AVO inversion can concisely estimate horizontal P-wave velocity even for strong anisotropy, when full Zoeppritz solutions for PP reflection are applied using far angle data. However, the estimates of S-wave velocity is less accurate compared to the P-wave result, although it is still close to horizontal values.

In this section, I construct a new AVO inversion jointly using exact P-wave reflection and converted PS-reflection together in order to provide better solutions for the aforementioned problems. I

first show how the previous nonlinear Zoeppritz inversion using PP reflection only can be extended to simultaneously utilize PS reflection together. The Joint inversion is still based on reformulations of Zoeppritz equations (Lavaud et al., 1999). However, I newly apply the adjoint state technique (Burger and Chavent, 1979) not only for obtaining the derivatives of P-wave reflection but also for the derivatives of converted PS-reflection. Therefore, the derivation of derivatives of the converted PS-reflection will be discussed below. Then, I apply the Joint AVO inversion to a synthetic model of Eagle Ford, which is a case of strong contrast and weak anisotropy, and compare the inversion results to results from other inversions such as Fatti et al. (1994)'s linearized three-terms inversion and the nonlinear Zoeppritz inversion using P-wave reflection only. These will show that the effectiveness of the Joint AVO inversion to characterize horizontal P-wave and S-wave velocities of anisotropic shale. Lastly, I briefly discuss how this Joint inversion can contribute to the estimation of seismic anisotropy and geomechanical properties of organic-rich shale.

3.2 Methodology

From now, I describe how the non-linear Zoeppritz AVO inversion can extensively utilize converted PS reflection as well as P-wave reflection. This is mainly composed of descriptions for two methods: reformulation of P-wave and converted PS-wave reflections in Zoeppritz equations (Lavaud et al., 1999) and adjoint state technique (Burger and Chavent, 1979). The reformulation makes the computation of exact reflection coefficients for the waves possible. And the adjoint state technique is applied to differentiate the coefficient for the inversion. In this section, the derivation of derivatives of the converted PS-reflection will be focused in detail, since the derivation for P-wave reflection was already discussed in the previous section.

3.2.1 Reformulation of Zoeppritz equations: R_{PP} and R_{PS}

For the development of the PP- and PS-Joint AVO inversion based on Zoeppritz equations, I first apply the reformulations of the exact reflection coefficients for normal P-wave and converted PS-wave. The reformulations were originally proposed by Lavaud et al. (1999). They rewrote the full Zoeppritz equations in terms of following three contrast parameters and average values that

allow more effective implementation of inversion. The expressions are of the form

$$
\begin{aligned}
e_p &= (\alpha_2^2 - \alpha_1^2)/(\alpha_2^2 + \alpha_1^2) && \text{(P-wave velocity contrast)} \\
e_s &= (\beta_2^2 - \beta_1^2)/(\beta_2^2 + \beta_1^2) && \text{(S-wave velocity contrast)} \\
e_d &= (\rho_2 - \rho_1)/(\rho_2 + \rho_1) && \text{(density contrast)} \\
\chi &= 2(\bar{\beta}^2)/(\bar{\alpha}^2), && \text{(background parameter)}
\end{aligned}
\tag{3.1}
$$

where α, β, and ρ indicate P-wave velocity, S-wave velocity and density, and subscripts 1 and 2 represent the upper and lower layers, respectively. $\bar{\alpha}$ and $\bar{\beta}$ are averages of parameters of underlying and overlying layers. Then, the exact PP- and PS-reflections can be formulated as (Lavaud et al., 1999):

$$
\begin{aligned}
R_{PP} &= \frac{P - Q}{P + Q} \\
R_{PS} &= -4qM_1 \frac{T_1}{S_1}(AB + eCM_2N_2)/(P + Q)
\end{aligned}
\tag{3.2}
$$

using the intermediate variables depicted below.

$$
\begin{aligned}
e &= e_s + e_d \\
f &= 1 - e_d^2 \\
S_1 &= \chi(1 + e_p) \\
S_2 &= \chi(1 - e_p) \\
T_1 &= \frac{2}{1 - e_s} \\
T_2 &= \frac{2}{1 + e_s} \\
q^2 &= S_1 \sin^2\theta \\
M_1 &= \sqrt{S_1 - q^2} \\
M_2 &= \sqrt{S_2 - q^2} \\
N_1 &= \sqrt{T_1 - q^2} \\
N_2 &= \sqrt{T_2 - q^2} \\
D &= eq^2 \\
A &= e_d - D \\
K &= D - A \\
B &= 1 - K \\
C &= 1 + K \\
Q &= M_2(C^2 N_2 + f N_1) + 4q^2 A^2 \\
P &= M_1(B^2 N_1 + f N_2) + 4eDM_1 M_2 N_1 N_2
\end{aligned} \tag{3.3}
$$

The value of this approach is that allows expressing the exact reflection coefficients for P-wave and converted PS-wave with only the above four parameters (e_p, e_s, e_d, and χ) instead of six (α_1, α_2, β_1, β_2, ρ_1 and ρ_2). This also makes it more straightforward to perform nonlinear inversion using the exact reflection coefficient solutions although the coefficient equation is still complicated.

3.2.2 Least-squares formulation of AVO inversion jointly using R_{PP} and R_{PS}

After the reformulations, I apply a least-squares approach to AVO inversions based on the parameterization. I consider the inverse problem as the minimization of a residual error function E to characterize the least-squares error between measured and forward modeled (computed) PP- and PS-reflection coefficients as follows:

$$E(x) = \frac{1}{2}\sum_{i=1}^{N_{obs}}(w \cdot \|R^c_{i\ PP}(x) - R^m_{i\ PP}\|^2 + (1-w) \cdot \|R^c_{i\ PS}(x) - R^m_{i\ PS}\|^2) \tag{3.4}$$

where R^m_i and R^c_i are the observed and forward modeled (computed) PP- and PS-reflection coefficients at the angle of incidence, θ_i, and N_{obs} is the number of angles of incidence. w indicates a weight factor to appropriately set contributions from each reflection for the inversion. For simplicity, the value is here set as 0.5 so that PP- and converted PS reflection can equally contribute to the inversion.

To minimize the error, I apply a quasi-Newton method that requires computation of the ∇R_{PP} and ∇R_{PP} with respect to e_p, e_s, e_d, and χ. I overcome the difficulty in differentiating PP- and PS-reflection coefficients in equation 3.2 by use of the adjoint state technique (Burger and Chavent, 1979).

The theory of the technique will be described below. For further description, I call *model vector* the vector

$$x = (e_p, e_s, e_d, \chi) \in \mathbb{R}^4 \tag{3.5}$$

of all quantities that are input to the calculation of R_{PP}, and *state vector* the vector

$$y = (e, f, S_1, S_2, \ldots, P, Q, R) \in \mathbb{R}^{19} \tag{3.6}$$

that are made of all quantities in equations 3.2 and 3.3 one has to compute to solve the state equations. Here, R is the reflection coefficient that can be both for P-wave reflection (i.e., R_{PP}) and converted PS-wave reflection (i.e., R_{PS}). I also set up a *data vector*

$$z = (R^m_1, \ldots, R^m_{N_{obs}}) \in \mathbb{R}^{N_{obs}} \tag{3.7}$$

which is to be compared to the *output vector*

$$v = (R^c_1, \ldots, R^c_{N_{obs}}) \in \mathbb{R}^{N_{obs}} \tag{3.8}$$

of reflection coefficients computed by equation 3.2. Then I can write

$$v = M \begin{bmatrix} y_1 \\ . \\ . \\ . \\ y_{N_{obs}} \end{bmatrix}, \tag{3.9}$$

where y_i is given by for θ_i, $i = 1, \ldots, N_{obs}$ and M is an *observation operator*.

3.2.3 Adjoint state technique

The adjoint state technique (Burger and Chavent, 1979) is a method to efficiently compute the gradient of an object function composed of non-linearly coupled parameters. The gradient can be

computed through the resolution of a linear adjoint equation that takes the parameters in a model vector and the intermediate quantities in a state vector for the evaluation of the object function.

To illustrate the essence of the adjoint state technique, let me define the object function, the model vector, the state vector, the output vector as R, x, y, and v, respectively. In addition, a mapping φ is introduced by the following:

$$\varphi : x \rightsquigarrow v, \tag{3.10}$$

that is given by

$$\begin{aligned} x \in \mathbb{R}^n &\rightsquigarrow y \in Y \quad \text{(solution of } e_j(x, y) = 0) \\ y \in Y &\rightsquigarrow v = M(y) \in \mathbb{R}^{N_{obs}}, \end{aligned} \tag{3.11}$$

where Y, $e_j(x, y) = 0$, and $M(y)$ are an affine state-space of dimension p, a set of p state equation, and an observation operator, respectively. Then the Lagrangian of the objective function R is expressed as

$$\mathcal{L}(x, y, \omega) = R(x, v) + \sum_{j=1}^{p} e_j(x, y)\omega_j \quad \text{for any } x \in \mathbb{R}^n, y \in \mathbb{R}^p, v \in \mathbb{R}^{N_{obs}}, \omega \in \mathbb{R}^p \tag{3.12}$$

If y_x is defined as the solution for input model x, $e_j(x, y_x) = 0$ for all $j = 1, \ldots, p$ by definition. Hence, for any choice of the multiplier vector $\omega \in \mathbb{R}^p$, it obviously leads

$$R(x, v) = \mathcal{L}(x, y, \omega) \quad \text{for any } x \in \mathbb{R}^n \tag{3.13}$$

Differentiation of equation 3.13 with respect to x (for any fixed ω) gives

$$\delta R = \frac{\partial \mathcal{L}}{\partial x}\delta x + \frac{\partial \mathcal{L}}{\partial y}\delta y \tag{3.14}$$

The need for computing δy can be eliminated by taking advantage of the fact that any multiplier ω can be used: ω can be chosen in such way that the second term in right-hand side of equation 3.14, $\frac{\partial \mathcal{L}}{\partial y}\delta y$, vanishes for any $\delta y \in \mathbb{R}^p$. This is the essence of the adjoint state technique where I can choose ω such that:

$$\frac{\partial \mathcal{L}}{\partial y}(x, y, \omega)\delta y = 0 \quad \text{for any } \delta y \in \mathbb{R}^p \tag{3.15}$$

Then equation 3.14 reduces to

$$\delta R = \frac{\partial \mathcal{L}}{\partial x}\delta x \quad \text{for any } \delta x \in \mathbb{R}^n \tag{3.16}$$

Consequently, the partial derivatives of the object function with respect to the model vector (i.e., $\nabla_x R$) can only be composed of the parameters in the model vector x and the multiplier ω, which satisfies the condition in equation 3.15.

3.2.4 Derivatives R_{PS}

Once the model vector (x), the state vector (y), the data vector (z) and the output vector (v) are set as in equations 3.5, 3.6, 3.7, and 3.8, the solutions of derivatives both of R_{PP} and R_{PP} are determined from the joint use of the reformulation and the adjoint state technique. I present necessary step-by-step descriptions of how to derive the solution of derivatives of R_{PS} (i.e., ∇R_{PS}) in Appendix A.

The solution of derivatives of R_{PP} was originally discussed in Lavaud et al. (1999), but with

the wrong δS_1-term. Specifically, they omitted the sinusoidal contribution of incident angle for the δS_1-term. Therefore, I corrected the term and presented the accurate solution in the previous section. Besides it, I newly present the solution of derivatives of R_{PS} below. It was never documented before due to the complexity of R_{PS} in nature compared to R_{PP} as illustrated in equation 3.2. The derivatives of R_{PS} with respect to the model vector are

$$\begin{aligned}
\frac{\partial R_{PS}}{\partial \chi} &= -(1+e_p)\omega_3 - (1-e_p)\omega_4 \\
\frac{\partial R_{PS}}{\partial e_p} &= \chi\omega_4 - \chi\omega_3 \\
\frac{\partial R_{PS}}{\partial e_s} &= -\omega_1 - \frac{2\omega_5}{(1-e_p)^2} + \frac{2\omega_6}{(1+e_s)^2} \\
\frac{\partial R_{PS}}{\partial e_d} &= -\omega_1 + 2e_d\omega_2 - \omega_3
\end{aligned} \tag{3.17}$$

where ω_1, ω_2, ..., ω_6 are achieved by equating total derivative of variables (in equation 3.3) in following adjoint equation to zero:

$$
\begin{aligned}
&\delta R_{PS}\left[1+(P+Q)\omega_{19}\right]+\delta P(\omega_{17}+R_{PS}\omega_{19})+\delta Q(\omega_{18}+R_{PS}\omega_{19})\\
&+\delta C(\omega_{16}-2CM_2N_2\omega_{18}+4eM_1M_2N_2q\sqrt{\frac{T1}{S1}}\omega_{19})\\
&+\delta B(\omega_{15}-2BM_1N_1\omega_{17}+4AM_1q\sqrt{\frac{T1}{S1}}\omega_{19})\\
&+\delta K(\omega_{14}+\omega_{15}-\omega_{16})\\
&+\delta A(\omega_{13}+\omega_{14}-8Aq^2\omega_{18}+4BM_1q\sqrt{\frac{T1}{S1}}\omega_{19})\\
&+\delta D(\omega_{12}+\omega_{13}-\omega_{14}-4eM_1M_2N_1N_2\omega_{17})\\
&+\delta N_2\left[2N_2\omega_{11}-(fM_1+4DeM_1M_2N_1)\omega_{17}-C^2M_2\omega_{18}+4CeM_1M_2q\sqrt{\frac{T1}{S1}}\omega_{19}\right]\\
&+\delta N_1\left[2N_1\omega_{10}-(B^2M_1+4DeM_1M_2N_2)\omega_{17}-fM_2\omega_{18}\right]\\
&+\delta M_2\left[-4DeM_1N_1N_2\omega_{17}-(fN_1+C^2N_2)\omega_{18}+4CeM_1N_2q\sqrt{\frac{T1}{S1}}\omega_{19}+2M_2\omega_9\right]\\
&+\delta M_1\left[-(B^2N_1+fN_2+4DeM_2N_1N_2)\omega_{17}+4(AB+CeM_2N_2)q\sqrt{\frac{T1}{S1}}\omega_{19}+2M_1\omega_8\right]\\
&+\delta q^2\left[\omega_{10}+\omega_{11}-e\omega_{12}-4A^2\omega_{18}+\frac{2M_1(AB+CeM_2N_2)\sqrt{\frac{T1}{S1}}\omega_{19}}{q}+\omega_7+\omega_8+\omega_9\right]\\
&+\delta T_2\left[-\omega_{11}+(1+e_s)\omega_6\right]+\delta T_1\left[-\omega_{10}+\frac{2M_1(AB+CeM_2N_2)q\omega_{19}}{S_1\sqrt{\frac{T1}{S1}}}+(1-e_s)\omega_5\right]\\
&+\delta S_2(\omega_4-\omega_9)+\delta S_1\left[-\frac{2M_1(AB+CeM_2N_2)qT_1\omega_{19}}{S_1^2\sqrt{\frac{T1}{S1}}}+\omega_3-\omega_8-\omega_7\sin^2\theta\right]\\
&+\delta f(-M_1N_2\omega_{17}-M_2N_1\omega_{18}+\omega_2)\\
&+\delta e(\omega_1-q^2\omega_{12}-4DM_1M_2N_1N_2\omega_{17}+4CM_1M_2N_2q\sqrt{\frac{T1}{S1}}\omega_{19})=0
\end{aligned}
\tag{3.18}
$$

Followings are solutions of ω_1, ω_2, ..., ω_6:

$$
\begin{aligned}
\omega_1 =& \frac{4}{P+Q}\Big[-2AM_1q^3\sqrt{\frac{T_1}{S_1}} - 2Aq^4R_{PS} - BM_1q^2\left(N_1R_{PS} + q\sqrt{\frac{T_1}{S_1}}\right) + CM_1M_2N_2q\sqrt{\frac{T_1}{S_1}} \\
& + CM_2N_2q^2R_{PS} + DM_1M_2N_1N_2R_{PS} + eM_1M_2N_1N_2q^2R_{PS} + 2eM_1M_2N_2q^3\sqrt{\frac{T_1}{S_1}}\Big] \\
\omega_2 =& \frac{R_{PS}(M_1N_1 + M_2N_1)}{P+Q} \\
\omega_3 =& \frac{1}{2M_1M_2N_1N_2qS_1^2(P+Q)\sqrt{\frac{T_1}{S_1}}}\Big\{ M_2N_1N_2q\big[4ABqT_1\left(S_1 - M_1^2\right) \\
& + R_{PS}S_1^2\sqrt{\frac{T_1}{S_1}}\left(B^2N_1 + 4DeM_2N_1N_2 + fN_2\right) + 4CeM_2N_2qT_1\left(S_1 - M_1^2\right)\big] \\
& - S_1\sin^2\theta\Big[-8A^2M_1M_2N_1N_2qR_{PS}S_1\sqrt{\frac{T_1}{S_1}} \\
& + 4AM_2N_1N_2\left(BT_1\left(q^2 - M_1^2\right) + 4eM_1q^2\left(M_1T_1 + qR_{PS}S_1\sqrt{\frac{T_1}{S_1}}\right)\right) \\
& + q\Big[B^2M_2N_2R_{PS}S_1\left(M_1^2 + N_1^2\right)\sqrt{\frac{T_1}{S_1}} + 8BeM_1^2M_2N_1N_2\left(N_1R_{PS}S_1\sqrt{\frac{T_1}{S_1}} + qT_1\right) \\
& + 4DeR_{PS}S_1\sqrt{\frac{T_1}{S_1}}\left(M_1^2\left(M_2^2\left(N_1^2 + N_2^2\right) + N_1^2N_2^2\right) + M_2^2N_1^2N_2^2\right) \\
& - 8e^2M_1^2M_2^2N_1N_2^2\left(N_1R_{PS}S_1\sqrt{\frac{T_1}{S_1}} + 2qT_1\right) \\
& + fR_{PS}S_1\sqrt{\frac{T_1}{S_1}}\left(M_1^2M_2N_1 + M_1N_2\left(M_2^2 + N_1^2\right) + M_2N_1N_2^2\right)\Big] \\
& + C^2M_1N_1qR_{PS}S_1\left(M_2^2 + N_2^2\right)\sqrt{\frac{T_1}{S_1}} \\
& + 4CeN_1\left(M_1^2T_1\left(M_2^2\left(q^2 - N_2^2\right) + N_2^2q^2\right) - 2M_1M_2^2N_2^2qR_{PS}S_1\sqrt{\frac{T_1}{S_1}} + M_2^2N_2^2q^2T_1\right)\Big]\Big\} \\
\omega_4 =& \frac{C^2N_2R_{PS} + 4CeM_1N_2\sqrt{q^2}\sqrt{\frac{T_1}{S_1}} + 4DeM_1N_1N_2R_{PS} + fN_1R_{PS}}{2M_2P + 2M_2Q} \\
\omega_5 =& \frac{\sqrt{\frac{T_1}{S_1}}\big[-4ABM_1N_1q - R_{PS}S_1\sqrt{\frac{T_1}{S_1}}(B^2M_1 + 4DeM_1M_2N_2 + fM_2) - 4CeM_1M_2N_1N_2q\big]}{2(e_s-1)N_1T_1(P+Q)} \\
\omega_6 =& \frac{M_2\left(C^2R_{PS} + 4CeM_1q\sqrt{\frac{T_1}{S_1}} + 4DeM_1N_1R_{PS}\right) + fM_1R_{PS}}{2(e_s+1)N_2(P+Q)}
\end{aligned}
\tag{3.19}
$$

3.2.5 Estimation of V_P, V_S, and ρ from e_P, e_S, and e_D

Once the background parameter, χ, and three contrast parameters, e_p, e_s, and e_d, are estimated by minimizing the residual error function (equation 3.4) with $\nabla_x R_{PP}$ (i.e., combination of equations 2.25 and 2.26) and $\nabla_x R_{PS}$ (i.e., combination of equations 3.17 and 3.19), the P-wave and S-wave velocities, and density of an underlying layer can be derived from the inverted parameters with the assumption that the model parameters of an overlying layer are known as following:

$$\begin{aligned} V_{P2} &= \sqrt{\frac{1+e_p}{1-e_p}} \cdot V_{P1} \\ V_{S2} &= \sqrt{\frac{1+e_s}{1-e_s}} \cdot V_{S1} \\ \rho_2 &= \frac{1+e_d}{1-e_d} \cdot \rho_1 \end{aligned} \tag{3.20}$$

3.3 Synthetic Case Study: Eagle Ford

Model	Kerogen (v/v)	ρ (g/cm^3)	$V_P(0°)$ (km/s)	$V_P(90°)$ (km/s)	$V_S(0°)$ (km/s)	$V_{SH}(90°)$ (km/s)	ε	γ	δ
Upper Layer	0	2.72	5.55	5.55	3.08	3.08	0	0	0
Lower Layer	0	2.68	4.72	4.72	2.64	2.64	0	0	0
	0.04	2.62	4.45	4.66	2.53	2.62	0.05	0.04	0.03
	0.08	2.57	4.21	4.59	2.43	2.59	0.09	0.07	0.05

Table 3.1: Two-layer models for the testing AVO inversion using full Zoeppritz and linearized approximations. The upper and lower layers represent the overburden Austin Chalk and the target shale (Upper Eagle Ford) with various kerogen content, respectively. Adapted from Table 1 of Lim et al. (2018) with permission. Copyright 2018 by the Society of Exploration Geophysicists (SEG).

In order to show the effectiveness of the PP- and PS-joint AVO inversion based on the Zoeppritz equation, I chose a synthetic model of the Eagle Ford shale presented in Sayers et al. (2015). The main reason for the choice is that the model corresponds to strong contrast in elastic properties

and weak anisotropy in seismic P- and S-wave velocities. As explained previously, linear isotropic and anisotropic AVO inversions cannot appropriately estimate target properties under this kind of situation.

Specifically, the Eagle Ford model is composed of simple two layers with the following properties:

- A vertical transverse isotropic (VTI) shale layer is overlain by an isotropic layer.
- P- and S-wave velocities, and density, for the isotropic layer are known and values for the anisotropic layer are unknown.

Kerogen (v/v)	c_{11}	c_{13}	c_{33}	c_{44}	c_{66}	ρ
0	59.8	22.4	59.8	18.7	18.7	2.68
0.04	56.8	19.5	51.8	16.8	18.0	2.62
0.08	54.1	17.2	45.6	15.2	17.3	2.57

Table 3.2: Elastic stiffness coefficients and density modeled in Sayers et al. (2015) for the Upper Eagle Ford for a kerogen aspect ratio of 0.1 and volume fractions of 0, 0.04, and 0.08. Their units are *GPa* and g/cc for elastic stiffness coefficient and density, respectively.

With these properties, three two-layer models are generated with different values of kerogen content as shown in Table 3.1. The Austin chalk and the Upper Eagle Ford are chosen as the upper isotropic layer and the lower VTI shale layer, respectively. For the lower VTI shale layer, the chosen model varies with its kerogen content ranging from 0 to 0.08 kerogen volume fraction with an increment of 0.04. The purpose of the variation of organic abundance in the lower layer is to control the anisotropy level of given models. Specifically, organic matters are generally more soft and compliant than other minerals presented in shales. Therefore, their shapes and distribution are usually anisotropic and this consequently makes organic materials an important source of anisotropy in organic-rich shales. Model velocities are calculated from values of elastic stiffness coefficients and densities presented in Sayers et al. (2015) (Table 3.2). In order to obtain the anisotropic

elastic stiffnesses and density values, Sayers et al. (2015) applied anisotropic Hashin-Shtrikman estimates, which were originally proposed by Willis (1977, 1978) and modified by Castañeda and Willis (1995), for kerogen inclusions modeled as oblate spheroids and their aspect ratio of 0.1 in a matrix of shale. In addition, bulk and shear moduli of the inorganic phase (i.e., Quartz, Calcite, and Clay) and kerogen reported in Peselnick and Robie (1963), Tosaya (1983), Carmichael (1988), Vernik and Landis (1996), and Vanorio et al. (2003) were used for the calculation. Their proportional compositions in the matrix were determined with a ternary diagram of the mineralogy of Eagle Ford samples investigated by Harbor (2011). From the elastic stiffness coefficients and densities are determined, the following equations are used to model values of phase velocities for the VTI model at an angle of incidence, θ:

$$
\begin{aligned}
V_P(\theta) &= (c_{11}\sin^2\theta + c_{33}\cos^2\theta + c_{44} + \sqrt{M})^{\frac{1}{2}}(2\rho)^{-\frac{1}{2}} && \text{(Quasi-longitudinal phase velocity)} \\
V_{SV}(\theta) &= (c_{11}\sin^2\theta + c_{33}\cos^2\theta + c_{44} - \sqrt{M})^{\frac{1}{2}}(2\rho)^{-\frac{1}{2}} && \text{(Quasi-shear phase velocity)} \\
V_{SH}(\theta) &= \left(\frac{c_{66}\sin^2\theta + c_{44}\cos^2\theta}{\rho}\right)^{\frac{1}{2}}, && \text{(Pure-shear phase velocity)}
\end{aligned}
\tag{3.21}
$$

where

$$
M = \left[(c_{11} - c_{44})\sin^2\theta - (c_{33} - c_{44})\cos^2\theta\right]^2 + (c_{13} + c_{44})\sin^2 2\theta \tag{3.22}
$$

Here, only the phase velocities of P- and S-waves at 0° and 90° are presented in Table 3.1. I then define anisotropy levels of P-wave and S-wave velocities with Thomsen's parameters (ϵ, γ, and δ) as proposed in Thomsen (1986) as

$$
\begin{aligned}
\varepsilon &= \frac{c_{11} - c_{33}}{2c_{33}} \\
\gamma &= \frac{c_{66} - c_{44}}{2c_{44}} \\
\delta &= \frac{(c_{13} + c_{44})^2 - (c_{33} - c_{44})^2}{2c_{33}(c_{33} - c_{44})},
\end{aligned}
\tag{3.23}
$$

With the model values, exact anisotropic PP- and PS-reflection coefficients are computed by a paraxial ray tracing (Gibson et al., 1991), which effectively solve the two-point problem of finding the ray that connects exactly a specific source and receiver (Figure 3.1). It is possible due to the fact that the paraxial method can allow extrapolation of the information on a given ray to nearby receiver locations. The range of angle of incidence for the reflections is from 0° to 60°. These AVO curves provide test data for the AVO inversion.

For the estimation of properties, I compared three different AVO inversion methods: the proposed PP- and PS-Joint inversion, the nonlinear inversion using Zoeppritz solution for PP reflection only, and a linear inversion based on Fatti et al. (1994)'s three terms equation. Fatti et al. (1994)'s equation is a linearized approximation of PP reflection widely used to decouple P-wave velocity and density from acoustic impedance. Following is the formulation of Fatti et al. (1994)'s equation:

$$
\begin{aligned}
R_{PP}(\theta) &= c_1 R_P(0^\circ) + c_2 R_S(0^\circ) + c_3 R_D, \qquad (3.24)\\
\text{where} \quad c_1 &= 1 + \tan^2\theta \\
c_2 &= -8K \sin^2\theta \\
c_3 &= 2K \sin^2\theta - \frac{1}{2}\tan^2\theta \\
K &= \left[\frac{\bar{V_P}}{\bar{V_S}}\right]^2 \\
R_P(0^\circ) &= \frac{1}{2}\{\frac{\Delta V_P}{\bar{V_P}} + \frac{\Delta\rho}{\bar{\rho}}\} \\
R_S(0^\circ) &= \frac{1}{2}\{\frac{\Delta V_S}{\bar{V_S}} + \frac{\Delta\rho}{\bar{\rho}}\} \\
R_D &= \frac{\Delta\rho}{\bar{\rho}}.
\end{aligned}
$$

Once the background parameter, χ, and three contrast parameters, e_p, e_s, and e_d, are estimated with the nonlinear Zoeppritz inversion, P-wave and S-wave velocities, density, acoustic impedance (AI), and shear impedance (SI) of the underlying Upper Eagle Ford can be calculated from the inverted parameters with the assumption that the model parameters of the overlying Austin Chalk

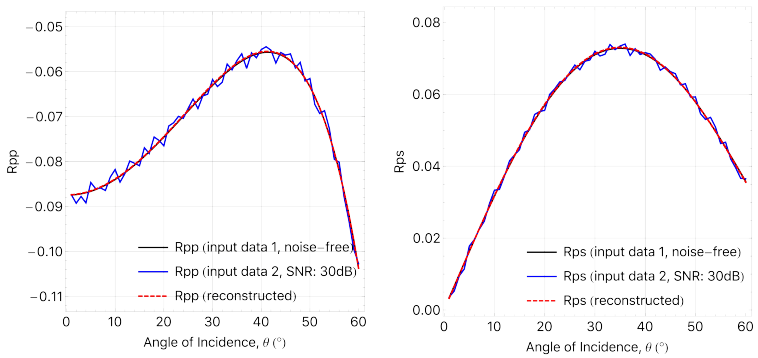

(a) Kerogen (v/v): 0

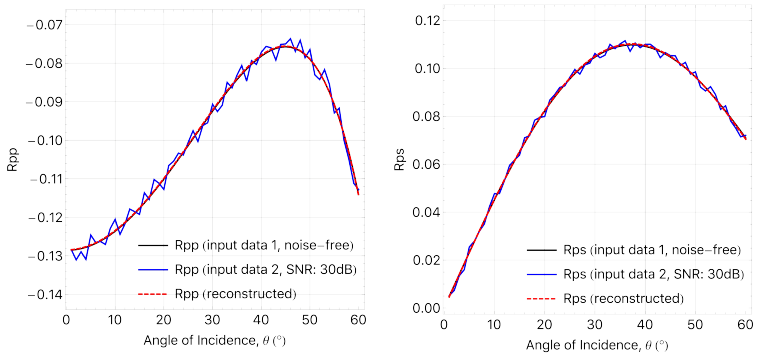

(b) Kerogen (v/v): 0.04

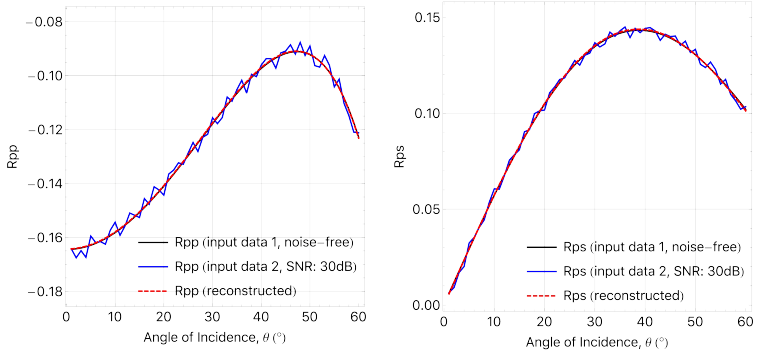

(c) Kerogen (v/v): 0.08

Figure 3.1: Input data (PP- and PS-reflection coefficients) for AVO inversion. Note that scales of the y-axis are different for each case of kerogen volume fractions. Both noise-free and noisy situations are considered. The reconstructed curves (red-dashed) are obtained with the optimal parameters when both PP- and PS-reflection coefficients are available in a noisy situation. Adapted from Figure 1 of Lim et al. (2018) with permission. Copyright 2018 by the Society of Exploration Geophysicists (SEG).

are known. As discussed in the previous section 2, when the nonlinear Zoeppritz inversion is applied to an anisotropic model with a wide range of AVO data, horizontal values are expected as inversion results for P-wave and S-wave velocities.

The inversion results of $\frac{\bar{V_P}}{\bar{V_S}}$, P-wave and S-wave velocities, and shear impedance are summarized in Figure 3.2 and Table 3.3. In both Figure 3.2 and Table 3.3, I provide the true model parameters and the corresponding shear impedance and $\frac{\bar{V_P}}{\bar{V_S}}$. The initial guesses correspond to the values of the upper layer, the Austin Chalk, except background $\frac{\bar{V_P}}{\bar{V_S}}$; target layer is the underlying Upper Eagle Ford. For the initial value of $\frac{\bar{V_P}}{\bar{V_S}}$, a value, 12% higher than the model value, is applied. Figure 3.2 shows inversion results for all the range of considered kerogen volume fraction when AVO curves (Figure 3.1) in a noise-free situation with a limited AVO angle range ($0^\circ \sim 40^\circ$) are used as data. On the other hand, Table 3.3 depicts inversion results that consider the case of 0.08 kerogen volume fraction only, which is the most anisotropic model in Table 3.1, for both noise-free and noisy situations. In this case, two different AVO angle ranges ($0^\circ \sim 40^\circ$, and $0^\circ \sim 60^\circ$) are considered.

Both Figure 3.2 and Table 3.3 show that the Fatti et al. (1994) approach cannot estimate horizontal P- and S-wave velocities, and correct shear impedance. Both PP and Joint (PP and PS) AVO inversion using exact Zopperitz equations can accurately determine horizontal P-wave velocity. However, when only PP reflection is available, the nonlinear inversion cannot determine correct horizontal S-wave velocity. On the other hand, horizontal S-wave velocity is accurately estimated when the Joint AVO inversion is applied. Additionally, the Joint inversion provides better estimations of shear impedance (SI) than other inversions. With the Joint inversion, all target parameters are recovered with less than 2% error even for the noisy situation with the limited AVO input range (i.e., $0^\circ \sim 40^\circ$). The reason of this improvement is due to better estimation of background $\frac{\bar{V_P}}{\bar{V_S}}$ with the addition of PS AVO information as depicted in Figure 3.2(a).

In addition, Figures 3.3 and 3.4 visualize the percent error between model and inverted values of target parameters for most anisotropic case (i.e., 0.08 of kerogen volume fraction) among the models presented in Table 3.3 . Figures 3.3 and 3.4 correspond to noise free and noise added

(30dB of signal-to-noise ratio) cases, respectively. They highlight the superiority of the proposed Joint inversion than compared methods. Both figures clearly show that the errors of estimation for all target parameters are smallest when PP- and PS-reflection coefficient are used as input data together with the joint inversion. Above all, the joint inversion provides a similar level of accuracy for the estimation even with the limited input range of AVO (i.e., $0^\circ \sim 40^\circ$) compared to the error level with a relatively wide angle range (i.e., $0^\circ \sim 60^\circ$). Moreover, the proposed method is the least sensitive result to signal-to-ratio among the presented inversions.

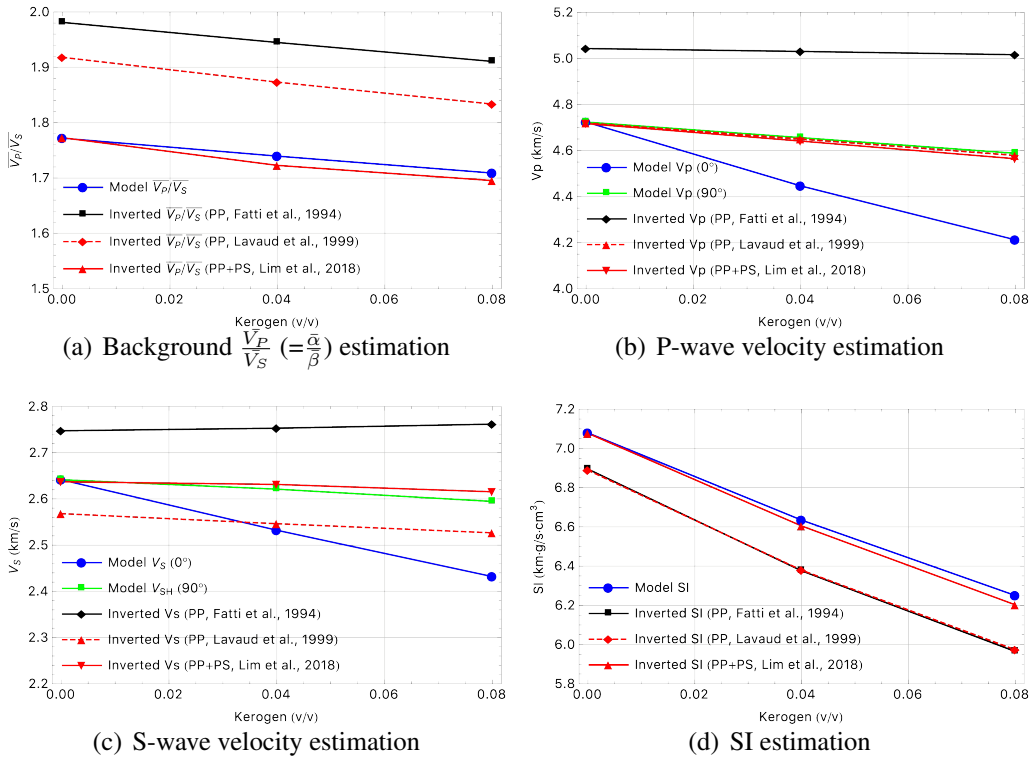

(a) Background $\frac{\bar{V}_P}{\bar{V}_S}$ ($=\frac{\bar{\alpha}}{\bar{\beta}}$) estimation

(b) P-wave velocity estimation

(c) S-wave velocity estimation

(d) SI estimation

Figure 3.2: Estimated $\frac{\bar{V}_P}{\bar{V}_S}$, P-wave and S-wave velocities, and shear impedance from three different AVO inversions. $0^\circ \sim 40^\circ$ AVO angle range is applied as data for the inversions in a noise-free situation. Adapted from Figure 2 of Lim et al. (2018) with permission. Copyright 2018 by the Society of Exploration Geophysicists (SEG).

Noise level	Noise-free					SNR: 30dB				
Parameter	$\frac{V_P}{V_S}$ (=$\frac{\bar{\alpha}}{\bar{\beta}}$)	$V_P(90°)$	$V_{SH}(90°)$	AI	SI	$\frac{V_P}{V_S}$ (=$\frac{\bar{\alpha}}{\bar{\beta}}$)	$V_P(90°)$	$V_{SH}(90°)$	AI	SI
True	1.71	4.59	2.59	10.83	6.25	1.71	4.59	2.59	10.83	6.25
Initial	1.91	5.55	3.08	15.09	8.38	1.91	5.55	3.08	15.09	8.38
AVO data range: $0° \sim 40°$										
PP (Fatti et al., 1994)	1.91	5.02	2.76	10.83	5.96	1.91	4.83	2.64	10.83	5.91
error	12%	9%	6%	0%	5%	12%	5%	3%	0%	5%
PP (Lavaud et al., 1999)	1.83	4.58	2.53	10.83	5.97	1.83	4.48	2.47	10.83	5.96
error	7%	0%	3%	0%	4%	7%	2%	5%	0%	5%
PP+PS (Lim et al., 2018)	1.70	4.56	2.62	10.82	6.20	1.70	4.50	2.57	10.83	6.19
error	1%	1%	1%	0%	1%	0%	2%	1%	0%	1%
AVO data range: $0° \sim 60°$										
PP (Fatti et al., 1994)	1.91	5.10	2.83	10.85	6.02	1.91	5.11	2.83	10.86	6.03
error	12%	11%	9%	0%	4%	12%	11%	9%	0%	4%
PP (Lavaud et al., 1999)	1.83	4.59	2.53	10.83	5.97	1.81	4.56	2.53	10.83	6.01
error	7%	0%	2%	0%	4%	6%	1%	2%	0%	4%
PP+PS (Lim et al., 2018)	1.70	4.59	2.63	10.83	6.20	1.70	4.57	2.61	10.83	6.19
error	1%	0%	1%	0%	1%	0 %	0%	1%	0%	1%

Table 3.3: Inversion results with three different AVO methods in the noise-free situation (left) and when the signal to noise ratio is 30 dB (Right). The applied model is the case of 0.08 kerogen volume fraction. Velocities and impedances are in km/s and $km \cdot g/s \cdot cm^3$, respectively. Every inversion results and percent errors are round off to two decimal places and the nearest whole number, respectively. Adapted from Table 3 of Lim et al. (2018) with permission. Copyright 2018 by the Society of Exploration Geophysicists (SEG).

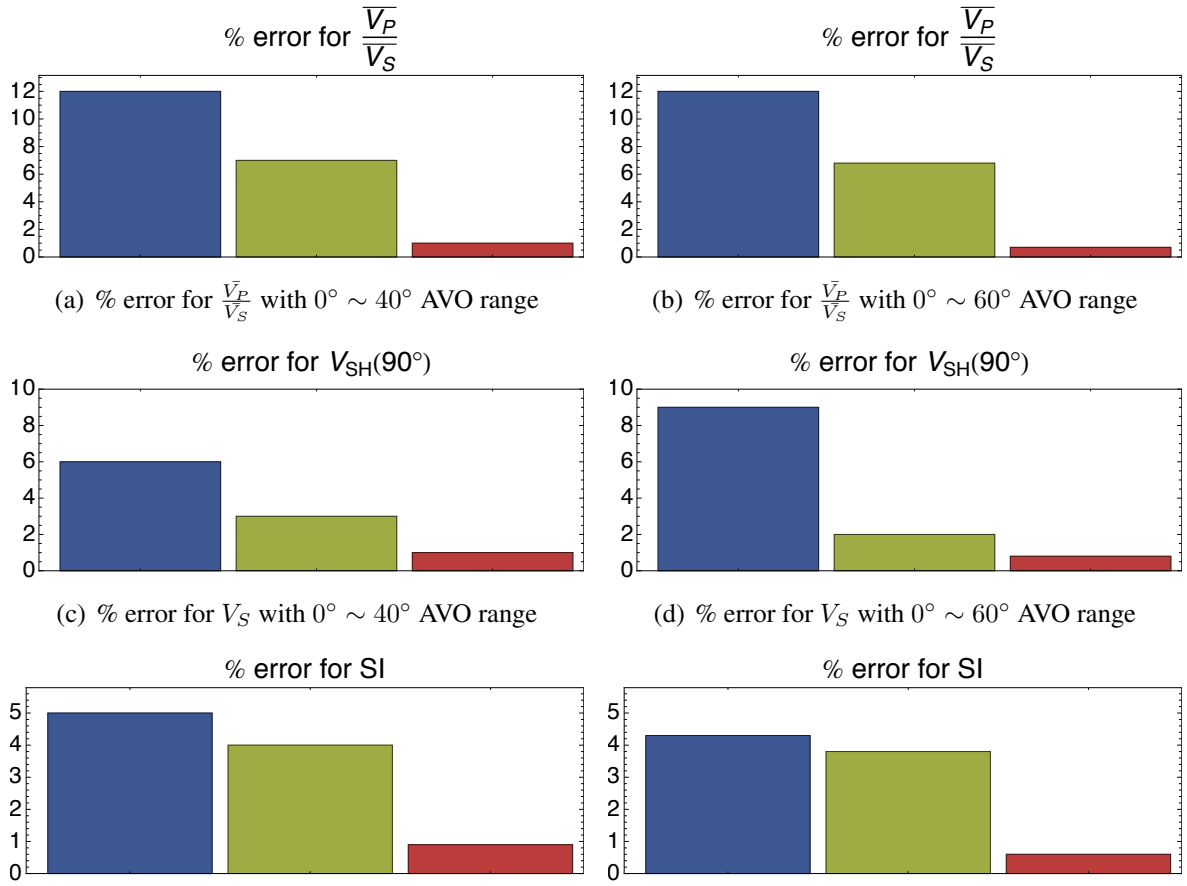

(a) % error for $\frac{\bar{V}_P}{\bar{V}_S}$ with $0° \sim 40°$ AVO range

(b) % error for $\frac{\bar{V}_P}{\bar{V}_S}$ with $0° \sim 60°$ AVO range

(c) % error for V_S with $0° \sim 40°$ AVO range

(d) % error for V_S with $0° \sim 60°$ AVO range

(e) % error for SI with $0° \sim 40°$ AVO range

(f) % error for SI with $0° \sim 60°$ AVO range

Figure 3.3: Percent error between model and inverted values of target parameters (for Kerogen (v/v): 0.08, Anisotropic, noise free). An intermediate angle range ($0° \sim 40°$) and a far angle range ($0° \sim 60°$) are applied as data for inversion. Blue, green, and red bars correspond to the inversion methods using Fatti's three-terms linear inversion, the Zoeppritz inversion using P-wave reflection only, and the proposed joint Zoeppritz inversion, respectively.

3.4 Conclusions and Discussion

In this section, I developed a new AVO inversion jointly using exact P-wave reflection and converted PS-reflection together. Especially, I newly derived the derivatives of the PS-wave reflection coefficient in terms of model parameters by applying a combination of the reformulation of parameters in the Zoeppritz equation and the adjoint state technique. This made the nonlinear inversion possible and stable.

In the given synthetic model test, the PP- and PS-Joint AVO inversion based on exact Zoeppritz

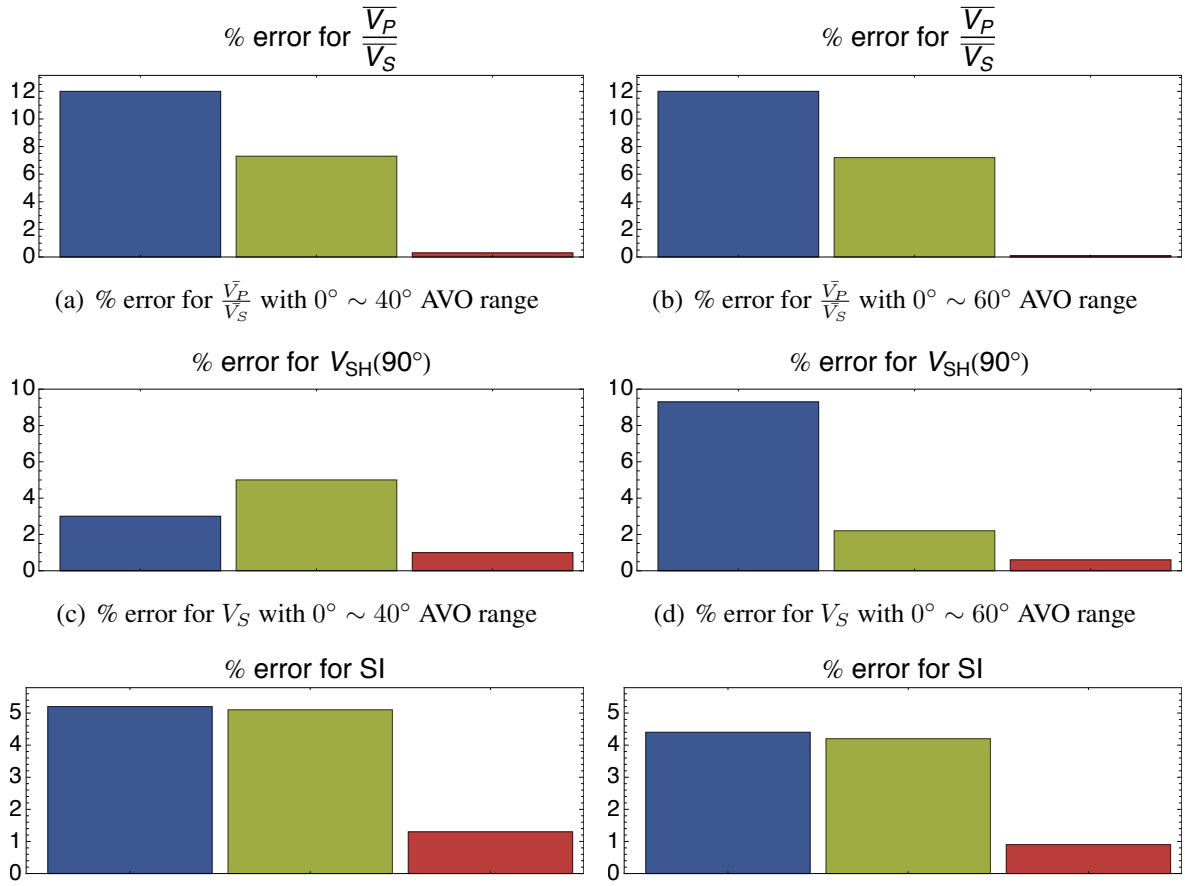

(a) % error for $\frac{\bar{V}_P}{\bar{V}_S}$ with $0° \sim 40°$ AVO range

(b) % error for $\frac{\bar{V}_P}{\bar{V}_S}$ with $0° \sim 60°$ AVO range

(c) % error for V_S with $0° \sim 40°$ AVO range

(d) % error for V_S with $0° \sim 60°$ AVO range

(e) % error for SI with $0° \sim 40°$ AVO range

(f) % error for SI with $0° \sim 60°$ AVO range

Figure 3.4: Percent error between model and inverted values of target parameters (for Kerogen (v/v): 0.08, Anisotropic, SNR: 30dB). An intermediate angle range ($0° \sim 40°$) and a far angle range ($0° \sim 60°$) are applied as data for inversion. Blue, green, and red bars correspond to the inversion methods using Fatti's three-terms linear inversion, the Zoeppritz inversion using P-wave reflection only, and the proposed joint Zoeppritz inversion, respectively.

equations can successfully estimate horizontal P-wave and S-wave velocities of Upper Eagle Ford overlain by Austin Chalk, for all range of model kerogen content. The inversion also accurately determines shear impedance and background $\frac{\bar{V}_P}{\bar{V}_S}$. Above all, all target parameters can correctly be recovered by the Joint inversion not only with a wide AVO input range but also with a relatively narrow AVO input range. In addition, the proposed nonlinear inversion is less sensitive to the signal-to-noise ratio that other inversion methods presented for comparison.

Based on the above results, I conclude that the proposed nonlinear PP- and PS-Joint Zoeppritz

inversion can consequently contribute to better characterization of conventional reservoir compared to that can achieved by other methods using P-wave reflection only. It is due to such benefits that the proposed method can provide:

- More accurate estimates of elastic properties.
- Correct estimation of the ratio between P-wave and S-wave velocities, which is normally constantly fixed in other inversions using P-wave reflection only, therefore has to be assumed correctly before inversion.
- Less sensitive to input AVO range and signal-to-noise ratio of the data.

Besides the above benefits, the method can also contribute to unconventional reservoir characterization by estimation of seismic anisotropy and geomechanical properties (e.g., Young's modulus and Poisson's ratio) of target shale. Since the PP- and PS-Joint inversion can successfully estimate horizontal P-wave and S-wave velocities of anisotropic shale, if the estimation of vertical velocity values somehow can be possible with other seismic methods, seismic anisotropy of target shale can be determined. Consequently, it leads to a better estimation of geomechanical properties not only in one direction but also in both horizontal and vertical directions. In the next section, I will introduce how the vertical values can also be achieved from seismic data and will propose a workflow to determine seismic anisotropy and geomechanical properties of anisotropic media.

4. APPLICATIONS OF NONLINEAR ZOEPPRITZ AVO INVERSION IN ESTIMATING SEISMIC ANISOTROPY, GEOMECHANICAL PROPERTIES, AND TOC

4.1 Introduction

Elastic properties, that can be estimated from AVO inversion, can also be linked to further estimation of additional physical constraints of target subsurface layer such as porosity, types of saturated fluid and lithology (Shuey, 1985; Gardner and Forel, 1987; Smith and Gidlow, 1987; Rutherford and Williams, 1989; Verm and Hilterman, 1995; Goodway et al., 1997). However, most of the rock property estimations only targeted typical high porous rocks: mainly sandstone and often carbonates, before unconventional shale has emerged as a viable energy resource. Nonetheless, accurate characterization of source rock properties became increasingly important in the last decade, since shale is now not only treated as source rock but also as a self-contained reservoir in an unconventional petroleum system. Consequently, the estimation of properties of shales from seismic data is important for the development of unconventional reservoirs. In particular, seismic anisotropy, geomechanical properties, and total organic carbon (TOC) content are key parameters that have a direct impact on the drilling and development of unconventional reservoirs.

Regarding geomechanical properties, if AVO inversion can successfully estimate parameters such as P-wave and S-wave velocities, and density for target shale formations, their geomechanical properties (i.e., Young's modulus and Poisson's ratio) can also be determined (Chopra et al., 2013). Zong et al. (2013) and Payne and Meyer (2017) showed examples of how AVO inversion can infer a representative value of geomechanical properties with an assumption of seismic isotropy. Once elastic Young's modulus and Poisson's ratio are successfully determined, brittleness and fracability of target shale can further be assessed, and this information can be used for defining landing zones of horizontal wells and for the effective hydraulic fracturing. Rickman et al. (2008) originally proposed an index to evaluate rock brittleness based on petrophysical observations, which indicate a correlation between higher brittleness and higher Young's modulus (and lower Poisson's ratio).

Goodway et al. (2010), Guo et al. (2012), and Zorn et al. (2017) also followed Rickman et al. (2008)'s approach and introduced other seismic attributes to infer rock brittleness from elastic properties. However, the general approach in the above methods is still based on the assumption of seismic isotropy. Organic-rich shale formations are, however, often anisotropic (Vernik and Nur, 1992; Johnston and Christensen, 1995; Sondergeld et al., 2000); this means that not only seismic wave velocities but also geomechanical properties have the anisotropic characteristic. Sayers et al. (2015) also showed that the level of anisotropy increases when the volume fraction of total organic carbon content (TOC) in shale increases.

Estimation of TOC in shale is also important since hydrocarbon sweet spots can generally be characterized by high TOC in unconventional plays. Solid organic matter in shale is generally referred to as kerogen and its fractional content is measured from core samples with a Rock-Eval pyrolysis device and typically reported as TOC (Jarvie et al., 2007; Huc, 2013). Although there are many different versions of the Rock-Eval pyrolysis differently developed by Durand and Espitalie (1976), Espitalié et al. (1977), Price (1983), and Durand et al. (1987), the device generally includes combustion and pyrolysis ovens together with hydrocarbon and CO_2 detectors. The output from the Rock-Eval can be used for extracting such data from core samples: TOC, the petroleum potential of the rock, the type of kerogen, and its thermal maturity. However, this direct measurement is only possible with expensive coring and laboratory treatments and thus quite costly. Whereas, petrophysical correlation methods based on wireline logs such as Schmoker (1979) and Passey et al. (1990) have been widely used for indirect TOC measurement. Once the indirect estimation is calibrated by direct TOC measurements in reference wells, geostatistical interpolation methods can further be applied to estimate its lateral variation. In addition, changes in TOC in shale can be detected from the surface seismic response, since the organic portion of shale influences its elastic properties such as P-wave and S-wave velocities, and density (Chopra et al., 2013). When a sound relationship between TOC and elastic properties of shale is built, TOC can be inferred from estimated elastic properties by seismic inversion. Løseth et al. (2011) and Altowairqi et al. (2017) estimate TOC from inverted acoustic impedance, which is the product

of P-wave velocity and density. However, if density and P-wave velocity can be decoupled from acoustic impedance, it may be possible to more reliably infer TOC from density. This is due to the fact that density is more directly governed by the organic portion of shale than any other elastic properties that can be estimated from seismic inversion (Schmoker, 1979; Vernik, 2016). In addition, determination of the level of anisotropy can also be linked to TOC estimation, since higher TOC is related to higher anisotropy.

As described above, it is the key for successful unconventional reservoir characterization to accurately estimate seismic anisotropy. However, many seismic applications based on elasticity theory were developed under the assumption of isotropy, although most sedimentary rocks are observed to be anisotropic from many experiments (Thomsen, 2014). In particular, most conventional AVO equations (Aki and Richards, 1980; Shuey, 1985; Wiggins et al., 1983; Fatti et al., 1994) are linear approximations of Zoeppritz equations (Zoeppritz, 1919) assuming weak contrasts in properties and seismic isotropy in velocities. However, it is known that if a seismic wave with a wavelength longer than target layers thickness propagates through a layered sequence of isotropic or VTI media, the wave behaves as if it propagates in a homogeneous but anisotropic medium, as Backus (1962) proved. Therefore, there is a fundamental discrepancy between reality and seismic applications. Thomsen (1986) accounted for the effects of seismic anisotropy in the seismic method. He first defined the level of anisotropy with three parameters (i.e., ϵ, γ, and δ) which are named after the *Thomsen parameters*. Bork et al. (1997) and Hilterman (2001) provided examples with anisotropic forward modeling in order to show significant differences between the AVO responses with and without anisotropy. For example, Bork et al. (1997) related VTI anisotropy to the unusual AVO anomalies they observed in the Gulf of Mexico and Trinidad. More importantly, they also emphasized that a new seismic inversion tool that can handle anisotropy should be developed. Although Rüger (1997) proposed an AVO equation for P-wave reflection coefficients in a TI media, it can only provide an accurate estimation based on the assumptions of weak contrast and weak anisotropy, that is, about a $10 \sim 20\%$ difference in seismic velocities as defined in Thomsen (1986). As a result, AVO inversion based on the above equations does not produce correct re-

sults when target shale has strong contrasts and strong anisotropy (Lavaud et al., 1999; Lim et al., 2017). Therefore, much research is still necessary to appropriately understand seismic anisotropy and make it a viable exploration tool.

In the previous section 1, I showed that the proposed nonlinear Zoeppritz inversion can accurately estimate horizontal P-wave velocity even for strong anisotropy when full Zoeppritz solutions for PP reflection are applied using far angle data. Density is, however, underestimated depending on the degree of anisotropy of P-wave velocity. I theoretically derived why horizontal velocity and underestimated density are determined by the AVO inversion and defined the relationship between the underestimation and the anisotropy. Therefore, the underestimated density can be corrected if the degree of anisotropy of P-wave velocity is accurately defined. This allows us to use Zoeppritz PP-AVO inversion to estimate organic carbon content in shale from the seismic response. In addition, it also gives an indication of how to estimate geomechanical properties in both horizontal and vertical directions, noting that previous approaches by other researchers (Zong et al., 2013; Payne and Meyer, 2017) could estimate only one value of geomechanical properties.

In this section, I first summarize the nonlinear AVO inversion using the full Zoeppritz equations and explain how better results can be achieved by the inversion instead of linearized approximations. I then describe how the proposed method can be applied for the estimation of seismic anisotropy, geomechanical properties, and TOC of shale. Particularly, I examine and explain the systematic trends of the inversion results with a simple two-layer synthetic model. The model is generated from the dataset of Avalon shale, Delaware Basin. I conducted the proposed AVO inversion with both near and far angle ranges since the results provide critical constraints to build a workflow that will be proposed below. In addition, I build an empirical rock physics relationship between organic carbon contents and invertible seismic properties for the target formation, Avalon shale, from cross-plots. It is observed a strong correlation between density and organic carbon content. From the relationship, I model geophysical parameters (i.e., P-wave and S-wave velocities, and density) with respect to the degree of anisotropy of the target shale and generate reflection coefficients based on the model values. The degree of anisotropy is controlled by the

amount of kerogen. I then present inversion results that show the effectiveness of the AVO inversion to characterize horizontal and vertical velocities, density of anisotropic shale. Based on the results, I propose a workflow and describe how it can be used for the estimation of seismic anisotropy, geomechanical properties, and TOC of highly anisotropic organic-rich shale. Besides the workflow, I introduce a new seismic attribute I label ΔV_P. It is developed to more practically estimate seismic anisotropy from real seismic data. For the development, a sensitivity test with various source-receiver offsets (i.e., angles of incidence) is first conducted with the simple two-layer synthetic model. Subsequently, the effectiveness of the attribute is demonstrated with the GOM field data, that was previously presented in section 1 also, and verified with a gamma-ray log of a vertical well located in the field.

4.2 Methodology

4.2.1 Nonlinear Zoeppritz AVO inversion

In order to develop a workflow to estimate seismic anisotropy, geomechanical properties, and TOC of shale, I apply a nonlinear AVO inversion based on the exact reflection coefficients. As presented in section 2 in detail, the nonlinear inversion was originally proposed with Lavaud et al. (1999)'s reformulation. They rewrote the full Zoeppritz equations in terms of the following three contrast parameters and an average background parameter that allow more effective implementation of inversion. The expressions are of the form

$$\begin{aligned} e_p &= (\alpha_2^2 - \alpha_1^2)/(\alpha_2^2 + \alpha_1^2) && \text{(P-wave velocity contrast)} \\ e_s &= (\beta_2^2 - \beta_1^2)/(\beta_2^2 + \beta_1^2) && \text{(S-wave velocity contrast)} \\ e_d &= (\rho_2 - \rho_1)/(\rho_2 + \rho_1) && \text{(density contrast)} \\ \chi &= 2(\bar{\beta}^2)/(\bar{\alpha}^2), && \text{(background parameter)} \end{aligned} \tag{4.1}$$

where α, β, and ρ indicate P-wave velocity, S-wave velocity and density, and subscripts 1 and 2 represent the upper and lower layers, respectively. $\bar{\alpha}$ and $\bar{\beta}$ are averages of parameters of un-

derlying and overlying layers. Then, the exact PP-reflection can be formulated as (Lavaud et al., 1999):

$$R_{PP} = \frac{P - Q}{P + Q}, \tag{4.2}$$

using the intermediate variables depicted below.

$$
\begin{aligned}
e &= e_s + e_d \\
f &= 1 - e_d^2 \\
S_1 &= \chi(1 + e_p) \\
S_2 &= \chi(1 - e_p) \\
T_1 &= \frac{2}{1 - e_s} \\
T_2 &= \frac{2}{1 + e_s} \\
q^2 &= S_1 \sin^2\theta \\
D &= eq^2 \\
M_1 &= \sqrt{S_1 - q^2} \\
M_2 &= \sqrt{S_2 - q^2} \\
N_1 &= \sqrt{T_1 - q^2} \\
N_2 &= \sqrt{T_2 - q^2} \\
A &= e_d - D \\
K &= D - A \\
B &= 1 - K \\
C &= 1 + K \\
Q &= M_2(C^2 N_2 + f N_1) + 4q^2 A^2 \\
P &= M_1(B^2 N_1 + f N_2) + 4eDM_1 M_2 N_1 N_2
\end{aligned}
\tag{4.3}
$$

The value of this approach is that allows expressing the exact PP-reflection coefficients with only the above four parameters (e_p, e_s, e_d, and χ) instead of six (α_1, α_2, β_1, β_2, ρ_1 and ρ_2). This also makes it more straightforward to perform nonlinear inversion using the exact reflection coefficient solutions although the coefficient equation is still complicated.

After the reformulation, I apply a least-squares approach to AVO inversions based on this new parameterization. I consider the inverse problem as the minimization of a residual error function E to characterize the least-squares error between measured and forward modeled (computed) PP-reflection coefficients as follows:

$$E(x) = \frac{1}{2}\sum_{i=1}^{N_{obs}} \|R^c_{i\ PP}(x) - R^m_{i\ PP}\|^2, \tag{4.4}$$

where $R^m_{i\ PP}$ and $R^c_{i\ PP}$ are the measured and forward modeled (computed) PP-reflection coefficients at the angle of incidence, θ_i, and N_{obs} is the number of angles of incidence.

To minimize the error, I apply a quasi-Newton method that requires computation of the ∇R_{PP} with respect to e_p, e_s, e_d, and χ. I overcome the difficulty in differentiating PP-reflection coefficients in equation 4.2 by use of the adjoint state technique (Burger and Chavent, 1979). Details of the adjoint state technique are well described in sections 2 and 3. Followings are the solution of ∇R_{PP} with respect to e_p, e_s, e_d, and χ:

$$\begin{aligned}
\frac{\partial R_{PP}}{\partial \chi} &= -(1+e_p)\omega_3 - (1-e_p)\omega_4 \\
\frac{\partial R_{PP}}{\partial e_p} &= \chi\omega_4 - \chi\omega_3 \\
\frac{\partial R_{PP}}{\partial e_s} &= -\omega_1 - \frac{2\omega_5}{(1-e_p)^2} + \frac{2\omega_6}{(1+e_s)^2} \\
\frac{\partial R_{PP}}{\partial e_d} &= -\omega_1 + 2e_d\omega_2 - \omega_3,
\end{aligned} \tag{4.5}$$

where ω_1, ω_2, ..., ω_6 are

$$
\begin{aligned}
\omega_1 =& \frac{q^2}{P+Q}\big[8Aq^2(-R_{PP}-1)+4BM_1N_1(1-R_{PP}) \\
& -4CM_2N_2(-R_{PP}-1)-4eM_1M_2N_1N_2(1-R_{PP})\big] \\
& -\frac{4DM_1M_2N_1N_2(1-R_{PP})}{P+Q} \\
\omega_2 =& \frac{M_2N_1(R_{PP}+1)-M_1N_2(1-R_{PP})}{P+Q} \\
\omega_3 =& \frac{\sin^2\theta}{2(P+Q)}\Big\{8A^2(R_{PP}+1)+8e(-2Aq^2R_{PP}-2Aq^2-BM_1N_1(R_{PP}-1) \\
& +CM_2N_2(R_{PP}+1)+eM_1M_2N_1N_2R_{PP}-eM_1M_2N_1N_2) \\
& -\frac{(R_{PP}-1)\big[B^2N_1+N_2(4DeM_2N_1+f)\big]}{M_1} \\
& +\frac{B^2(M_1-M_1R_{PP})-M_2(4DeM_1N_2(R_{PP}-1)+f(R_{PP}+1))}{N_1} \\
& +\frac{f(M_1-M_1R_{PP})-M_2\big[C^2(R_{PP}+1)+4DeM_1N_1(R_{PP}-1)\big]}{N_2} \\
& -\frac{N_2\big[C^2(R_{PP}+1)+4DeM_1N_1(R_{PP}-1)\big]+fN_1(R_{PP}+1)}{M_2}\Big\} \\
& +\frac{(R_{PP}-1)\big[B^2N_1+N_2(4DeM_2N_1+f)\big]}{2(P+Q)M_1} \\
\omega_4 =& \frac{N_2\big[C^2(R_{PP}+1)+4DeM_1N_1(R_{PP}-1)\big]+fN_1(R_{PP}+1)}{2M_2(P+Q)} \\
\omega_5 =& \frac{B^2(M_1-M_1R_{PP})-M_2\big[4DeM_1N_2(R_{PP}-1)+f(R_{PP}+1)\big]}{2(e_s-1)N_1(P+Q)} \\
\omega_6 =& \frac{M_2\big[C^2(R_{PP}+1)+4DeM_1N_1(R_{PP}-1)\big]+fM_1(R_{PP}-1)}{2(e_s+1)N_2(P+Q)}
\end{aligned}
\tag{4.6}
$$

Once the background parameter, χ, and three contrast parameters, e_p, e_s, and e_d, are estimated by minimizing the residual error function (equation 4.4) with $\nabla_x R_{PP}$ (combination of equations 4.5 and 4.6), the P-wave and S-wave velocities, and density of an underlying layer can be derived from the inverted parameters with the assumption that the model parameters of an overlying layer are known as following:

$$
\begin{aligned}
V_{P2} &= \sqrt{\frac{1+e_p}{1-e_p}} \cdot V_{P1} \\
V_{S2} &= \sqrt{\frac{1+e_s}{1-e_s}} \cdot V_{S1} \\
\rho_2 &= \frac{1+e_d}{1-e_d} \cdot \rho_1
\end{aligned}
\tag{4.7}
$$

4.2.2 Analysis of inversion results based on a synthetic case study (based on a seismic model from Avalon Shale, Delaware Basin)

From now, the proposed nonlinear inversion is tested with a simple two-layer synthetic model. The model is generated from a dataset of Avalon Shale, Delaware Basin. The main objective of this test is to build an effective workflow to estimate seismic anisotropy, geomechanical properties, and TOC of shale by analyzing inversion results with two different AVO input ranges (i.e., relatively near and far angle ranges). As illustrated below, the results will provide critical constraints to build the workflow.

4.2.2.1 Data & Model generation

Data, used for a synthetic model generation, are from a vertical well in the Bone Spring formation and Avalon shale of the Delaware basin. Figure 4.1 shows a plot of horizontal and vertical P-wave and S-wave velocities, density, and TOC for the interval considered in the model generation. The interbedded limestones with higher velocity (compared to shale) are clearly visible. Horizontal and vertical velocities are from ultrasonic measurements and open-hole logging respectively. Density and TOC values are achieved from tight rock analysis and Rock-Eval pyrolysis.

In order to investigate what quantities are determined using the full Zoeppritz solutions for P-wave reflection amplitudes that assume isotropy when the target formation is instead anisotropic, I consider a model with the following properties:

- A vertical transverse isotropic (VTI) shale layer is overlain by an isotropic layer.

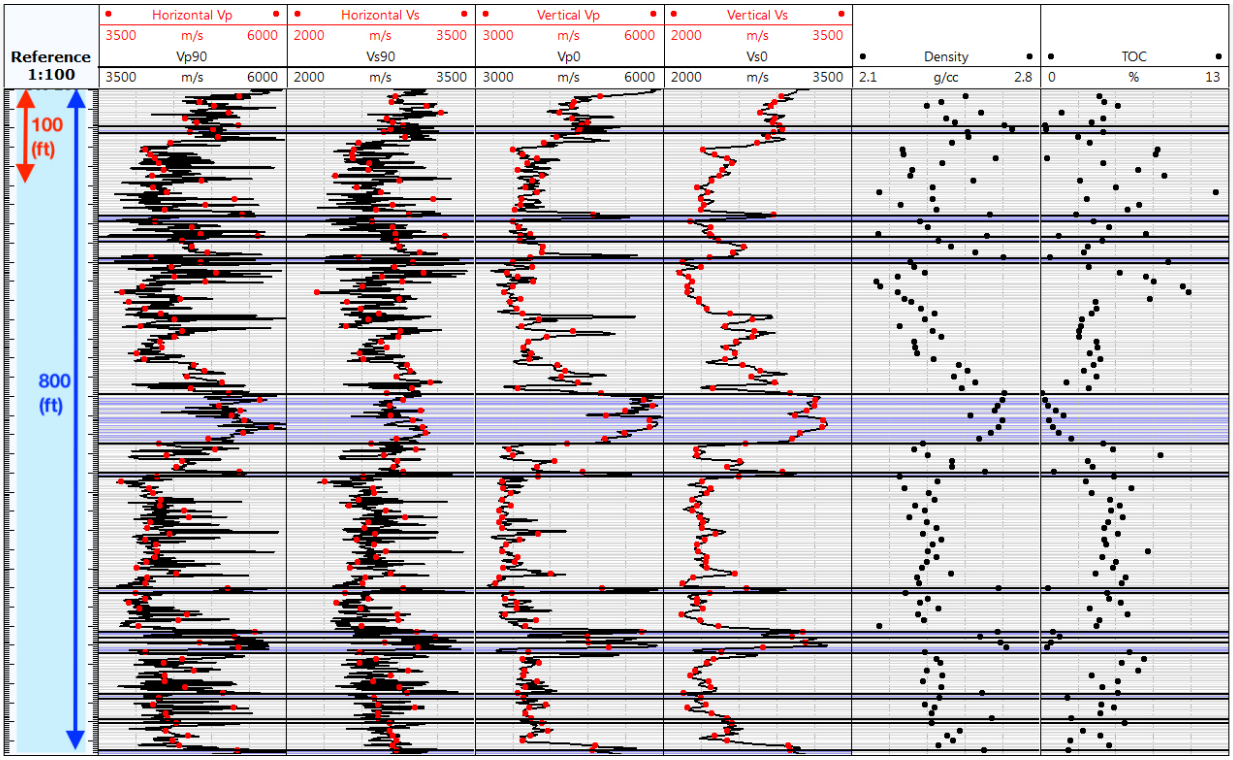

Figure 4.1: A well for Bone Spring formation and Avalon shale: $V_P(90°)$, $V_{SH}(90°)$, $V_P(0°)$, $V_S(0°)$, ρ, and TOC for 122 data points. Interbedded limestones are highlighted in blue.

Model	Kerogen (v/v)	ρ (g/cm^3)	$V_P(0°)$ (km/s)	$V_P(90°)$ (km/s)	$V_S(0°)$ (km/s)	$V_{SH}(90°)$ (km/s)	ε	γ	δ
Upper Layer	0	2.63	5.05	5.05	2.90	2.90	0	0	0
Lower Layer	0	2.54	4.23	4.70	2.71	2.92	0.12	0.08	0.06
	0.1	2.42	3.96	4.54	2.50	2.80	0.16	0.13	0.08
	0.2	2.31	3.69	4.38	2.29	2.68	0.20	0.18	0.10
	0.3	2.19	3.42	4.22	2.09	2.56	0.26	0.25	0.12

Table 4.1: Two-layer models for the testing AVO inversions using full Zoeppritz and linearized approximations. The lower layer represents the target shale with various kerogen content. Model values are derived from analyses with a well described in Figure 4.1 except δ. The values of δ are referred from Lim et al. (2017).

- P- and S-wave velocities, and density, for the isotropic layer are known and values for the anisotropic layer are unknown.

With these properties, four two-layer models are generated with different values of kerogen content

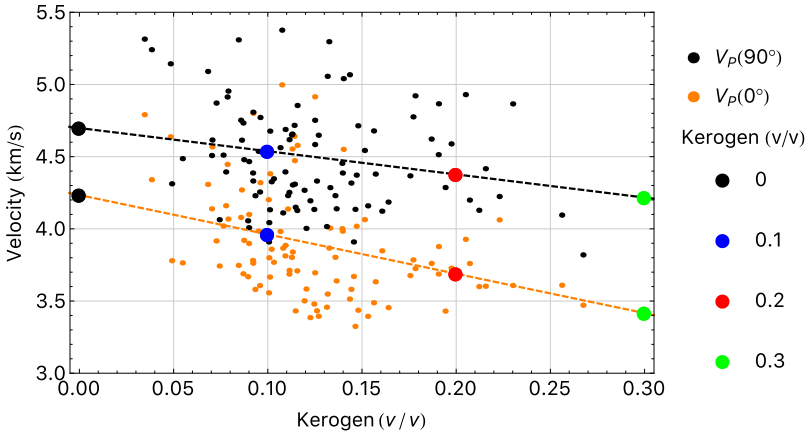

(a) $V_P(90°)$, $V_P(0°)$, and their model values

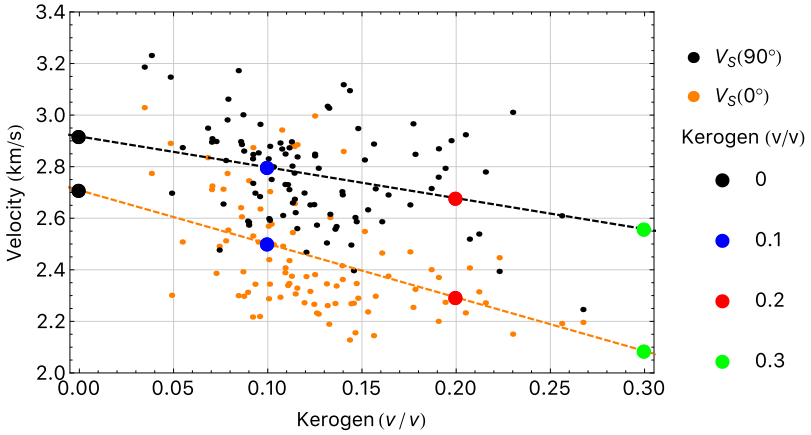

(b) $V_S(90°)$, $V_S(0°)$, and their model values

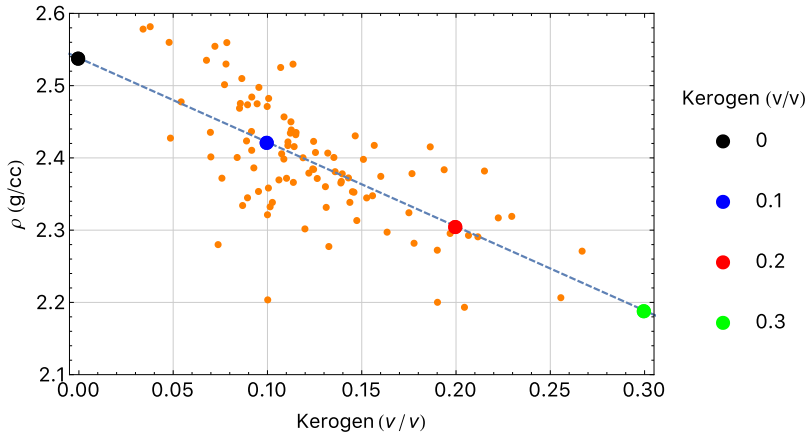

(c) ρ, and its model values

Figure 4.2: $V_P(90°)$, $V_P(0°)$, and their model values, $V_S(90°)$, $V_S(0°)$, and their model values, and ρ, and its model values

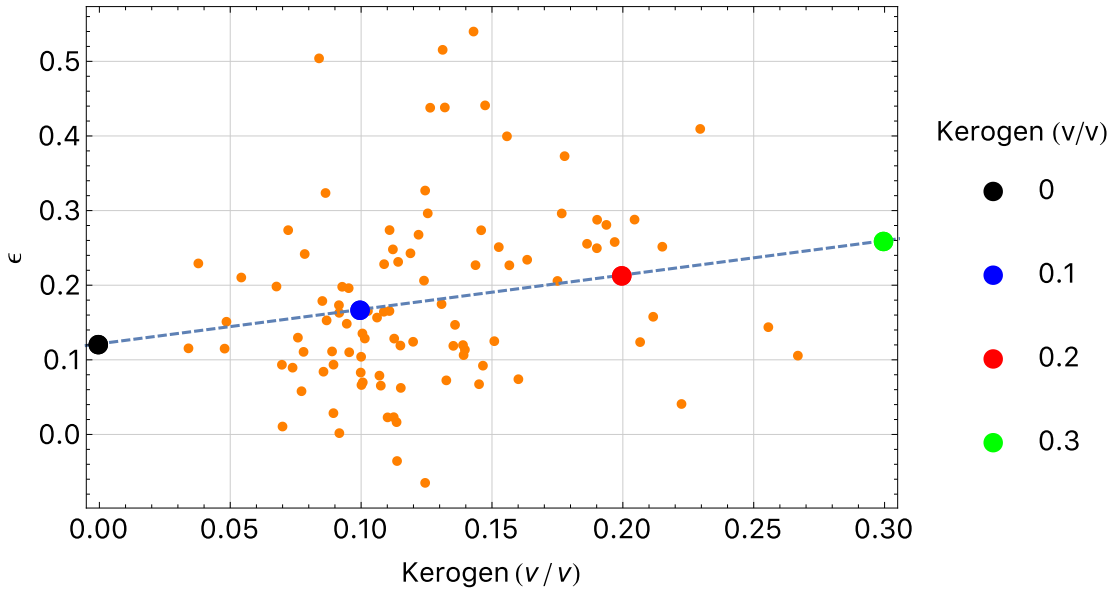

(a) ε

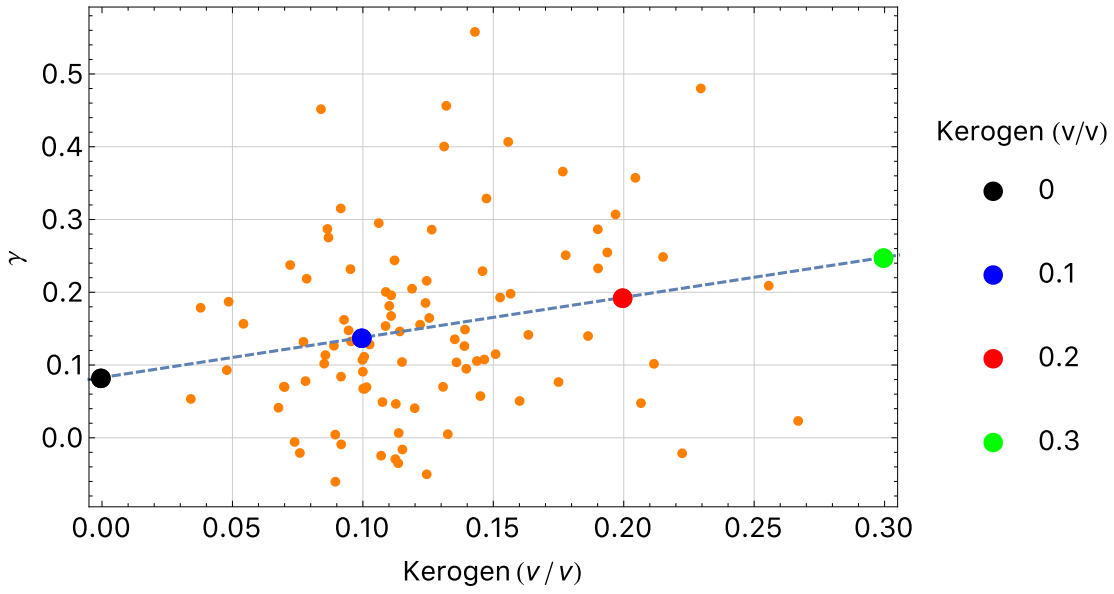

(b) γ

Figure 4.3: Thomsen parameters: ε, γ.

as shown in Table 4.1. Velocities and density for the upper, isotropic layer are from average values of interbedded limestones depicted in Figure 4.1. For the lower VTI shale layer, I applied a linear regression of the Avalon shale to develop an empirical model relating organic content to the velocities and density. The purpose of the variation of organic abundance in the lower layer is to

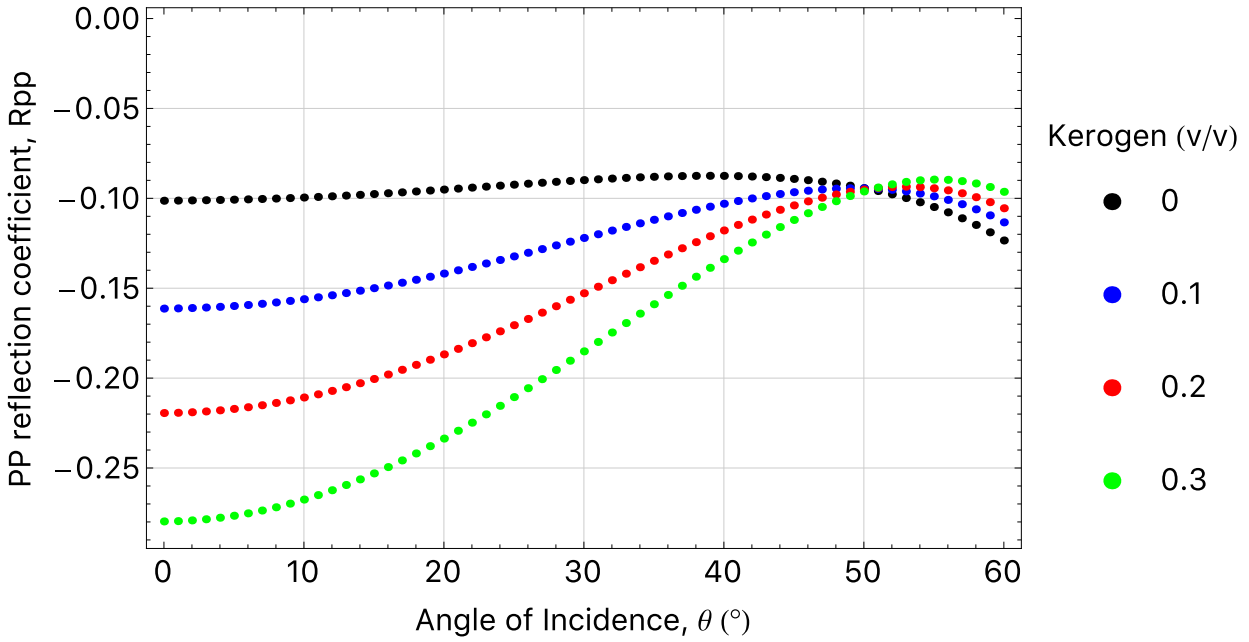

Figure 4.4: Exact anisotropic AVO responses (reflection coefficients) from the model interfaces in Table 4.1.

control the anisotropy level of given models. As already mentioned in section 2, organic matters are generally more soft and compliant than other minerals presented in shales. Therefore, their shapes and distribution are usually anisotropic and this consequently makes organic materials an important source of anisotropy in organic-rich shales.

The chosen models sample the range of kerogen content in the velocity dataset, ranging from 0 to 0.3 kerogen volume fraction, which is converted from measured TOC, with an increment of 0.1. The data and model values are depicted in Figures 4.2(a) (for P-wave velocity), 4.2(b) (for S-wave velocity), and 4.2(c) (for density). I then define their anisotropy levels with Thomsen's parameters ϵ and γ (Figure 4.3), noting I have no values for δ. Because there is no information on $V_P\ (45°)$ information in the dataset, δ is assumed from the values described in Lim et al. (2017). The values are empirically modeled with the dataset from Vernik (2016) which includes values of kerogen volume fraction and measured $V_P\ (45°)$ under a high confining pressure of 50 to 70 (MPa) for ten different shale formations.

With the model values, exact anisotropic PP-reflection coefficients are computed by a paraxial

ray tracing (Gibson et al., 1991), which effectively solves the two-point problem of finding the ray that connects exactly a specific source and receiver (Figure 4.4). It is possible due to the fact that the paraxial method can allow extrapolation of the information on a given ray to nearby receiver locations. The range of angle of incidence for the reflections is from 0° to 60°. These AVO curves provide test data for the AVO inversion.

4.2.2.2 Inversion Results

Figure 4.5 compare inversion of the synthetic test data using the proposed nonlinear Zoeppritz inversion and a more typical linearized AVO inversion based on the solution from Fatti et al. (1994), which is

$$R_{PP}(\theta) = c_1 R_P(0^\circ) + c_2 R_S(0^\circ) + c_3 R_D, \tag{4.8}$$

$$\begin{aligned}
\text{where} \quad c_1 &= 1 + \tan^2\theta \\
c_2 &= -8K\sin^2\theta \\
c_3 &= 2K\sin^2\theta - \frac{1}{2}\tan^2\theta \\
K &= \left[\frac{\bar{V_P}}{\bar{V_S}}\right]^2 \\
R_P(0^\circ) &= \frac{1}{2}\{\frac{\Delta V_P}{\bar{V_P}} + \frac{\Delta\rho}{\bar{\rho}}\} \\
R_S(0^\circ) &= \frac{1}{2}\{\frac{\Delta V_S}{\bar{V_S}} + \frac{\Delta\rho}{\bar{\rho}}\} \\
R_D &= \frac{\Delta\rho}{\bar{\rho}}.
\end{aligned}$$

Above Fatti et al. (1994)'s equation is a linearized approximation of PP reflection widely used to decouple P-wave velocity and density from acoustic impedance. Both near ($0^\circ \sim 20^\circ$) and far angle ranges ($0^\circ \sim 60^\circ$) of AVO curves in Figure 4.4 are considered as input data.

With the near angle range, the nonlinear method accurately estimates vertical P-wave velocity and the correct density for all values of kerogen volume fraction (Figures 4.5(a) and 4.5(e)). It also

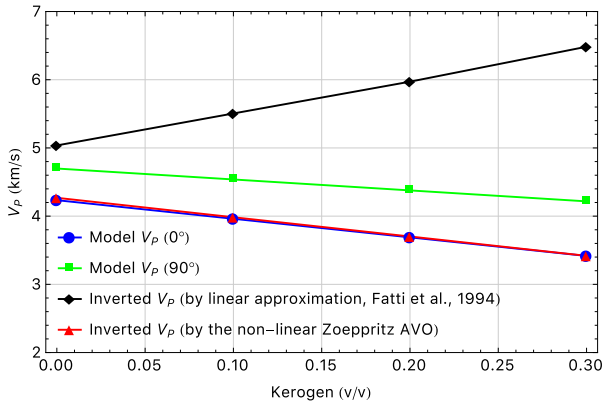

(a) V_P estimation with $0° \sim 20°$ AVO range

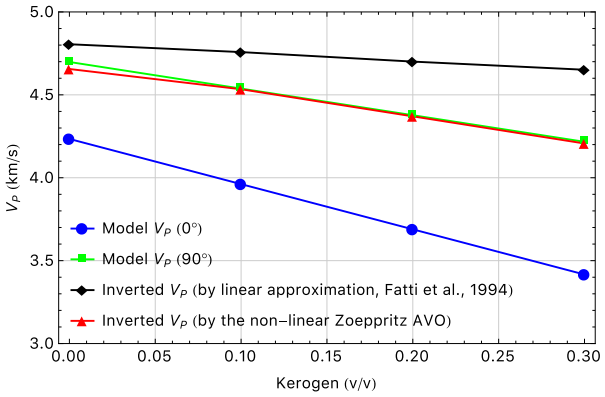

(b) V_P estimation with $0° \sim 60°$ AVO range

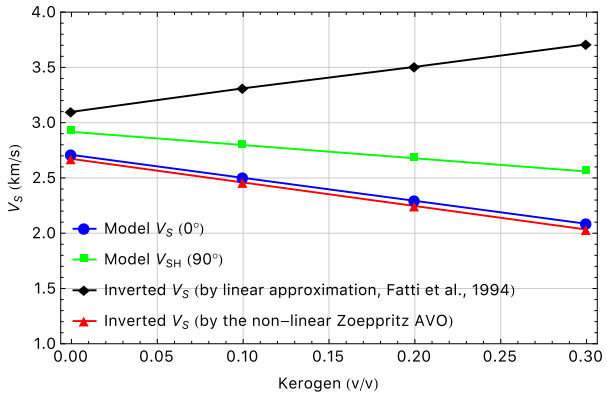

(c) V_S estimation with $0° \sim 20°$ AVO range

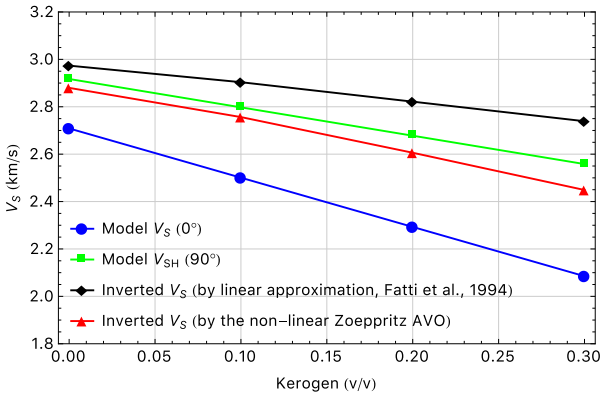

(d) V_S estimation with $0° \sim 60°$ AVO range

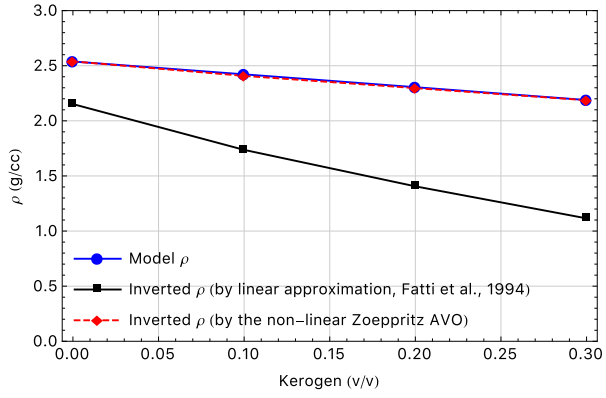

(e) ρ estimation with $0° \sim 20°$ AVO range

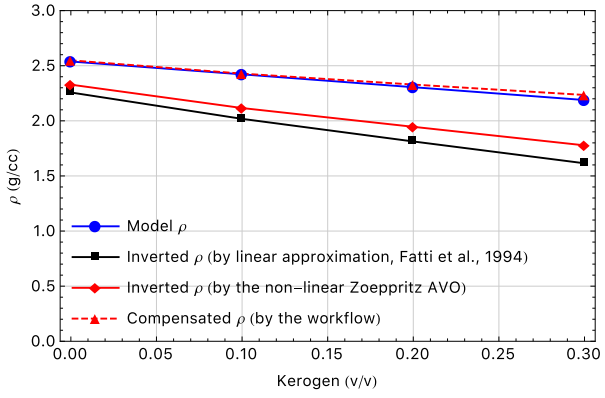

(f) ρ estimation with $0° \sim 60°$ AVO range

Figure 4.5: Estimated P-wave (V_P) and S-wave (V_S) velocities, and density (ρ) from the nonlinear AVO inversion. A near angle range ($0° \sim 20°$) and a far angle range ($0° \sim 60°$) are applied as data for inversion.

produces inverted S-wave velocity estimates that are still close to the model vertical velocity but less accurate compared to P-wave velocity estimates (Figures 4.5(c)). When the far angle range is used as input for the nonlinear inversion, the result remains consistently close to the horizontal P-wave and S-wave velocities (Figures 4.5(b) and 4.5(d)). However, the nonlinear inversion produces density estimates that are underestimated, with a discrepancy that increases with increasing anisotropy (red solid line in Figures 4.5(f)). The discrepancy is related to the degree of the anisotropy of P-wave velocity, ϵ, as theoretically shown in section 2 (equation 2.8). In contrast, the linearized inversion produces inaccurate velocity estimates that have a large difference from both true vertical and horizontal P-wave and S-wave velocities. The linearized inversion results for density have also larger errors than that from the nonlinear inversion.

4.2.2.3 Sensitivity analysis to understand the behavior of inversion results

As shown in above, vertical and horizontal velocities are inverted from the nonlinear Zoeppritz inversion, when near and far angle AVO ranges are applied as inversion inputs, respectively. To understand the systematic trend of the inversion results, I conduct a sensitivity test with a model in Table 4.1, the case of 0 kerogen volume fraction which corresponds to weak anisotropy (i.e., about 10% in *Thomsen's parameters*). The test is devised to compare AVO curves computed with the isotropic Zoeppritz equation and the exact anisotropic AVO response generated from Gibson et al. (1991). The comparison shows the effect of changing P-wave and S-wave velocities at the same time, whereas density is fixed as the exact model value. P-wave and S-wave velocities simultaneously vary in the Zoeppritz equation from their vertical velocities (i.e., $V_P(0^\circ)$ & $V_{SH}(0^\circ)$) to horizontal velocities (i.e., $V_P(90^\circ)$ & $V_{SH}(90^\circ)$) with the increment of 30° in angle of incidence. Table 4.2 describes the phase velocities in terms of the angle of incidence for P-wave and S-wave velocities. The values are determined with the following equations after elastic stiffness coefficients and density are modeled:

Incident Angle (°)	V_P (km/s)	V_{SH} (km/s)
0	4.23	2.71
30	4.32	2.76
30	4.56	2.87
60	4.70	2.92

Table 4.2: Phase velocities for the model that corresponds to a kerogen volume fractions of 0 in Table 4.1.

Kerogen (v/v)	c_{11}	c_{13}	c_{33}	c_{44}	c_{66}	ρ
0	56.0	11.1	45.5	18.6	21.6	2.54
0.1	49.9	10.7	38.0	15.1	19.0	2.42
0.2	44.2	10.1	31.4	12.1	16.5	2.31
0.3	38.9	9.3	25.5	9.5	14.3	2.19

Table 4.3: Elastic stiffness coefficients and density for the Avalon shale with kerogen volume fractions of 0, 0.1, 0.2, and 0.3. Their units are *GPa* and g/cc for elastic stiffness coefficient and density, respectively.

$$V_P(\theta) = (c_{11}\sin^2\theta + c_{33}\cos^2\theta + c_{44} + \sqrt{M})^{\frac{1}{2}}(2\rho)^{-\frac{1}{2}} \qquad \text{(Quasi-longitudinal phase velocity)}$$

$$V_{SH}(\theta) = \left(\frac{c_{66}\sin^2\theta + c_{44}\cos^2\theta}{\rho}\right)^{\frac{1}{2}}, \qquad \text{(Pure-shear phase velocity)} \qquad (4.9)$$

where

$$M = \left[(c_{11} - c_{44})\sin^2\theta - (c_{33} - c_{44})\cos^2\theta\right]^2 + (c_{13} + c_{44})\sin^2 2\theta \qquad (4.10)$$

Table 4.3 lists the model elastic stiffness coefficients and densities for all the level of organic carbon content. Among the models, values for 0 volume fraction of kerogen are used for calculation of the phase velocities.

As shown in Figure 4.6, when $V_P(0°)$ and $V_{SH}(0°)$ (the set of vertical velocities) are used, the green curve computed from the Zoeppritz equation, that used for isotropic AVO inversion, is almost matched to near angle range of the red line from the paraxial ray tracing, the forward

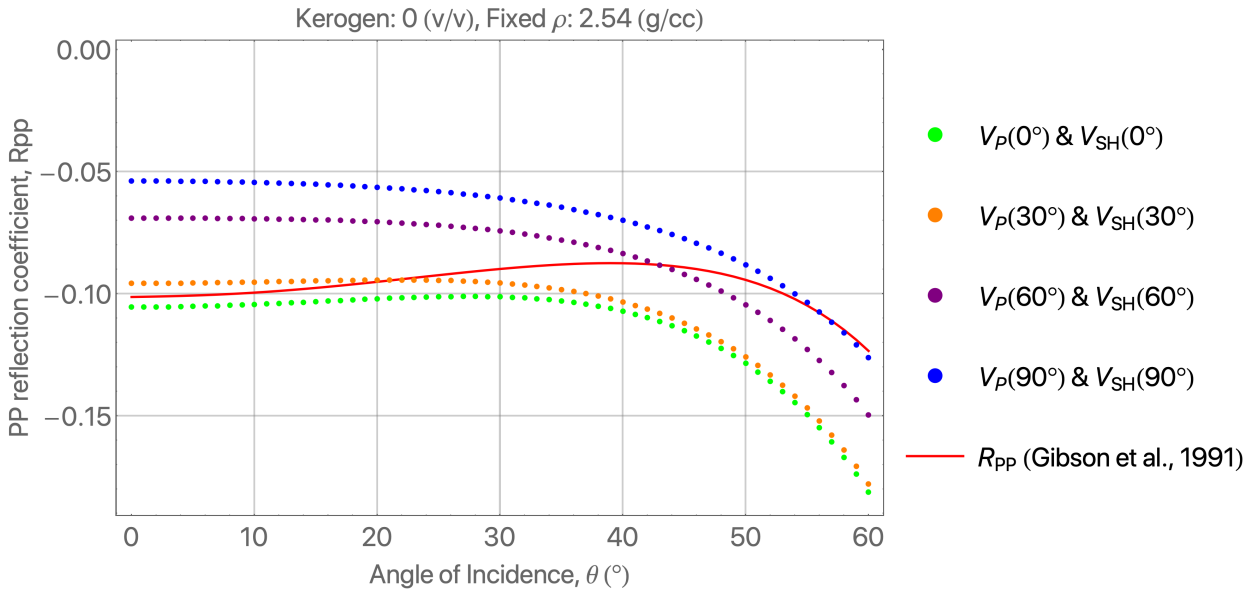

Figure 4.6: Comparison of AVO curves, dotted curves are generated by the Zoeppritz equation by varying Vp and Vs values. The red-colored solid line represents the AVO curve computed from the paraxial ray tracing (Gibson et al., 1991). Annotated $V_P(0°)$ & $V_{SH}(0°)$, $V_P(30°)$ & $V_{SH}(30°)$, $V_P(60°)$ & $V_{SH}(60°)$, and $V_P(90°)$ & $V_{SH}(90°)$ are corresponding to P-wave and S-wave velocities at $0°$, $30°$, $60°$, and $90°$ of incident angle, respectively.

modeled curve for anisotropy. On the other hand, the blue curve, generated with values of $V_P(90°)$ and $V_{SH}(90°)$ (the set of vertical velocities), is overlain with the far angle range of the red line. This observation can be evidence of the following arguments:

- Since the curvatures of the curves, which are generated by the Zoeppritz equation and the paraxial ray tracing, are different each other when the nonlinear Zoeppritz inversion tries to fit the data, which is generated by the paraxial ray tracing, an inverted density value should be underestimated.

- $V_P(0°)$ and $V_{SH}(0°)$ (i.e., vertical velocities) are inverted by the Zoeppritz inversion when a limited near angle range is applied as an input AVO. Likewise, $V_P(90°)$ & $V_{SH}(90°)$ (i.e., horizontal velocities) will also be achieved when a far angle range will be used for the non-linear inversion.

4.2.3 Workflow for estimation of seismic anisotropy, geomechanical properties, and TOC

From now, I propose an effective workflow to estimate seismic anisotropy, geomechanical properties, and TOC of organic-rich shale based on the analysis of the inversion results illustrated previously. Figure 4.7 summarizes the nonlinear inversion results and describes the workflow. This first illustrates how to estimate seismic anisotropy, specifically ϵ and γ. In addition, it describes the way to compensate the underestimated density (estimated with far angle range) to the correct density with the determined ϵ.

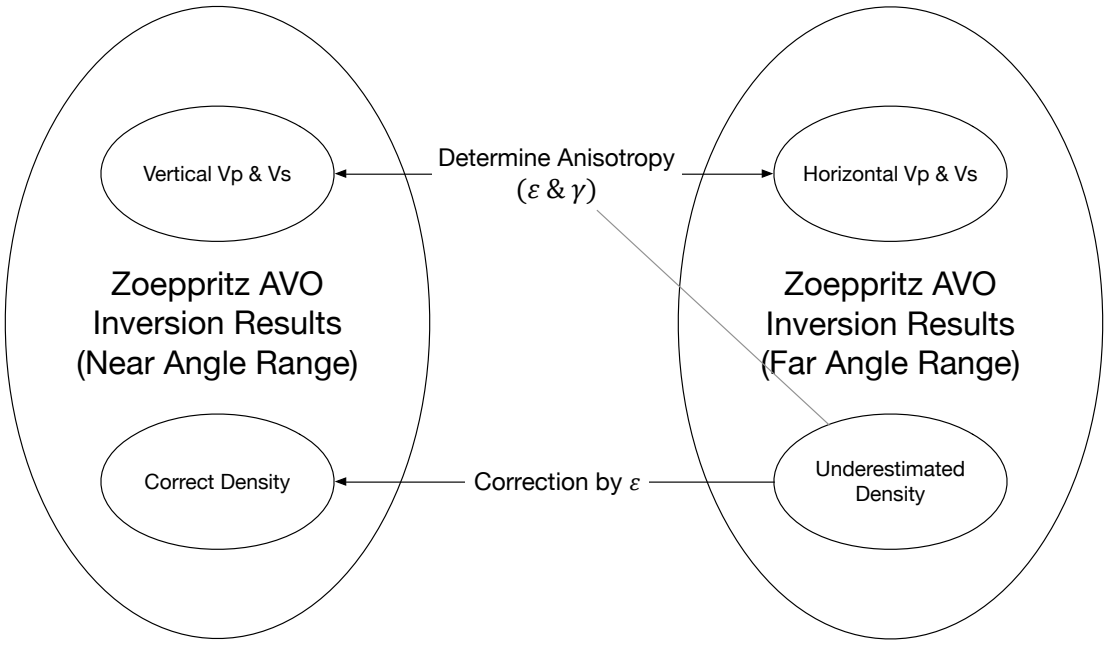

Figure 4.7: A workflow to estimate seismic isotropy (ϵ and γ). It summarizes the inversion results for P-wave and S-wave velocities and density. It also describes how to compensate the underestimated density to correct density by the determined ϵ.

The nonlinear inversion successfully determined vertical and horizontal velocities with near and far angle ranges, respectively. Therefore, by comparing the determined horizontal and vertical values, such seismic anisotropies can be estimated: ϵ for P-wave velocity and γ for S-wave velocity. In order to compute values of ϵ and γ from inverted P-wave and S-wave velocities, following

formulations from Thomsen (1986) are used:

$$\varepsilon = \frac{V_P^2(90°) - V_P^2(0°)}{2V_P^2(0°)} \tag{4.11}$$
$$\gamma = \frac{V_{SH}^2(90°) - V_{SH}^2(0°)}{2V_{SH}^2(0°)}$$

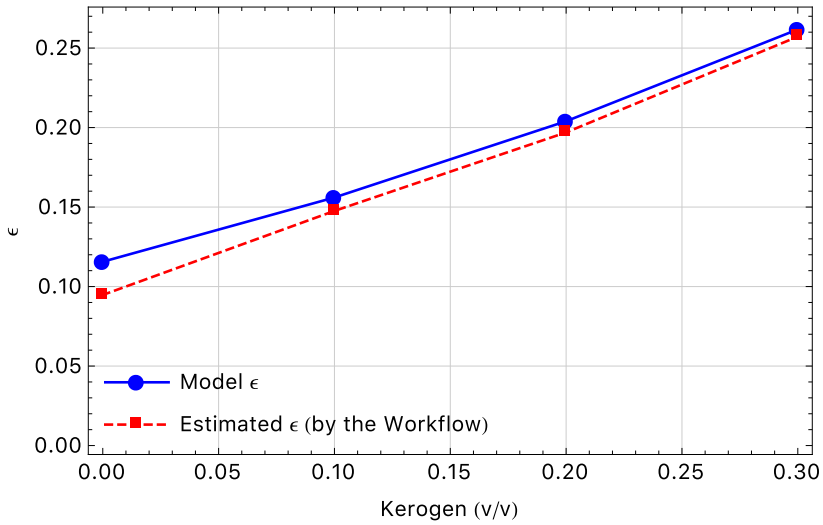

(a) Epsilon (ε) estimation

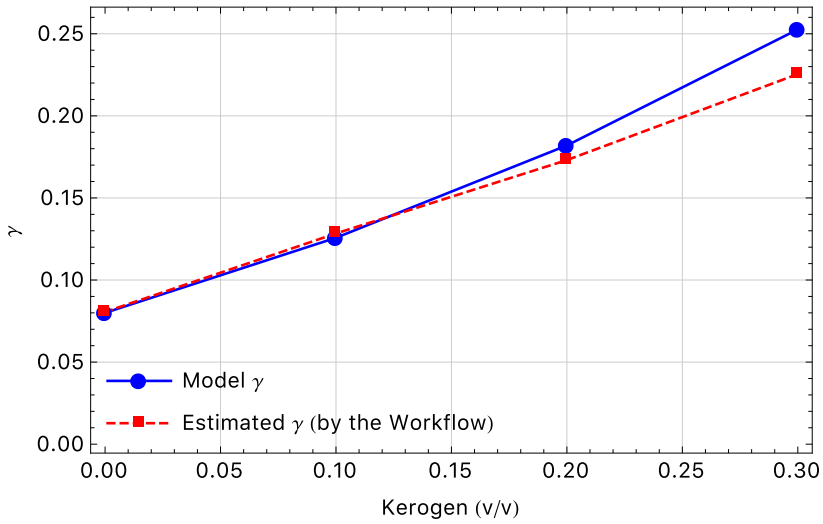

(b) Gamma (γ) estimation

Figure 4.8: Estimation of seismic anisotropy with Thomsen's parameters ϵ and γ.

Figure 4.8 depicts the estimations of ϵ and γ by applying the workflow with the nonlinear inversion results described in Figure 4.5. For ϵ, although the workflow keeps generating constant errors along with all target kerogen volume fractions, it does predict correctly the rate of the change in ϵ. Whereas, the error of γ increases with increasing organic content. Nonetheless, the workflow is accurately estimating both ϵ and γ with the proposed nonlinear inversion by providing small errors less than 12% for all the range of kerogen volume fraction.

Besides the estimation of anisotropy, the underestimated density can be compensated to correct density with the workflow, since discrepancy is related to the degree of the anisotropy of P-wave velocity, ϵ, as theoretically derived in section 2 (equation 2.8). With the estimated ϵ (red colored values in Figure 4.8(b)), the underestimated density (red solid line in Figures 4.5(f)) is now corrected to a better estimation (red dashed line in Figures 4.5(f)).

Inverted parameters from the AVO inversion can also be used to estimate properties of interest such as Young's modulus and Poisson's ratio for geomechanical analyses. Since I obtained all necessary information such as horizontal and vertical P-wave and S-wave velocities, correct density, and seismic anisotropy (except δ or c_{13}) from the inversion and the workflow, Young's modulus and Poisson's ratio in both horizontal and vertical direction can be computed. Young's modulus and Poisson's ratio of VTI medium are expressed with elastic stiffness coefficients (King, 1964; Banik et al., 2012) as following:

$$
\begin{aligned}
E_V &= \frac{c_{33}(c_{11}-c_{66})-c_{13}^2}{c_{11}-c_{66}} \quad (=E_3) \\
E_H &= \frac{4c_{66}(c_{33}(c_{11}-c_{66})-c_{13}^2)}{c_{11}c_{33}-c_{13}^2} \quad (=E_1=E_2) \\
\nu_V &= \frac{c_{13}}{2(c_{11}-c_{66})} \quad (=\nu_{31}=\nu_{32}) \\
\nu_{HV} &= \frac{2c_{13}c_{66}}{c_{11}c_{33}-c_{13}^2} \quad (=\nu_{13}=\nu_{23}) \\
\nu_{HH} &= \frac{c_{33}(c_{11}-2c_{66})-c_{13}^2}{c_{11}c_{33}-c_{13}^2} \quad (=\nu_{12}=\nu_{21})
\end{aligned}
\tag{4.12}
$$

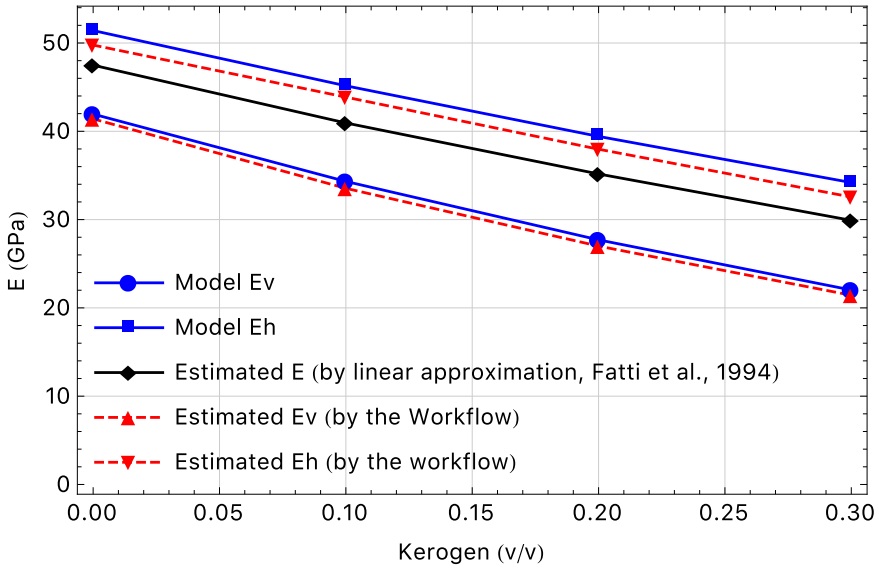

(a) Young's modulus estimation

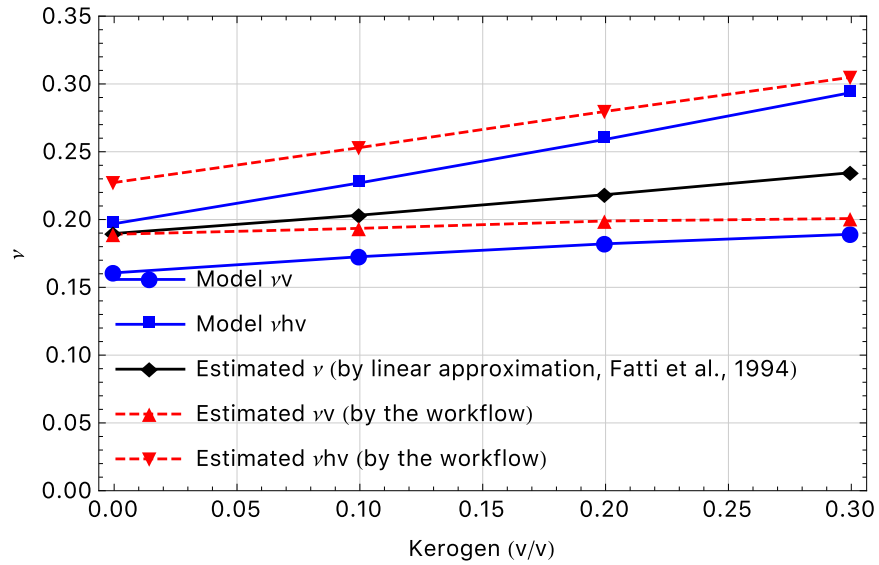

(b) Poisson's ratio estimation

Figure 4.9: Estimation of geomechanical properties in horizontal and vertical directions.

This does require that I assume reasonable values for δ. In this case, I apply model δ values in Table 4.1 to the estimation. Estimated values for Young's modulus for the test models are shown in Figure 4.9(a), and Figure 4.9(b) shows the Poisson's ratio estimates. Another estimation for the parameters from Fatti's inversion is also given for comparison. While only one value of geomechanical properties can be computed from the linearized method, the nonlinear approach

accurately estimates Young's modulus in both horizontal and vertical directions with all values of kerogen volume fractions. The errors for vertical and horizontal values between estimations and models are less than 1% and 4% for all the range of organic abundance, respectively. In contrast, estimates of Poisson's ratio are constantly shifted from true values although it still predicts the rate of change related to kerogen volume fractions. One possible explanation of the discrepancy between model and inverted Poisson's ratio could be the lack of accurate δ information. If more reliable δ values of target shale can be obtained from direct measurements of $V_P\ (45°)$ values, a better estimation of Poisson's ratio can be achieved.

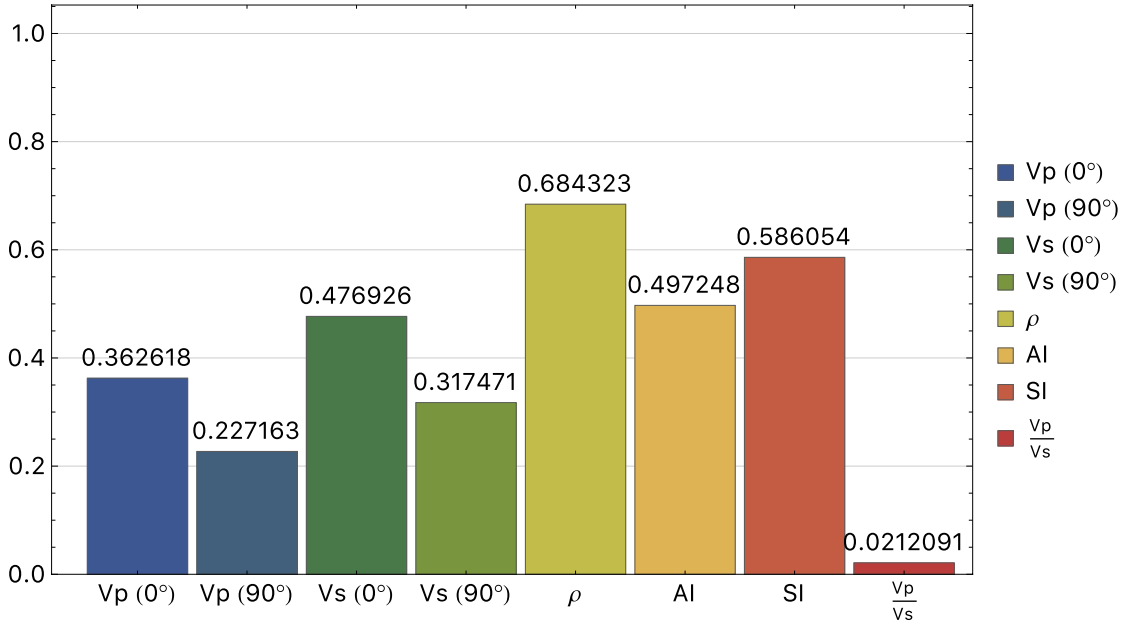

Figure 4.10: Absolute values of correlation coefficients between geophysical parameters and TOC for the Avalon shale described in Figure 4.1.

For TOC estimation from elastic properties, I first calculate correlation coefficients between the various parameters and TOC for Avalon shale in the Delaware basin (Figure 4.10). Only shale intervals in Figure 4.1 were considered and interbedded limestones are excluded. As shown in Figure 4.10, density is the most correlated to the organic carbon content for the Avalon shale.

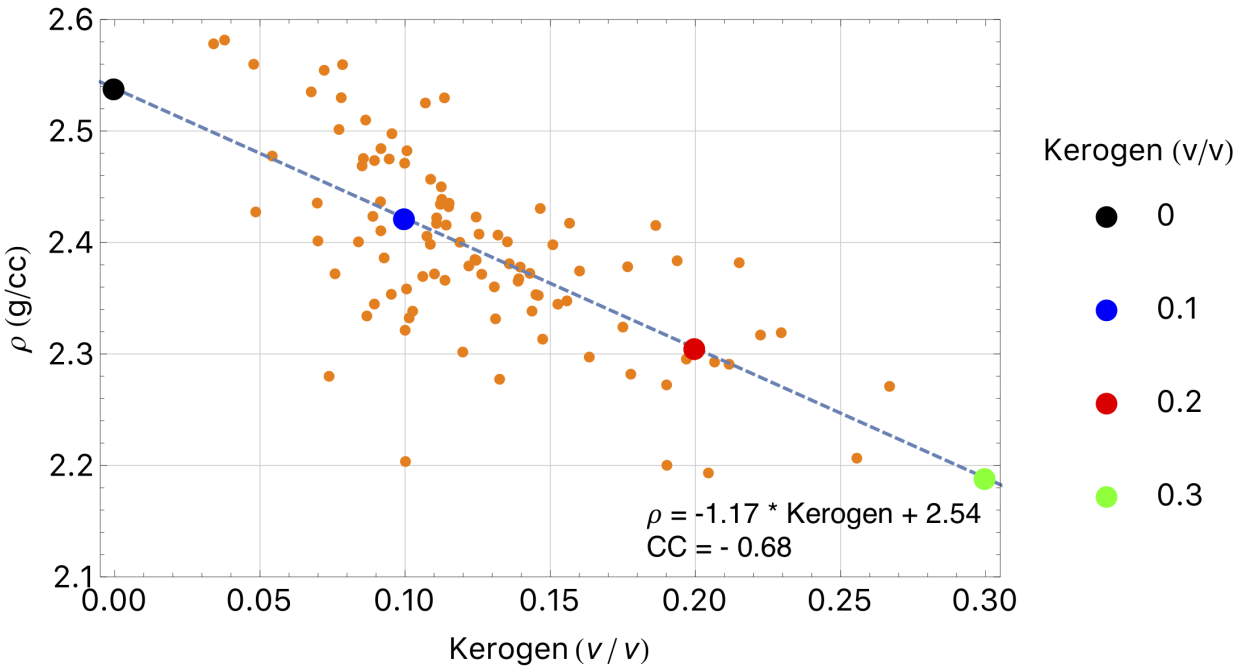

Figure 4.11: A cross-plot between density and kerogen volume fraction for the Avalon shale described in Figure 4.1. A linear regression line is generated to model density values with respect to kerogen volume fraction.

Therefore, estimated density from the workflow will be used for the estimation of TOC, since the nonlinear Zoeppritz inversion can effectively decouple density and P-wave velocity as previously verified. In order to build an empirical rock physics relationship between kerogen volume fraction and density, I convert the measured TOC to kerogen volume fraction by using an equation described in Vernik (2016):

$$Kerogen\ (v/v) = 2.6 \cdot \frac{TOC\ (wt\%)}{100} \tag{4.13}$$

I then develop the following relationship by cross-plotting and linear regression of the data as illustrated in Figure 4.11:

$$Kerogen\ (v/v) = \frac{2.54 - \rho(g/cm^3)}{1.17} \tag{4.14}$$

The empirical relationship is now applied to estimate kerogen volume fraction from the density. For the estimation, following three density values are used:

1. density inverted by Fatti's linear inversion with $0^\circ \sim 60^\circ$ AVO ranges (black line in Figures 4.5(f))

2. density first inverted by the nonlinear inversion with $0^\circ \sim 60^\circ$ AVO ranges, then compensated with the workflow in Figure 4.7 (red dashed line in Figures 4.5(f))

3. density inverted by the nonlinear inversion with $0^\circ \sim 20^\circ$ AVO ranges (red dashed line in Figures 4.5(e))

Figure 4.12 shows the estimation of organic abundance in kerogen volume fraction. In contrast to the estimation by the density obtained from linearized inversion, when the nonlinear inversion and the proposed workflow are applied, the organic carbon content in the models are accurately estimated due to their better density estimation.

4.2.4 Sensitivity test and new seismic-anisotropy attribute: $|\Delta V_P|$

From now on, I present a new seismic attribute named after ΔV_P. It is developed to more practically estimate seismic anisotropy from real seismic data. For the development, I first conduct a sensitivity test with various source-receiver offsets (i.e., angles of incidence). The nonlinear Zoeppritz AVO inversion is applied with the previous Avalon shale model again.

Figure 4.13 describes inversion results using the full Zoeppritz AVO inversion with six different AVO angle ranges. As illustrated, when the maximum angle values of the applied AVO ranges are smaller than 20°, the full Zoeepritz AVO inverts the P-wave velocities that are very close to vertical model values. On the other hand, when the maximum angle values of the applied AVO ranges are bigger than 40°, the Full Zoeepritz AVO inverts the P-wave velocities that are similar to horizontal

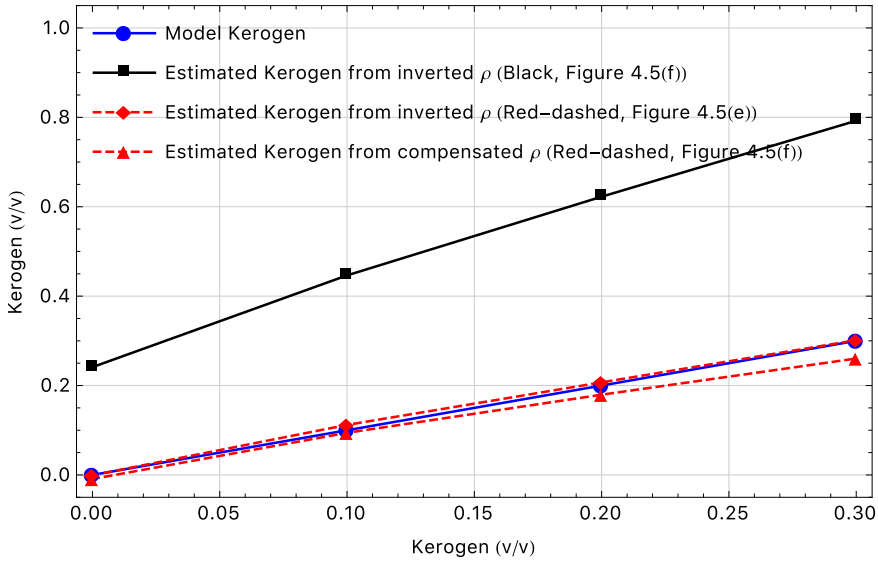

Figure 4.12: Estimated kerogen volume fraction with respect to model kerogen values. Three different approaches are applied for the estimations.

values regardless of their level of anisotropy. In addition, the inversion generates various P-wave velocity from vertical to horizontal values with an intermediate AVO range (here, $0^\circ \sim 30^\circ$). The model values of kerogen volume fraction, which correspond to levels of anisotropy, control what value is determined from the inversion with the AVO range. This also shows that a larger far angle range is required to estimate horizontal velocity for stronger anisotropy. Above all, the sensitivity test implies the level of anisotropy can be determined by comparison of the P-wave velocity estimates that are inverted with two differently applied AVO ranges.

For example, when I subtract a P-wave velocity prediction ($V_{P.\text{near}}$), for which a relatively near AVO angle is applied, from another prediction ($V_{P.\text{far}}$) with a far angle range, the level of anisotropy can be defined in a quantitative way as formulated in following:

$$\Delta V_P = V_{P.\text{far}} - V_{P.\text{near}} \tag{4.15}$$

Figure 4.14 shows the effectiveness of the proposed new seismic-anisotropy attribute, ΔV_P, for inferring the level of anisotropy of the model. In Figure 4.14(a), the ΔV_P attribute is computed by

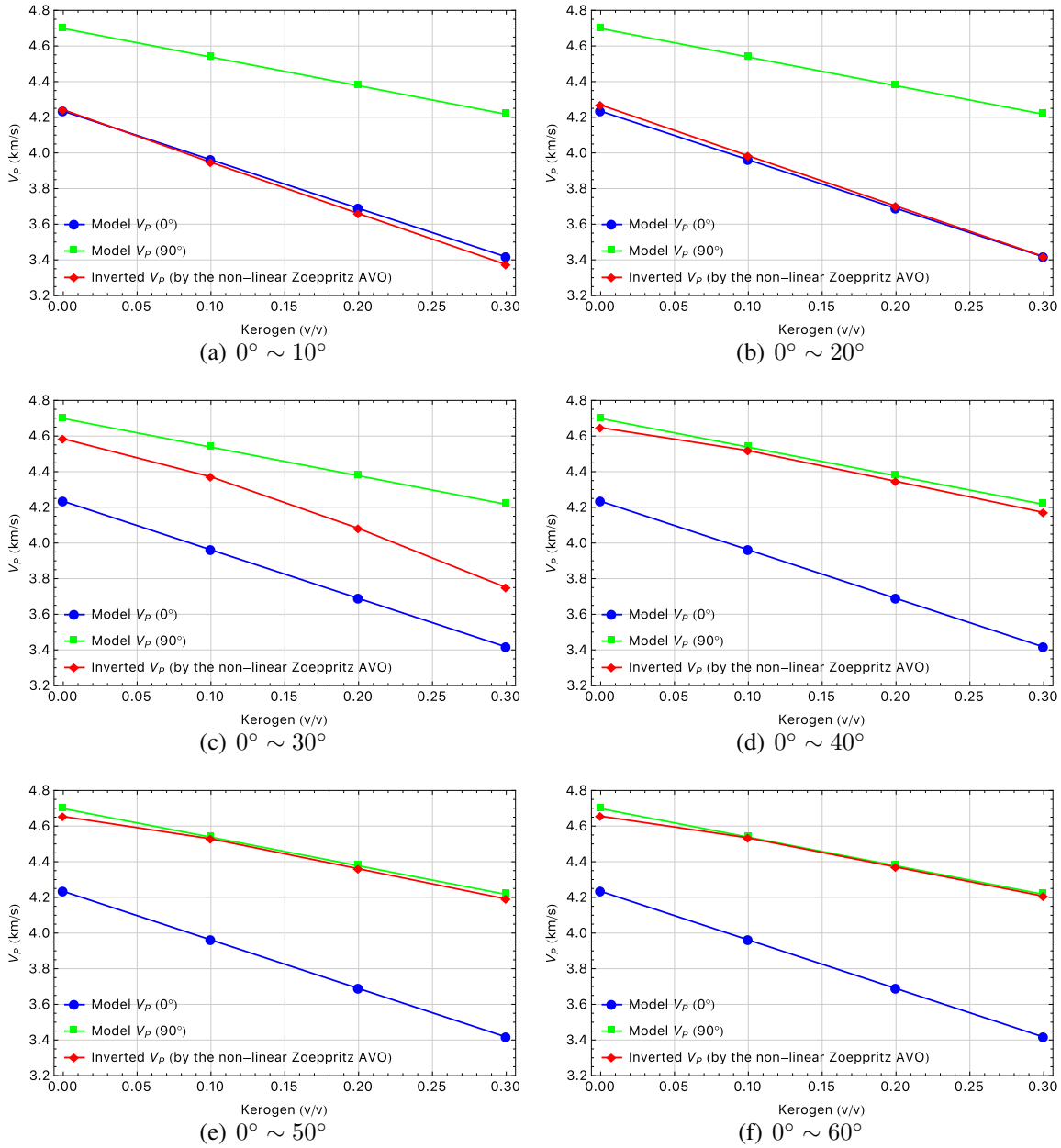

(a) $0° \sim 10°$ (b) $0° \sim 20°$

(c) $0° \sim 30°$ (d) $0° \sim 40°$

(e) $0° \sim 50°$ (f) $0° \sim 60°$

Figure 4.13: Inverted P-wave velocity with six different AVO ranges. The non-linear Zoeppritz AVO inversion is applied for the sensitivity test by varying the AVO ranges.

subtracting two different inversion results which are inverted with far and near AVO angle ranges (here $0° \sim 50°$ and $0° \sim 20°$), respectively. For the case of Figure 4.14(b), the narrow range is now applied as $0° \sim 30°$. Both cases clearly show higher values of ΔV_P correspond to higher levels of anisotropy of the models.

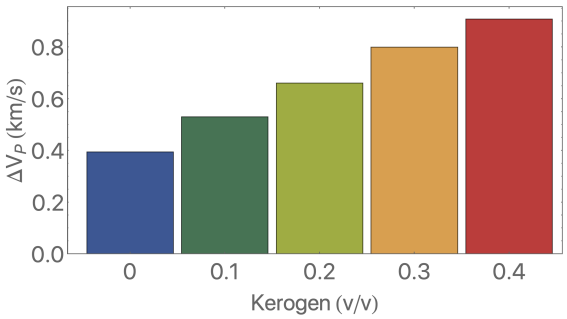

(a) Subtraction of inverted V_P in Figures 4.13(e) and 4.13(b)

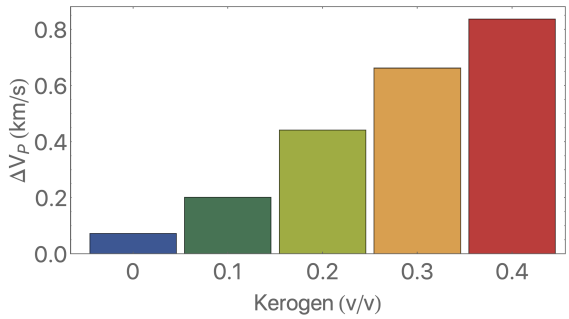

(b) Subtraction of inverted V_P in Figures 4.13(e) and 4.13(c)

Figure 4.14: New seismic-anisotropy attribute: $|\Delta V_P|$. Colors correspond to kerogen volume fractions. Note that the value of $|\Delta V_P|$ increases with the increase of kerogen volume fraction.

4.3 Field Case Study: Gulf of Mexico (SE of New Orleans, LA)

From now, I apply the ΔV_P attribute in a field data example to infer the level of seismic anisotropy from a real seismic data. The dataset originates from a field of Gulf of Mexico (GOM) in the southeast of New Orleans, Louisiana. Details of the dataset are already described in section 2. In order to test the proposed ΔV_P attribute, two different AVO ranges ($4^\circ \sim 44^\circ$ and $4^\circ \sim 32^\circ$) are first applied with the nonlinear Zoeppritz AVO inversion before generating the ΔV_P attribute (Figures 4.15(a) and 4.15(b)). Finally, the target seismic attribute and its absolute values are generated (Figures 4.15(c) and 4.15(d)). Although a set of anisotropy logs is not available in the dataset to evaluate seismic anisotropy, it includes a gamma-ray (GR) log which can assess the amount of shale contents that should be highly correlated to seismic anisotropy. Therefore, the effectiveness of the attribute for inference of seismic anisotropy can indirectly be verified by comparing to the GR log as shown in Figure 4.16. Values along with the GR log and $|\Delta V_P|$ are first normalized for a direct comparison. In addition, I respectively applied 110 Hz and 125 Hz as low pass and high cut frequencies for the generation of low-pass filtered GR log. It is due to the fact that the maximum frequency of the seismic data is about 125 Hz since the data is sampled in 4 ms. Cross-correlation between two normalized value is quite low as about 0.2 (Figure 4.16(a)) due to the difference of the resolutions of two different methods (i.e., GR log and seismic inversion). However, when the en-

velopes of each curve (i.e., normalized and filtered GR log, and normalized $|\Delta V_P|$) are computed as depicted in Figure 4.16(b) with the same scale to preserve local peaks of pre-defined values, there is a meaningful correlation with over 0.7 cross-correlation value. This shows the potential of the proposed attribute, ΔV_P, to evaluate the level of seismic anisotropy.

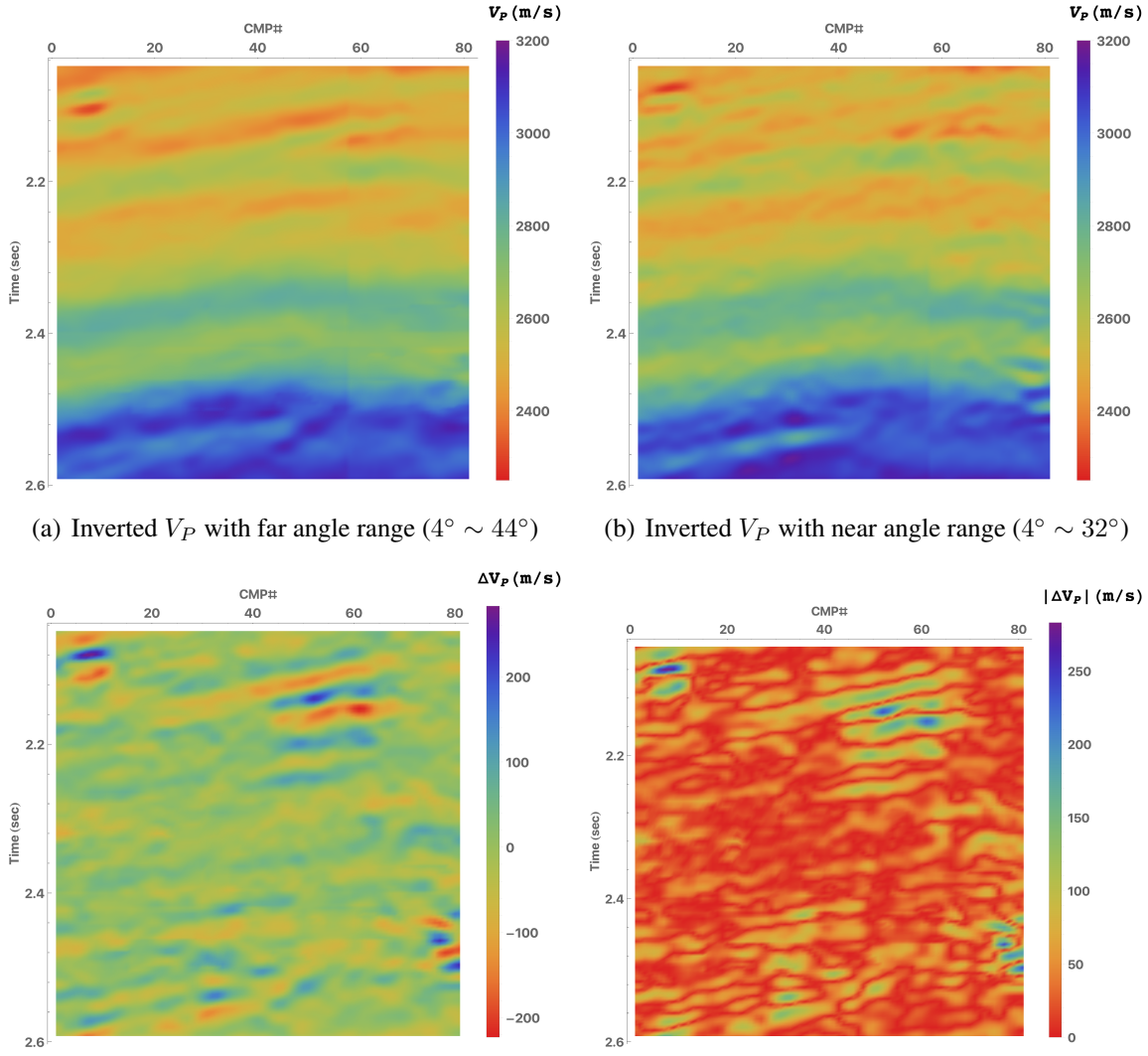

(a) Inverted V_P with far angle range ($4° \sim 44°$)

(b) Inverted V_P with near angle range ($4° \sim 32°$)

(c) ΔV_P, (a) - (b)

(d) $|\Delta V_P|$, |(a) - (b)|

Figure 4.15: Inversion results for V_P with relatively far (a) and near (b) angle ranges, their difference (ΔV_P), and its absolute value ($|\Delta V_P|$).

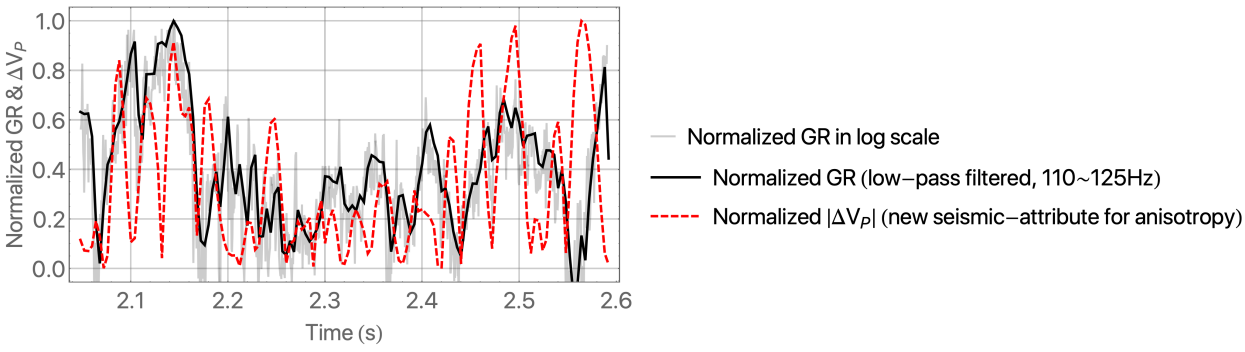

(a) Normalized GR and $|\Delta V_P|$

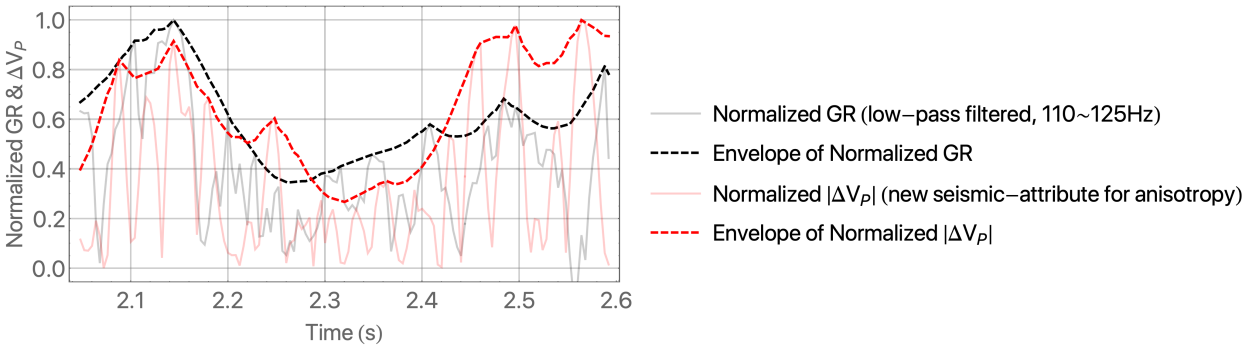

(b) Envelopes of normalized GR and $|\Delta V_P|$

Figure 4.16: Comparison between anisotropy attribute (ΔV_P), and Gamma-ray log (raw and low-pass filtered).

4.4 Conclusions and Discussion

In the section, I proposed a workflow to estimate seismic anisotropy, geomechanical properties, and total organic carbon (TOC) content of shale.

With the workflow, AVO inversion using the full Zoeppritz equations can characterize seismic anisotropy and geomechanical properties of Avalon shale that are overlain by an isotropic limestone layer. The inversion accurately determines horizontal P-wave and S-wave velocities when a far angle range is applied as input data. With a near angle range, the inversion can obtain reliable vertical velocities, and correct density, although the inversion is more sensitive to the target parameters when a limited AVO range is applied (Appendix B). Consequently, seismic anisotropy can be estimated by comparison of these inverted horizontal and vertical velocities. In addition,

geomechanical properties are also reliably determined in both horizontal and vertical directions.

The nonlinear Zoeppritz AVO inversion can also characterize the organic carbon content of Avalon shale. For this, I first built an empirical rock physics relationship between the density and organic kerogen content of the shale. Since the inversion correctly estimates density when a near angle range is applied as input data, kerogen volume fraction can accurately be determined from the empirical relationship. Although the inversion underestimates density values with a far angle AVO range, it can be corrected with the anisotropy of P-wave velocity determined by the proposed workflow. Consequently, the organic carbon content in the shale can correctly be inferred from the densities estimated from two different approaches.

Lastly, I introduced a new seismic attribute (ΔV_P) in order to more practically estimate seismic anisotropy from real seismic data. The attribute is developed from the following results from a sensitivity test:

- When the model is anisotropic and two different AVO ranges (i.e., relatively near and far angle ranges) are applied for the nonlinear Zoeppritz inversion, significantly different P-wave velocities are inverted.

- Once the two inverted values are subtracted from each other, the difference, which is the seismic attribute (ΔV_P), increases with the increase of model anisotropy.

In a given field seismic test, ΔV_P is well correlated with a gamma-ray (GR) log, which in turn is related to the amount of clay or shale content and should be highly correlated with seismic anisotropy. Therefore, these results support the effectiveness of the attribute for inference of the degree of seismic anisotropy.

In contrast to linear AVO inversion methods which generate only one isotropic value for target properties, the inversion method can estimate values for both horizontal and vertical P-wave and S-wave velocities. In addition, the inversion provides correct density for anisotropic media. A combination of those better estimations of the elastic parameters can eventually allow estimation of geomechanical properties in both horizontal and vertical directions, whereas other methods only

can estimate one value for the geomechanical properties.

Other potential applications of the nonlinear Zoeppritiz inversion and the seismic attribute ΔV_P include estimations of δ and TOC. Although estimations of seismic anisotropy for ϵ and γ are only demonstrated in the section, seismic anisotropy δ may also further be inferred with the proposed workflow by varying input AVO angle ranges. When the δ value and correct model Poisson's ratio are respectively set as unknown and known, the nonlinear AVO inversion is now changed to another type of inverse problem to estimate correct δ value. The proposed seismic anisotropy attribute ΔV_P may also be used to infer organic abundance in an unconventional shale reservoir. It is due to the fact that organic carbon content in shale is also strongly related to seismic anisotropy as discussed in the section.

5. CONCLUSIONS AND FUTURE WORK AND DISCUSSION

5.1 Conclusions

In the preceding sections, I have investigated a new nonlinear AVO inversion based on the Zoeppritz equation in order to accurately estimate the elastic and rock properties of target subsurface layers. Specifically, the inversion is devised for the layers which are highly anisotropic and often surrounded by hard layers to generate strong contrasts.

I first proposed a nonlinear AVO inversion based on exact Zoeppritz solutions for P-wave reflection amplitudes. The reformulation of the parameters in the Zoeppritz equation and application of an adjoint technique make the nonlinear inversion possible. In contrast to traditional AVO inversions using a linearized approximation of the reflection, the inversion does not require any prerequisite assumptions such as the linear relationship between parameters, and the background ratio between P- and S-wave velocities. Instead, the nonlinear Zoeppritz inversion can independently estimate contrasts of target parameters. It consequently leads to better estimation of P- and S-wave velocities, and density. The effectiveness of the proposed AVO inversion is verified with a synthetic model and a field seismic study. The given synthetic case study shows that, when a far offset AVO data is available, AVO inversion using the full Zoeppritz equation can correctly characterize geophysical and geomechanical properties of possible target shales that are overlain by isotropic layers. Specifically, Inverted P-wave and S-wave velocities are approximately equal to the horizontal velocities of the target shales, and inverted density is underestimated. However, the underestimated density can be corrected, once the level of anisotropy can be determined by comparing inverted horizontal velocity and vertical values. In addition, the inversion predicts the rate of change in geomechanical properties with increasing seismic anisotropy of the model. The results with the given field seismic study also strengthen that the inversion more accurately determines P-wave and S-wave velocities, density, and the ratio between P- and S-wave velocities compared to linear inversion.

I then constructed a new AVO inversion jointly using exact P-wave reflection and converted PS-reflection together to overcome following technical challenges required for typical AVO inversions using P-wave reflection only: 1) An expensive long-offset acquisition is required for decoupling density and P-wave velocity, 2) An accurate background the ratio of averaged P-wave and S-wave velocities between two target layers, $\frac{\bar{V_P}}{\bar{V_S}}$, has to be assumed before inversion, and 3) AVO inversion is very sensitive to signal-to-noise ratio. For the development, I newly derived the derivatives of the PS-wave reflection coefficient in terms of model parameters by applying a combination of the reformulation of parameters in the Zoeppritz equation and the adjoint state technique. In a given synthetic model test, the PP- and PS-Joint AVO inversion based on exact Zoeppritz equations can successfully estimate horizontal P-wave and S-wave velocities of an inferred case of the Upper Eagle Ford overlain by Austin Chalk, for all levels of seismic anisotropy. The inversion also accurately determines shear impedance and background $\frac{\bar{V_P}}{\bar{V_S}}$. Above all, all target parameters can correctly be recovered by the Joint inversion not only with a wide AVO input range but also with a relatively narrow AVO input range. In addition, the proposed joint inversion is less sensitive to the signal-to-noise ratio that other inversion methods using P-wave reflection only.

Lastly, I proposed a workflow to estimate seismic anisotropy, geomechanical properties, and total organic carbon (TOC) content of shale. In a given model test, the nonlinear Zoeppritz AVO inversion can characterize those properties of Avalon shale that are overlain by an isotropic limestone layer. The inversion accurately determines horizontal P-wave and S-wave velocities when a far angle range is applied as input data. With a near angle range, the inversion can obtain reliable vertical velocities and correct density. Consequently, seismic anisotropy can be estimated by comparison of these inverted horizontal and vertical velocities. In addition, geomechanical properties are also reliably determined in both horizontal and vertical directions. Since the inversion correctly estimates density, TOC can accurately be determined from an empirical relationship presented in the section. Furthermore, I introduced a new seismic attribute (ΔV_P) in order to more practically estimate seismic anisotropy from real seismic data. In a given field seismic test, the seismic attribute is well correlated with the values of gamma-ray (GR) log, which can assess the amount of

shale contents and should be highly correlated to seismic anisotropy. Therefore, the effectiveness of the attribute for inference of seismic anisotropy can indirectly be verified.

Based on above results, I conclude that the proposed nonlinear Zoeppritz inversion can consequently contribute toward both conventional and unconventional reservoir characterization by following: 1) providing more accurate estimations of geophysical and geomechanical properties than compared linear methods, and 2) further estimating seismic anisotropy, geomechanical properties, and TOC.

5.2 Future work

There are several possible improvements that can be implemented for the nonlinear Zoeppritz AVO inversion and its application.

First, the weight factor (i.e., w) in equation 3.4 is needed to be properly determined for enhancement of inversion results and more efficient joint inversion. In the presented inversion results, the value is set as 0.5 so that PP- and converted PS reflection can equally contribute to the inversion. However, there is a possibility that unequal contributions from the reflections may provide better results. It is, therefore, necessary to conduct a sensitivity test varying the values of the weight factor in order to determine its optimal value which can improve the proposed joint inversion. In order to provide a general understanding of the optimization, Appendix B describes the sensitivity of the nonlinear Zoeppritz AVO inversion to the P-wave and S-wave velocities, and density with three different weight factors (i.e., w: 0, 0.5, and 1).

Second, developments of advanced pre-processing techniques such as NMO-stretch correction and trim statics can improve the effectiveness of the nonlinear Zoeppritz AVO inversion. This is due to the fact that the proposed inversion still requires AVO data in far angle ranges, and the techniques can provide more stable reflection amplitudes in the ranges. Therefore, the integration of the proposed inversion and the pre-processing techniques can be a possible extension.

Although the effectiveness of the inversion for estimation of seismic anisotropy, geomechanical properties, and TOC was already demonstrated with an offshore seismic data, if another field seismic study with unconventional reservoir is possible, it can strengthen not only the superiority of

the inversion but also the feasibility of the proposed workflow and attribute. For example, seismic anisotropy inferred from the attribute was indirectly verified with a GR log in the dissertation study due to limitations of available data. Nonetheless, if measured horizontal and vertical velocities are available from ultrasonic measurements with core samples, the effectiveness of the attribute for estimation of seismic anisotropy can directly be verified. For this, to collect a full set of such data for a target reservoir has to be preceded: 1) seismic data, 2) core samples, and 3) ultrasonic measurements for vertical, horizontal, and a non-parallel (and a non-perpendicular at the same time) direction to the samples' bedding direction. The necessary data type can be extended to Rock-Eval pyrolysis for further verification of its feasibility to estimate TOC.

5.3 Discussion

Potential applications of the nonlinear Zoeppritiz inversion, the proposed workflow, and the seismic attribute, ΔV_P, include inferences of 1) fracability, 2) kerogen maturity of shale, and 3) a seismic anisotropy parameter, δ.

For the development of an unconventional reservoir, defining the fracability of target formations is important, since this information can be used for the effective hydraulic fracturing and therefore targeting landing zones of horizontal wells. The nonlinear inversion can contribute toward the understanding of rock fracability by providing an accurate estimation of geomechanical properties. Since the inversion can determine geomechanical properties not only in one isotropic direction but also in both horizontal and vertical directions unlike other inversions, brittleness and fracability of target shale can also be assessed in both directions from seismic data. However, for this application, a sound physical relationship between fracabilty and elastic geomechanical properties (i.e., Young's modulus and Poisson's ratio) has first to be established. As an example of previous attempts, Rickman et al. (2008) proposed an index, named after *brittelness index*, to evaluate rock brittleness from the elastic properties based on petrophysical observations, which indicate a correlation between higher brittleness and higher Young's modulus (and lower Poisson's ratio). Goodway et al. (2010), Guo et al. (2012), and Zorn et al. (2017) also followed Rickman et al. (2008)'s approach and introduced other seismic attributes to infer rock brittleness from elastic

properties. Nonetheless, the effectiveness to infer rock fracability from the elastic property is still arguable, since the failure of rock generally occurs in the inelastic region during its deformation process instead of the elastic region as Vernik (2016) mentioned. In addition, Vernik (2016) also pointed out that the effect of anisotropy has to be considered besides elastic-parameter-based fracability estimation assuming isotropy. Therefore, more profound studies to relate seismic anisotropy and elastic properties to fracability are needed to be preceded for a direct estimation of fracabilty from seismic data with the proposed inversion.

Regarding the objective of source rock properties characterization from seismic data, the estimation of TOC was discussed in the dissertation. Although the seismic attribute ΔV_P is developed for the estimation of seismic anisotropy, it may also be used to infer organic abundance in an unconventional shale reservoir. It is due to the fact that organic carbon content in shale is also strongly related to seismic anisotropy as discussed in the section. Besides the TOC estimation, the nonlinear AVO inversion may infer kerogen maturity of shale, which is another important constraint to guide unconventional production. Kerogen maturity indicates the degree to which source rock formation has been exposed to high heat with enough time that is needed to break down the organic matter to generate hydrocarbons. As a result, the information assesses the quality of organic shale that contains and potentially produces hydrocarbons. In addition, it is also important for the reconstruction of burial history in basin modeling, and prediction of overpressured formations. Prasad et al. (2011) and Yenugu (2014) showed examples of how kerogen maturity can be characterized by seismic properties such as P-wave and S-wave velocities, density, and impedance. Since the nonlinear Zoeppritiz inversion can independently estimate the seismic parameters, assessment of maturity from seismic data may be possible with the method. For this, establishing and exploiting correlations between seismic properties, microstructure, and kerogen content of shale has to be investigated.

The last potential application of the nonlinear Zoeppritiz inversion is the estimation of δ, one of *Thomsen parameters* (ϵ, γ, and δ) to indicate anisotropy level. Of the three parameters, δ is one of the most important parameters, since it controls the normal-moveout (NMO) behavior of

a VTI medium like shale (Yan et al., 2013). Although estimations of seismic anisotropy for ϵ and γ are only demonstrated in the dissertation, seismic anisotropy δ may also further be inferred with the proposed workflow (in section 4) by varying input AVO angle ranges. When the δ value and correct model Poisson's ratio are respectively set as unknown and known, the nonlinear AVO inversion is now changed to another type of inverse problem to estimate correct δ value. Once an accurate estimation of δ is possible with the inversion, it can contribute to accurate velocity modeling by providing better NMO velocities for VTI media. Consequently, it may enhance the accuracy of other seismic data processing techniques such as NMO correction, migration, full waveform inversion (FWI), and etc.

REFERENCES

Aki, K., and P. G. Richards, 1980, Quantitative seismology: University Science Books.

Altowairqi, Y., R. Rezaee, B. Evans, and M. Urosevic, 2017, A quantitative application of seismic inversion and multi-attribute analysis based on rock physics linear relationships to identify high total organic carbon shale-a case study from the perth basin, western australia.

Auld, B. A., 1973, Acoustic fields and waves in solids: Ripol Classic.

Backus, G. E., 1962, Long-wave elastic anisotropy produced by horizontal layering: Journal of Geophysical Research, **67**, 4427–4440.

Banik, N. C., M. S. Egan, et al., 2012, Effects of vti anisotropy on shale reservoir characterization: Presented at the SPE Middle East Unconventional Gas Conference and Exhibition, Society of Petroleum Engineers.

Behura, J., N. Kabir, R. Crider, P. Jilek, and E. Lake, 2010, Density extraction from p-wave avo inversion: Tuscaloosa trend example: The Leading Edge, **29**, 772–777.

Birch, F., 1961, The velocity of compressional waves in rocks to 10 kilobars: Part 2.: Journal of Geophysical Research, **66**, 2199–2224.

Bork, J., C. Yin, J. Castagna, H. Karazincir, L. Wood, and R. Schneider, 1997, An investigation into unusual avo signatures in the gulf of mexico and trinidad, *in* SEG Technical Program Expanded Abstracts 1997: Society of Exploration Geophysicists, 199–201.

Bortfeld, R., 1961, Approximations to the reflection and transmission coefficients of plane longitudinal and transverse waves: Geophysical Prospecting, **9**, 485–502.

Burger, J., and G. Chavent, 1979, Identification de param tres r partis dans les quations aux d riv es partielles: RAIRO, **13**, 115–126.

Carcione, J. M., 2001, AVO effects of a hydrocarbon source-rock layer: Geophysics, **66**, 419–427.

Carcione, J. M., H. B. Helle, and P. Avseth, 2011, Source-rock seismic-velocity models: Gassmann versus backus: Geophysics, **76**, N37–N45.

Carmichael, R. S., 1988, Practical handbook of physical properties of rocks and minerals: CRC

press.

Castagna, J. P., and M. Backus, 1993, AVO analysis—tutorial and review: Offset-dependent reflectivity: Theory and practice of AVO analysis: SEG Investigations in Geophysics, 3–36.

Castagna, J. P., and H. W. Swan, 1997, Principles of avo crossplotting: The leading edge, **16**, 337–344.

Castagna, J. P., H. W. Swan, and D. J. Foster, 1998, Framework for avo gradient and intercept interpretation: Geophysics, **63**, 948–956.

Castañeda, P. P., and J. R. Willis, 1995, The effect of spatial distribution on the effective behavior of composite materials and cracked media: Journal of the Mechanics and Physics of Solids, **43**, 1919–1951.

Chopra, S., R. K. Sharma, and K. J. Marfurt, 2013, Current workflows for shale gas reservoir characterization: Unconventional Resources Technology Conference (URTEC).

Connolly, P., 1999, Elastic impedance: The leading edge, **18**, 438–452.

Dębski, W., and A. Tarantola, 1995, Information on elastic parameters obtained from the amplitudes of reflected waves: Geophysics, **60**, 1426–1436.

Durand, B., and J. Espitalie, 1976, Geochemical studies on the organic matter from the douala basin (cameroon)—ii. evolution of kerogen: Geochimica et Cosmochimica Acta, **40**, 801–808.

Durand, B., A. Huc, and J. Oudin, 1987, Oil saturation and primary migration: observations in shales and coals from the kerbau wells, mahakam delta, indonesia: Collection colloques et séminaires-Institut français du pétrole, 173–195.

Espitalié, J., J. L. Laporte, M. Madec, F. Marquis, P. Leplat, J. Paulet, and A. Boutefeu, 1977, Méthode rapide de caractérisation des roches mètres, de leur potentiel pétrolier et de leur degré d'évolution: Revue de l'Institut français du Pétrole, **32**, 23–42.

Fatti, J. L., G. C. Smith, P. J. Vail, P. J. Strauss, and P. R. Levitt, 1994, Detection of gas in sandstone reservoirs using AVO analysis: A 3-D seismic case history using the Geostack technique: Geophysics, **59**, 1362–1376.

Gardner, G., and D. Forel, 1987, Connections between rock properties and seismic data, *in* Re-

fresher course in geophysics: University of Houston, Allied Geophysical Laboratories.

Gibson, R. L., A. G. Sena, and M. Toksöz, 1991, Paraxial ray tracing in 3d inhomogeneous, anisotropic media: Geophysical prospecting, **39**, 473–504.

Goodway, B., T. Chen, and J. Downton, 1997, Improved avo fluid detection and lithology discrimination using lamé petrophysical parameters;"$\lambda\rho$","$\mu\rho$", & "λ/μ fluid stack", from p and s inversions, *in* SEG Technical Program Expanded Abstracts 1997: Society of Exploration Geophysicists, 183–186.

Goodway, B., M. Perez, J. Varsek, and C. Abaco, 2010, Seismic petrophysics and isotropic-anisotropic avo methods for unconventional gas exploration: The Leading Edge, **29**, 1500–1508.

Guo, Z., M. Chapman, and X. Li, 2012, A shale rock physics model and its application in the prediction of brittleness index, mineralogy, and porosity of the barnett shale, *in* SEG technical program expanded abstracts 2012: Society of Exploration Geophysicists, 1–5.

Hampson, D., and B. Russell, 2013, Joint simultaneous inversion of pp and ps angle gathers: Canadian Society of Exploration Geophysicists Recorder, **33**, 32–39.

Hampson, D. P., B. H. Russell, and B. Bankhead, 2005, Simultaneous inversion of pre-stack seismic data, *in* SEG Technical Program Expanded Abstracts 2005: Society of Exploration Geophysicists, 1633–1637.

Harbor, R. L., 2011, Facies characterization and stratigraphic architecture of organic-rich mudrocks, upper cretaceous eagle ford formation, south texas.

Hilterman, F. J., 2001, Seismic amplitude interpretation: Society of Exploration Geophysicists and European Association of Geoscientists and Engineers.

Hornby, B. E., 1998, Experimental laboratory determination of the dynamic elastic properties of wet, drained shales: Journal of Geophysical Research: Solid Earth, **103**, 29945–29964.

Huc, A.-Y., 2013, Geochemistry of fossil fuels: from conventional to unconventional hydrocarbon systems: Editions Technip.

Jarvie, D. M., R. J. Hill, T. E. Ruble, and R. M. Pollastro, 2007, Unconventional shale-gas systems: The mississippian barnett shale of north-central texas as one model for thermogenic shale-gas

assessment: AAPG bulletin, **91**, 475–499.

Johnston, J. E., and N. I. Christensen, 1995, Seismic anisotropy of shales: Journal of Geophysical Research: Solid Earth, **100**, 5991–6003.

Kabir, N., R. Crider, and G. Xia, 2005, Can hydrocarbon saturation be estimated using density contrast parameter?, *in* SEG Technical Program Expanded Abstracts 2005: Society of Exploration Geophysicists, 214–217.

King, M. S., 1964, Wave velocities and dynamic elastic moduli of sedimentary rocks: PhD thesis, University of California, Berkeley.

Kurt, H., 2007, Joint inversion of ava data for elastic parameters by bootstrapping: Computers & Geosciences, **33**, 367–382.

Lavaud, B., N. Kabir, and G. Chavent, 1999, Pushing avo inversion beyond linearized approximation: Journal of Seismic Exploration, **8**, 279–302.

Lim, U. Y., 2014, Investigation of and correction for waveform changes arising from nmo stretch: Master's thesis, University of Houston.

Lim, U. Y., R. Gibson, N. Kabir, and D. Zhu, 2017, Inference of geomechanical properties of shales from avo inversion based on the zoeppritz equations, *in* SEG Technical Program Expanded Abstracts 2017: Society of Exploration Geophysicists, 728–732.

Lim, U. Y., N. Kabir, and R. L. Gibson Jr, 2018, Horizontal-velocity estimation from pp-and ps-joint avo inversion based on zoeppritz equations: Eagle ford case study, *in* SEG Technical Program Expanded Abstracts 2018: Society of Exploration Geophysicists, 2422–2426.

Lo, T.-w., K. B. Coyner, and M. N. Toksöz, 1986, Experimental determination of elastic anisotropy of berea sandstone, chicopee shale, and chelmsford granite: Geophysics, **51**, 164–171.

Løseth, H., L. Wensaas, M. Gading, K. Duffaut, and M. Springer, 2011, Can hydrocarbon source rocks be identified on seismic data?: Geology, **39**, 1167–1170.

Margrave, G. F., R. R. Stewart, and J. A. Larsen, 2001, Joint pp and ps seismic inversion: The Leading Edge, **20**, 1048–1052.

Mesdag, P., 2016, A new approach to quantitative azimuthal inversion for stress and fracture detec-

tion, *in* SEG Technical Program Expanded Abstracts 2016: Society of Exploration Geophysicists, 357–361.

Nye, J. F., 1985, Physical properties of crystals: their representation by tensors and matrices: Oxford university press.

Ostrander, W., 1984, Plane-wave reflection coefficients for gas sands at nonnormal angles of incidence: Geophysics, **49**, 1637–1648.

Passey, Q., S. Creaney, J. Kulla, F. Moretti, and J. Stroud, 1990, A practical model for organic richness from porosity and resistivity logs: AAPG bulletin, **74**, 1777–1794.

Payne, S. S., and J. Meyer, 2017, Using seismic inversion to predict geomechanical well behavior: a case study from the permian basin.

Pearson, K., 1895, Notes on regression and inheritance in the case of two parents proceedings of the royal society of london, 58, 240-242.

Peselnick, L., and R. A. Robie, 1963, Elastic constants of calcite: Journal of Applied Physics, **34**, 2494–2495.

Prasad, M., K. C. Mba, T. Sadler, M. L. Batzle, et al., 2011, Maturity and impedance analysis of organic-rich shales: SPE Reservoir Evaluation & Engineering, **14**, 533–543.

Price, L. C., 1983, Geologic time as a parameter in organic metamorphism and vitrinite reflectance as an absolute paleogeothermometer: Journal of Petroleum Geology, **6**, 5–37.

Rickman, R., M. J. Mullen, J. E. Petre, W. V. Grieser, and D. Kundert, 2008, A practical use of shale petrophysics for stimulation design optimization: All shale plays are not clones of the barnett shale, *in* SPE Annual Technical Conference and Exhibition: Society of Petroleum Engineers.

Ross, C., 1995, Improved mature field development with 3d/avo technology: First Break, **13**, 139–145.

Rüger, A., 1997, P-wave reflection coefficients for transversely isotropic models with vertical and horizontal axis of symmetry: Geophysics, **62**, 713–722.

Russell, B. H., 1988, Introduction to seismic inversion methods: Society of Exploration Geophysicists.

Rutherford, S. R., and R. H. Williams, 1989, Amplitude-versus-offset variations in gas sands: Geophysics, **54**, 680–688.

Sayers, C. M., 2013, The effect of kerogen on the avo response of organic-rich shales: The Leading Edge, **32**, 1514–1519.

Sayers, C. M., S. Guo, and J. Silva, 2015, Sensitivity of the elastic anisotropy and seismic reflection amplitude of the eagle ford shale to the presence of kerogen: Geophysical Prospecting, **63**, 151–165.

Schmoker, J. W., 1979, Determination of organic content of appalachian devonian shales from formation-density logs: Geologic notes: AAPG Bulletin, **63**, 1504–1509.

Shuey, R., 1985, A simplification of the zoeppritz equations: Geophysics, **50**, 609–614.

Smith, G., and P. Gidlow, 1987, Weighted stacking for rock property estimation and detection of gas: Geophysical Prospecting, **35**, 993–1014.

Sondergeld, C. H., C. S. Rai, R. W. Whidden, et al., 2000, Ultrasonic measurement of anisotropy on the kimmeridge shale: GEOPHYSICS.

Sondhi, N., 2011, Petrophysical characterization of eagle ford shale: Master's thesis, University of Oklahoma.

Sone, H., 2012, Mechanical properties of shale gas reservoir rocks, and its relation to the in-situ stress variation observed in shale gas reservoirs: PhD thesis, Stanford University.

Thomsen, L., 1986, Weak elastic anisotropy: Geophysics, **51**, 1954–1966.

———, 2014, Understanding seismic anisotropy in exploration and exploitation: Society of Exploration Geophysicists.

Tosaya, C. A., 1983, Acoustical properties of clay-bearing rocks.: PhD thesis, Stanford University.

Ursenbach, C. P., 2002, Optimal zoeppritz approximations, *in* SEG Technical Program Expanded Abstracts 2002: Society of Exploration Geophysicists, 1897–1900.

Ursin, B., and T. Dahl, 1992, Seismic reflection amplitudes: Geophysical Prospecting, **40**, 483–512.

Vanorio, T., M. Prasad, and A. Nur, 2003, Elastic properties of dry clay mineral aggregates, sus-

pensions and sandstones: Geophysical Journal International, **155**, 319–326.

Verm, R., and F. Hilterman, 1995, Lithology color-coded seismic sections: The calibration of avo crossplotting to rock properties: The Leading Edge, **14**, 847–853.

Vernik, L., 2016, Seismic petrophysics in quantitative interpretation: Society of Exploration Geophysicists.

Vernik, L., and C. Landis, 1996, Elastic anisotropy of source rocks: Implications for hydrocarbon generation and primary migration: AAPG bulletin, **80**, 531–544.

Vernik, L., and X. Liu, 1997, Velocity anisotropy in shales: A petrophysical study: GEOPHYSICS, **62**, 521–532.

Vernik, L., and A. Nur, 1992, Ultrasonic velocity and anisotropy of hydrocarbon source rocks: GEOPHYSICS, **57**, 727–735.

Wang, Y., 1999, Approximations to the zoeppritz equations and their use in avo analysis: Geophysics, **64**, 1920–1927.

Wiggins, R., G. Kenny, and C. McClure, 1983, A method for determining and displaying the shear-velocity reflectivities of a geologic formation.

Willis, J., 1977, Bounds and self-consistent estimates for the overall properties of anisotropic composites: Journal of the Mechanics and Physics of Solids, **25**, 185–202.

———, 1978, Variational principles and bounds for the overall properties of composites: Continuum models for discrete systems, 185–215.

Yan, F., D.-h. Han, and Q. Yao, 2013, Physical constraints on c13 and thomsen parameter delta for vti rocks, *in* SEG Technical Program Expanded Abstracts 2013: Society of Exploration Geophysicists, 2889–2894.

Yenugu, M. R., 2014, Elastic, microstructural and geochemical characterization of kerogen maturity for shales: PhD thesis, University of Houston.

Yoo, S., and R. L. Gibson Jr, 2005, Frequency dependent avo analysis after target oriented stretch correction, *in* SEG Technical Program Expanded Abstracts 2005: Society of Exploration Geophysicists, 293–296.

Zhi, L., S. Chen, and X.-y. Li, 2013, Joint avo inversion of pp and ps waves using exact zoeppritz equation, *in* SEG Technical Program Expanded Abstracts 2013: Society of Exploration Geophysicists, 457–461.

———, 2016, Amplitude variation with angle inversion using the exact zoeppritz equations—theory and methodology: Geophysics, **81**, N1–N15.

Zhu, X., and G. McMechan, 2012, Avo inversion using the zoeppritz equation for pp reflections, *in* SEG Technical Program Expanded Abstracts 2012: Society of Exploration Geophysicists, 1–5.

Zoeppritz, K., 1919, On the reflection and penetration of seismic waves through unstable layers: Göttinger Nachrichten, I, 66–84.

Zong, Z., X. Yin, and G. Wu, 2013, Elastic impedance parameterization and inversion with young's modulus and poisson's ratioei with young and poisson: Geophysics, **78**, N35–N42.

Zorn, E., R. Hammack, W. Harbert, and A. Kumar, 2017, Geomechanical lithology-based analysis of microseismicity in organic shale sequences: A pennsylvania marcellus shale example: The Leading Edge, **36**, 845–851.

APPENDIX A

DERIVATION OF THE GRADIENT OF R_{PS} (∇R_{PS})

This appendix is devoted to the resolution of the derivation of the gradient of R_{PS} (i.e., ∇R_{PS}). I compute here the derivatives of the forward map $\varphi : x \rightsquigarrow v$ (equation 3.10) described in section 3: the parameter vector $x \in \mathbb{R}^4$ is made of the dimensionless three contrast and one background parameters (e_p, e_s, e_d, χ) across the elastic interface, and the output vector $v \in \mathbb{R}^{N_{obs}}$ is made of the N_{obs} reflection coefficients $R_1, \ldots, R_{N_{obs}}$ computed by the sequence of equations 3.3 (first) and 3.2 (last) for the N_{obs} different incidence angles $\theta_1, \ldots, \theta_{N_{obs}}$. I illustrate this procedure by applying the adjoint state technique (Burger and Chavent, 1979) introduced in sections 2.3.3 and 3.2.3 step-by-step.

A.1 Forward Map and Objective Function

Because of the independence of the calculations performed for each angle of incidence, I only need to compute the derivative of the forward map $\varphi : x \in \mathbb{R}^4 \rightsquigarrow v = R_{PS} \in \mathbb{R}$ for one given incidence angle θ. Hence the forward map here is $\varphi : x \rightsquigarrow R_{PS}$, and the objective function is R_{PS}. I equip both parameter space $\mathbb{R}^4$ and output space $\mathbb{R}$ with the usual Euclidean scalar products so that the Jacobian φ' of φ and its gradient $\nabla\varphi$ is transposed matrices for the chosen scalar products.

A.2 State-Space Decomposition

I use here the decomposition suggested in equation 3.11:

$$\begin{aligned} y &= (e, f, S_1, S_2, \ldots, P, Q, R_{PS}) \in \mathbb{R}^{19} \qquad \text{(state vector)} \\ M &= [0, \ldots, 01] \qquad\qquad\qquad \text{(observation operator)}, \end{aligned} \tag{A.1}$$

which has to be complemented by the state equation $e(x, y) = 0$. This requires to rewrite the set of equations 3.2 and 3.3 in the form of a sequence of equations. If I want to avoid the need to

differentiate square roots or quotients, I can choose for $e(x, y) = 0$:

$$
\begin{aligned}
& e - e_s - e_d = 0 \\
& f - 1 + e_d^2 = 0 \\
& S_1 - \chi(1 + e_p) = 0 \\
& S_2 - \chi(1 - e_p) = 0 \\
& (1 - e_s)T_1 - 2 = 0 \\
& (1 + e_s)T_2 - 2 = 0 \\
& q^2 - S_1 \sin^2 \theta = 0 \\
& M_1^2 - S_1 + q^2 = 0 \qquad (M_1 \geq 0) \\
& M_2^2 - S_2 + q^2 = 0 \qquad (M_2 \geq 0) \\
& N_1^2 - T_1 + q^2 = 0 \qquad (N_1 \geq 0) \\
& N_2^2 - T_2 + q^2 = 0 \qquad (N_2 \geq 0) \\
& D - eq^2 = 0 \\
& A - e_d + D = 0 \\
& K - D + A = 0 \\
& B - 1 + K = 0 \\
& C - 1 - K = 0 \\
& Q - M_2(C^2 N_2 + f N_1) - 4q^2 A^2 = 0 \\
& P - M_1(B^2 N_1 + f N_2) - 4eDM_1 M_2 N_1 N_2 = 0 \\
& (P + Q)S_1 R_{PS} + 4qM_1 T_1(AB + eCM_2 N_2) = 0
\end{aligned}
\tag{A.2}
$$

When the chosen equations have more than one solution, the condition in parenthesis indicates which one is to be chosen. As expected, there are 19 equations for 19 state unknowns. In this context, the solution of the (direct) state equation, y, is called the (direct) state.

A.3 Lagrangian

With the objective function R_{PS} and the state-space decomposition in equation A.2, the Lagrangian reads

$$
\begin{aligned}
\mathcal{L}(x, y, \omega) =& R_{PS} + \omega_1(e - e_s - e_d) \\
&+ \omega_2(f - 1 + e_d^2) \\
&+ \omega_3(S_1 - \chi(1 + e_p)) \\
&+ \omega_4(S_2 - \chi(1 - e_p)) \\
&+ \omega_5((1 - e_s)T_1 - 2) \\
&+ \omega_6((1 + e_s)T_2 - 2) \\
&+ \omega_7(q^2 - S_1 \sin^2\theta) \\
&+ \omega_8(M_1^2 - S_1 + q^2) \\
&+ \omega_9(M_2^2 - S_2 + q^2) \\
&+ \omega_{10}(N_1^2 - T_1 + q^2) \\
&+ \omega_{11}(N_2^2 - T_2 + q^2) \\
&+ \omega_{12}(D - eq^2) \\
&+ \omega_{13}(A - e_d + D) \\
&+ \omega_{14}(K - D + A) \\
&+ \omega_{15}(B - 1 + K) \\
&+ \omega_{16}(C - 1 - K) \\
&+ \omega_{17}(Q - M_2(C^2 N_2 + f N_1) - 4q^2 A^2) \\
&+ \omega_{18}(P - M_1(B^2 N_1 + f N_2) - 4eDM_1M_2N_1N_2) \\
&+ \omega_{19}((P + Q)S_1 R_{PS} + 4qM_1T_1(AB + eCM_2N_2))
\end{aligned}
\tag{A.3}
$$

The equation A.3 can be briefly expressed as formulated in equation 3.12. ω is defined as the solution of following adjoint state equation:

$$\frac{\partial \mathcal{L}}{\partial y}(x, y, \omega)\delta y = 0 \quad \text{for any } \delta y \in \mathbb{R}^{19} \tag{A.4}$$

In this context, ω is called the adjoint state.

For further discussions, it is useful to summarize the arguments of the Lagrangian and the spaces where they belong at this point as follows:

$$\begin{aligned} x &= (e_p, e_s, e_d, \chi) \in \mathbb{R}^4 && \text{(model vector)} \\ y &= (e, f, S_1, S_2, \ldots, P, Q, R_{PS}) \in \mathbb{R}^{19} && \text{(direct state vector)} \\ \omega &= (\omega_1, \ldots, \omega_1 9) \in \mathbb{R}^{19} && \text{(adjoint state vector)} \end{aligned} \tag{A.5}$$

Note that the direct and adjoint state vectors have the same dimension. In addition, the vectors, x, y, and ω contain all the necessary information to compute the Lagrangian, $\mathcal{L}$, as an explicit function. Here, the only quantity that appears in the right-hand side of equation A.3 is not in the arguments of $\mathcal{L}$. Instead, it is in the angle of incidence, θ, which is known.

A.4 Adjoint Equation

The variational form of the adjoint equation in equation A.4 is obtained by differentiating the 20 terms of the Lagrangian (equation A.3) with respect to the state variables only and equating the result to zero. Following shows the form:

$$
\begin{aligned}
\frac{\partial \mathcal{L}}{\partial y}(x,y,\omega)\delta y =& \delta R_{PS} + \omega_1\delta e + \omega_2\delta f + \omega_3\delta S_1 + \omega_4\delta S_2 \\
&+ \omega_5(1-e_s)\delta T_1 + \omega_6(1+e_s)\delta T_2 \\
&+ \omega_7(\delta(q^2) - \delta S_1 \sin^2\theta) + \omega_8(2M_1\delta M_1 - \delta S_1 + \delta(q^2)) \\
&+ \omega_9(2M_2\delta M_2 - \delta S_2 + \delta(q^2)) + \omega_{10}(2N_1\delta N_1 + \delta(q^2) - \delta T_1) \\
&+ \omega_{11}(2N_2\delta N_2 + \delta(q^2) - \delta T_2) + \omega_{12}(\delta D - q^2\delta e - e\delta(q^2)) \\
&+ \omega_{13}(\delta A + \delta D) + \omega_{14}(\delta A - \delta D + \delta K) \\
&+ \omega_{15}(\delta B + \delta K) + \omega_{16}(\delta C - \delta K) \\
&+ \omega_{17}(-4eM_1M_2N_1N_2\delta D - 4DM_1M_2N_1N_2\delta e - 4DeM_2N_1N_2\delta M_1 \\
&\quad - \delta M_1(B^2N_1 + fN_2) - 4DeM_1N_1N_2\delta M_2 \\
&\quad - 4DeM_1M_2N_2\delta N_1 - 4DeM_1M_2N_1\delta N_2 \\
&\quad - M_1(2BN_1\delta B + N_2\delta f + B^2\delta N_1 + f\delta N_2) + \delta P) \\
&+ \omega_{18}(-8Aq^2\delta A - (fN_1 + C^2N_2)\delta M_2 \\
&\quad - M_2(2CN_2\delta C + N_1\delta f + f\delta N_1 + C^2\delta N_2) \\
&\quad - 4A^2\delta(q^2) + \delta Q) \\
&+ \omega_{19}(4(AB + CeM_2N_2)\sqrt{q^2}\sqrt{\frac{T_1}{S_1}}\delta M_1 \\
&\quad + 4M_1\sqrt{q^2}\sqrt{\frac{T_1}{S_1}}(B\delta A + A\delta B + eM_2N_2\delta C \\
&\qquad + CM_2N_2\delta e + CeN_2\delta M_2 + CeM_2\delta N_2) \\
&\quad + \frac{2M_1(AB + CeM_2N_2)\sqrt{\frac{T_1}{S_1}}\delta(q^2)}{\sqrt{(q^2)}} \\
&\quad + R_{PS}(\delta P + \delta Q) + (P+Q)\delta R_{PS} \\
&\quad + \frac{2M_1(AB + CeM_2N_2)\sqrt{q^2}(-\frac{T_1\delta S_1}{S_1^2} + \delta T_1/S_1)}{\sqrt{\frac{T_1}{S_1}}})
\end{aligned}
\tag{A.6}
$$

The computational form of the adjoint equations is obtained by equating to zero the coefficient of δe, δf, δS_1, δS_2, ..., δP, δQ, and δR_{PS} in equation A.6. Following equations are the adjoint state equations for exact PS-reflection (equation 3.2), which can be solved easily backwards, computing first ω_{19}, then ω_{18}, ..., ω_1 sequentially:

$$
\begin{aligned}
0 =&\ \omega_1 - q^2\omega_{12} - 4DM_1M_2N_1N_2\omega_{17} + 4CM_1M_2N_2q\sqrt{\frac{T1}{S1}}\omega_{19} \\
0 =&\ \omega_2 - M_1N_2\omega_{17} - M_2N_1\omega_{18} \\
0 =&\ \omega_3 - \omega_8 - \omega_7\sin^2\theta - \frac{2M_1(AB + CeM_2N_2)qT_1\omega_{19}}{S_1^2\sqrt{\frac{T1}{S1}}} \\
0 =&\ \omega_4 - \omega_9 \\
0 =&\ (1-e_s)\omega_5 - \omega_{10} + \frac{2M_1(AB + CeM_2N_2)q\omega_{19}}{S_1\sqrt{\frac{T1}{S1}}} \\
0 =&\ (1+e_s)\omega_6 - \omega_{11} \\
0 =&\ \omega_7 + \omega_8 + \omega_9 + \omega_{10} + \omega_{11} - e\omega_{12} - 4A^2\omega_{18} + \frac{2M_1(AB + CeM_2N_2)\sqrt{\frac{T1}{S1}}\omega_{19}}{q} \\
0 =&\ 2M_1\omega_8 - (B^2N_1 + fN_2 + 4DeM_2N_1N_2)\omega_{17} + 4(AB + CeM_2N_2)q\sqrt{\frac{T1}{S1}}\omega_{19} \\
0 =&\ 2M_2\omega_9 - 4DeM_1N_1N_2\omega_{17} - (fN_1 + C^2N_2)\omega_{18} + 4CeM_1N_2q\sqrt{\frac{T1}{S1}}\omega_{19} \\
0 =&\ 2N_1\omega_{10} - (B^2M_1 + 4DeM_1M_2N_2)\omega_{17} - fM_2\omega_{18} \\
0 =&\ 2N_2\omega_{11} - (fM_1 + 4DeM_1M_2N_1)\omega_{17} - C^2M_2\omega_{18} + 4CeM_1M_2q\sqrt{\frac{T1}{S1}}\omega_{19} \\
0 =&\ \omega_{12} + \omega_{13} - \omega_{14} - 4eM_1M_2N_1N_2\omega_{17} \\
0 =&\ \omega_{13} + \omega_{14} - 8Aq^2\omega_{18} + 4BM_1q\sqrt{\frac{T1}{S1}}\omega_{19} \\
0 =&\ \omega_{14} + \omega_{15} - \omega_{16} \\
0 =&\ \omega_{15} - 2BM_1N_1\omega_{17} + 4AM_1q\sqrt{\frac{T1}{S1}}\omega_{19} \\
0 =&\ \omega_{16} - 2CM_2N_2\omega_{18} + 4eM_1M_2N_2q\sqrt{\frac{T1}{S1}}\omega_{19} \\
0 =&\ \omega_{17} + R_{PS}\omega_{19} \\
0 =&\ \omega_{18} + R_{PS}\omega_{19} \\
0 =&\ 1 + (P+Q)\omega_{19}
\end{aligned}
\tag{A.7}
$$

A.5 Gradient Equation

Differentiation of the Lagrangian (equation A.3) with respect to its first argument (i.e., model vector), $x = (e_p, e_s, e_d, \chi)$, gives

$$\begin{aligned}\frac{\partial \mathcal{L}}{\partial x}(x, y, \omega) = &- \omega_1(\delta e_s + \delta e_d) \\ &+ \omega_2 2 e_d \delta e_d \\ &- \omega_3(\delta\chi(1 + e_p) + \chi(\delta e_p)) \\ &- \omega_4(\delta\chi(1 - e_p) - \chi(\delta e_p)) \\ &- \omega_5 \delta e_s T_1 \\ &+ \omega_6 \delta e_s T_2 \\ &- \omega_{13} \delta e_d \end{aligned} \tag{A.8}$$

Since for any $\delta x \in \mathbb{R}^n$,

$$\frac{\partial R_{PS}}{\partial \chi}\delta\chi + \frac{\partial R_{PS}}{\partial e_p}\delta e_p + \frac{\partial R_{PS}}{\partial e_s}\delta e_s + \frac{\partial R_{PS}}{\partial e_d}\delta e_d = \frac{\partial \mathcal{L}}{\partial x}(x, y_x, \omega_x) \tag{A.9}$$

comparing equations A.8 and A.9 finally gives the gradient of R_{PS} with respect to the model vector $x = (e_p, e_s, e_d, \chi)$ (i.e., $\nabla_x R_{PS}$) as following:

$$\begin{aligned}\frac{\partial R_{PS}}{\partial \chi} &= -(1 + e_p)\omega_3 - (1 - e_p)\omega_4 \\ \frac{\partial R_{PS}}{\partial e_p} &= \chi\omega_4 - \chi\omega_3 \\ \frac{\partial R_{PS}}{\partial e_s} &= -\omega_1 - \omega_5 T_1 + \omega_6 T_2 \\ \frac{\partial R_{PS}}{\partial e_d} &= -\omega_1 + 2 e_d \omega_2 - \omega_3 \end{aligned} \tag{A.10}$$

Substituting corresponding values in equation 3.3 for T_1 and T_2 in equation A.10 gives the final form of the gradient of R_{PS} as in equation 3.17.

APPENDIX B

SENSITIVITY OF THE NONLINEAR ZOEPPRITZ AVO INVERSION TO THE P-WAVE AND S-WAVE VELOCITIES AND DENSITY

In the appendix, I will examine the sensitivity of the nonlinear Zoeppritz AVO inversion to the target parameters (i.e., P-wave and S-wave velocities, and density). The sensitivity is also investigated with the different types of AVO input: PP- and PS-reflection coefficients (R_{PP} and R_{PS}). For the test, the Eagle Ford model presented in section 3 is selected. With the model values in Table 3.1, input AVO data (i.e., exact anisotropic PP- and PS-reflection coefficients) are generated by a paraxial ray tracing (Gibson et al., 1991) (Figure 3.1). The proposed nonlinear Zoeppritz inversion is applied to the data. I first compute the L^2-norm described in equation 3.4 as illustrated in Figures B.1, B.2, B.3, B.4, B.5, and B.6. For the computations depicted in each subfigure, I vary two parameters with one fixed parameter. When one target parameter is fixed, exact model values are applied for the other two (for example, Figure B.1(a) illustrates the situation where variable values of P-wave velocity and density are applied, and the value of S-wave is fixed as the true model value.). Ranges of variation of each parameters are set as

- from 4 (km/s) to 5 (km/s) with the 0.1 (km/s) increment for P-wave velocity (V_P)
- from 2 (km/s) to 3 (km/s) with the 0.1 (km/s) increment for S-wave velocity (V_S)
- from 2 (g/cc) to 3 (g/cc) with the 0.1 (g/cc) increment for density (ρ)

Then, I consider the following different situations based on

- the AVO input ranges
  - $0^\circ \sim 60^\circ$ (Figures B.1, B.2, and B.3)
  - $0^\circ \sim 20^\circ$ (Figures B.4, B.5, and B.6)
- the data used for inversion

  - R_{PP} only: the case that ω in equation 3.4 is set as 1 (Figures B.1 and B.4)
  - R_{PS} only: the case that ω in equation 3.4 is set as 0 (Figures B.2 and B.5)
  - $R_{PP} + R_{PS}$ together: the case that ω in equation 3.4 is set as 0.5 (Figures B.3 and B.6)

- the level of organic abundance determined in kerogen volume fraction (i.e., the controlling factor of seismic anisotropy)
  - 0 (Kerogen (v/v)) (first row of Figures B.1, B.2, B.3, B.4, B.5, and B.6)
  - 0.04 (Kerogen (v/v)) (second row of Figures B.1, B.2, B.3, B.4, B.5, and B.6)
  - 0.08 (Kerogen (v/v)) (third row of Figures B.1, B.2, B.3, B.4, B.5, and B.6)

- the combinations of parameters varied for the computation of L^2-norm
  - V_P and ρ (first column of Figures B.1, B.2, B.3, B.4, B.5, and B.6)
  - V_S and ρ (second column of Figures B.1, B.2, B.3, B.4, B.5, and B.6)
  - V_P and V_S (third column of Figures B.1, B.2, B.3, B.4, B.5, and B.6)

When the AVO input and its range are set as R_{PP} and $0^\circ \sim 60^\circ$, the ambiguity of the location of the minimum of the L^2-norm is minimized (Figure B.1) compared to other situations described in Figures B.2, B.4, and B.5. For most of the cases in Figure B.1, the proposed nonlinear AVO inversion results (red circles) are well matched to the minima of the errors except the case depicted in Figure B.1(c). The exception is evidence that density contributes to the result of AVO inversion relatively more than the other two parameters when R_{PP} is applied as input. Therefore, displays of the norm as a function of V_P and V_S shows a broader minimum than for the other two combinations of parameters that address density (i.e., compare the third column of Figure B.1 to the first two columns). On the other hand, the uncertainty of the location of the minimum significantly increases when R_{PS} is only considered as input with the same AVO range, $0^\circ \sim 60^\circ$, for all possible combinations (Figure B.2). The first and third columns in Figure B.2 also show that density and V_S affect PS AVO inversion more than V_P. In addition, the PS AVO inversion values (red circles in

Figure B.2) have relatively more deviated from the minimum error (the purple colored area) than the PP AVO inversion results (red circles in Figure B.1). The above observations indicate that R_{PP} conveys more information on V_P than R_{PS}. Consequently, the nonlinear Zoeppritz AVO inversion can provide more accurate estimates for the target parameters when R_{PP} is applied instead of R_{PS} with far angle range.

However, when the relatively near angle range (i.e., $0^\circ \sim 20^\circ$) is utilized for the inversion, the ambiguity from the both PP- and PS-AVO inversions to define the minimum L^2-norm dramatically increase (Figures B.4 and B.5). Therefore, the AVO inversion cannot properly differentiate the target parameters, which are coupled with each other, in many cases. It also implies the importance of accurate initial estimates of parameters before inversion. In particular, Figure B.4 illustrates that the sensitivity values of the AVO inversion to the parameters, when R_{PP} is the only input data, follow the ordering $\rho > V_P > V_S$. In addition, it also shows the strong coupling between density and V_S (second column of Figure B.4) in the case. On the other hand, it is repeatedly shown that density (mostly) and V_P more influences on the L^2-norm than V_S, when R_{PS} is only considered (Figure B.5). In this case, the strong coupling between density and V_S is still observed in the second column of Figure B.5.

In order to show the effectiveness of the joint inversion approach presented in section 3, the inversion results utilizing both R_{PP} and R_{PS} with equal weight are indicated with yellow circles in Figures B.3 and B.6. The yellow circles are also plotted in Figures B.1, B.2, B.4, and B.5 for comparisons. In these cases, ω in equation 3.4 is set as 0.5. Figure B.3 shows the distribution of L^2-norm between modeled and observed AVOs, when the relatively far AVO angle range is applied (i.e., $0^\circ \sim 60^\circ$). On the other hand, Figure B.6 describes the results with the near angle range, $0^\circ \sim 20^\circ$. As shown in both cases, the distributions of L^2-norm are more concave compared to the cases either R_{PP} or R_{PS} is applied only. Therefore, the joint inversion can more efficiently overcome the strong nonlinearity of the inverse problem by utilizing additional PS-AVO information as well as more typical PP-AVO.

In conclusion, the sensitivity of the nonlinear Zoeppritz AVO inversion to the P-wave and S-

wave velocities, and density depends on the applied AVO ranges. When a far angle range is applied, density and V_S controls the sensitivity of the nonlinear Zoeppritz AVO inversion more than V_P for both cases using PP- and PS-reflections separately. However, the sensitivity is more influenced by density and V_P than V_S, when the AVO input is relatively limited as a near angle range. In addition, observed tradeoff relationships in second columns of Figures B.4 and B.5 imply the difficulty to invert the unique value of the parameters with the limited angle range. Moreover, the uncertainty of the nonlinear AVO inversion to determine the minimum error between modeled and observed AVO dramatically increases, when the AVO input range is limited, It is mainly due to the fact the nonlinearity of the target parameters significantly increases. Therefore, when R_{PP} is only considered as data for the inversion, to increase the AVO input range is necessary in order to decouple V_P, V_S, and density. Although the level of nonlinearity between target parameters in R_{PS} is much higher than the level in R_{PP}, the additional PS-AVO information can reduce the ambiguity to minimize the L^2-norm with the joint inversion approach. In the given sensitivity tests, the joint inversion can successfully define the minima even with the limited AVO angle range.

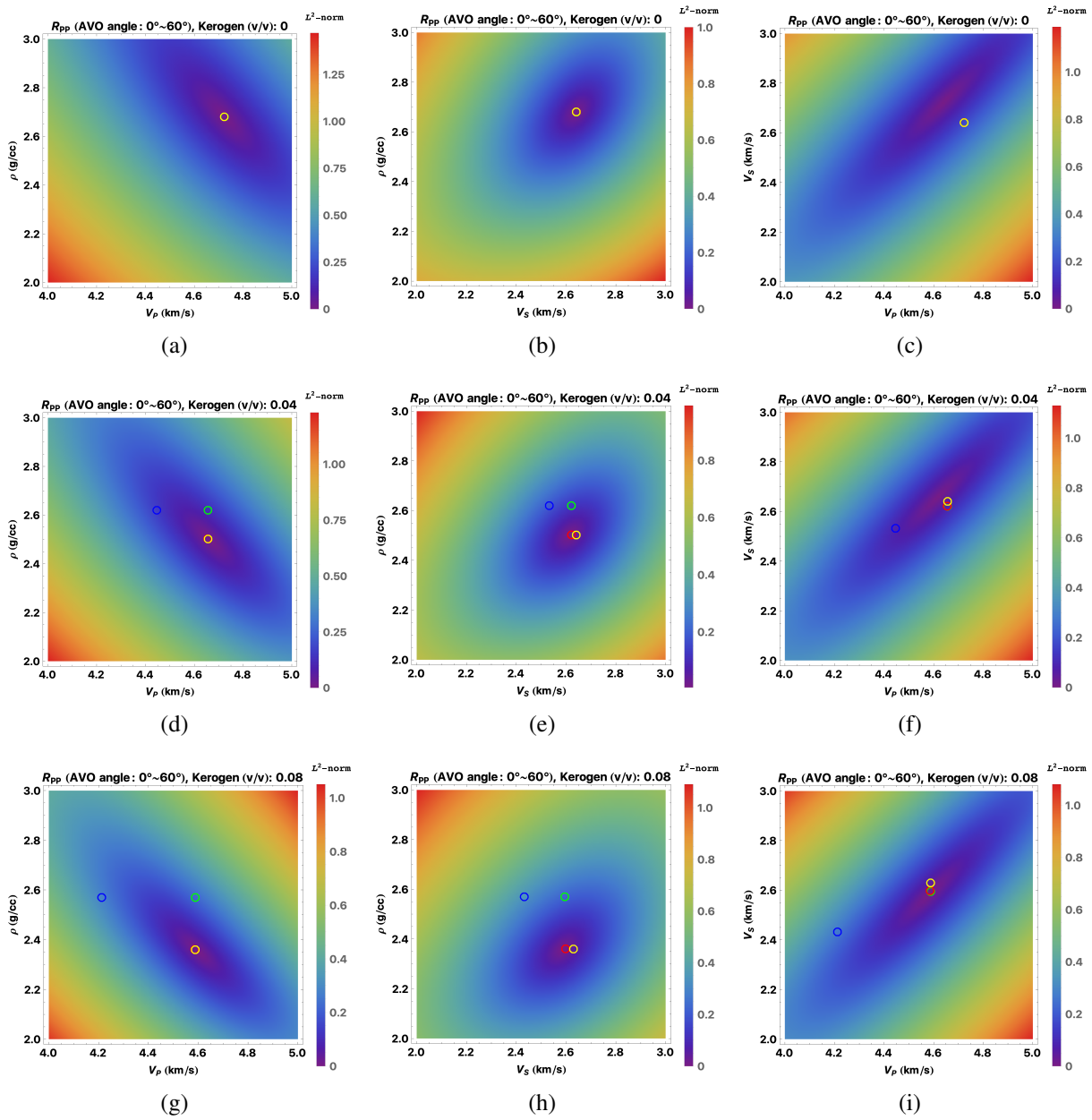

Figure B.1: Density Plot for L^2-norm in equation 3.4. ω is set as 1 in order to consider PP-reflection coefficient (R_{PP}) only, and each column shows the norm for a different pair of parameters. $0^\circ \sim 60^\circ$ AVO input range is applied for the computation. The green and blue circles correspond to horizontal and vertical model values for all the levels of kerogen content, respectively. The red circles indicate inversion results from the proposed nonlinear Zoeppritz AVO inversion using R_{PP} only (i.e., the case that ω is set as 1 in equation 3.4). The yellow circles show the results for join inversion of PP- and PS-reflection coefficients as emphasized in Figure B.3.

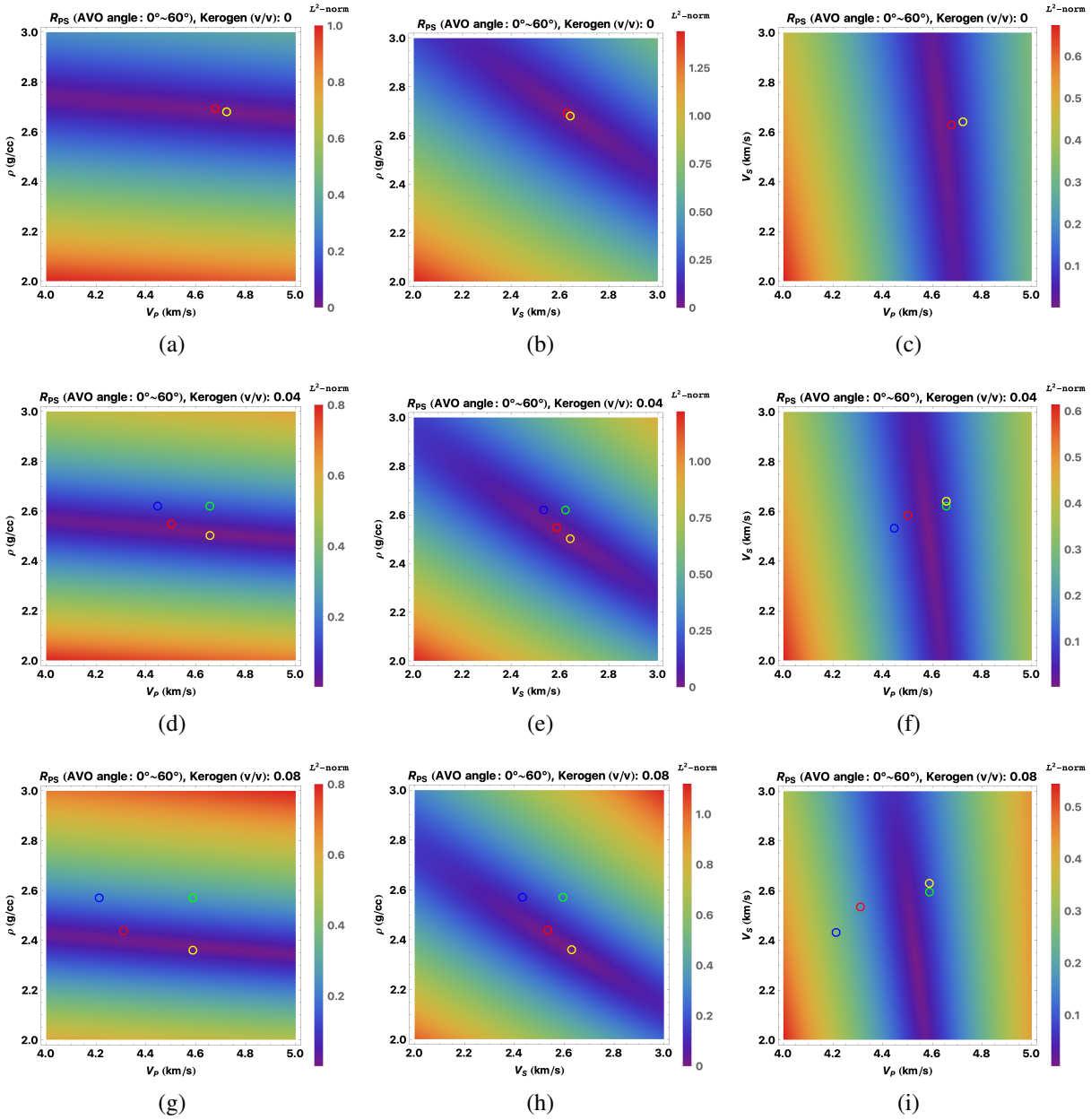

Figure B.2: Density Plot for L^2-norm in equation 3.4. ω is set as 0 in order to consider PS-reflection coefficient (R_{PS}) only, and each column shows the norm for a different pair of parameters. $0^\circ \sim 60^\circ$ AVO input range is applied for the computation. The green and blue circles correspond to horizontal and vertical model values for all the levels of kerogen content, respectively. The red circles indicate inversion results from the proposed nonlinear Zoeppritz AVO inversion using R_{PS} only (i.e., the case that ω is set as 0 in equation 3.4). The yellow circles show the results for join inversion of PP- and PS-reflection coefficients as emphasized in Figure B.3.

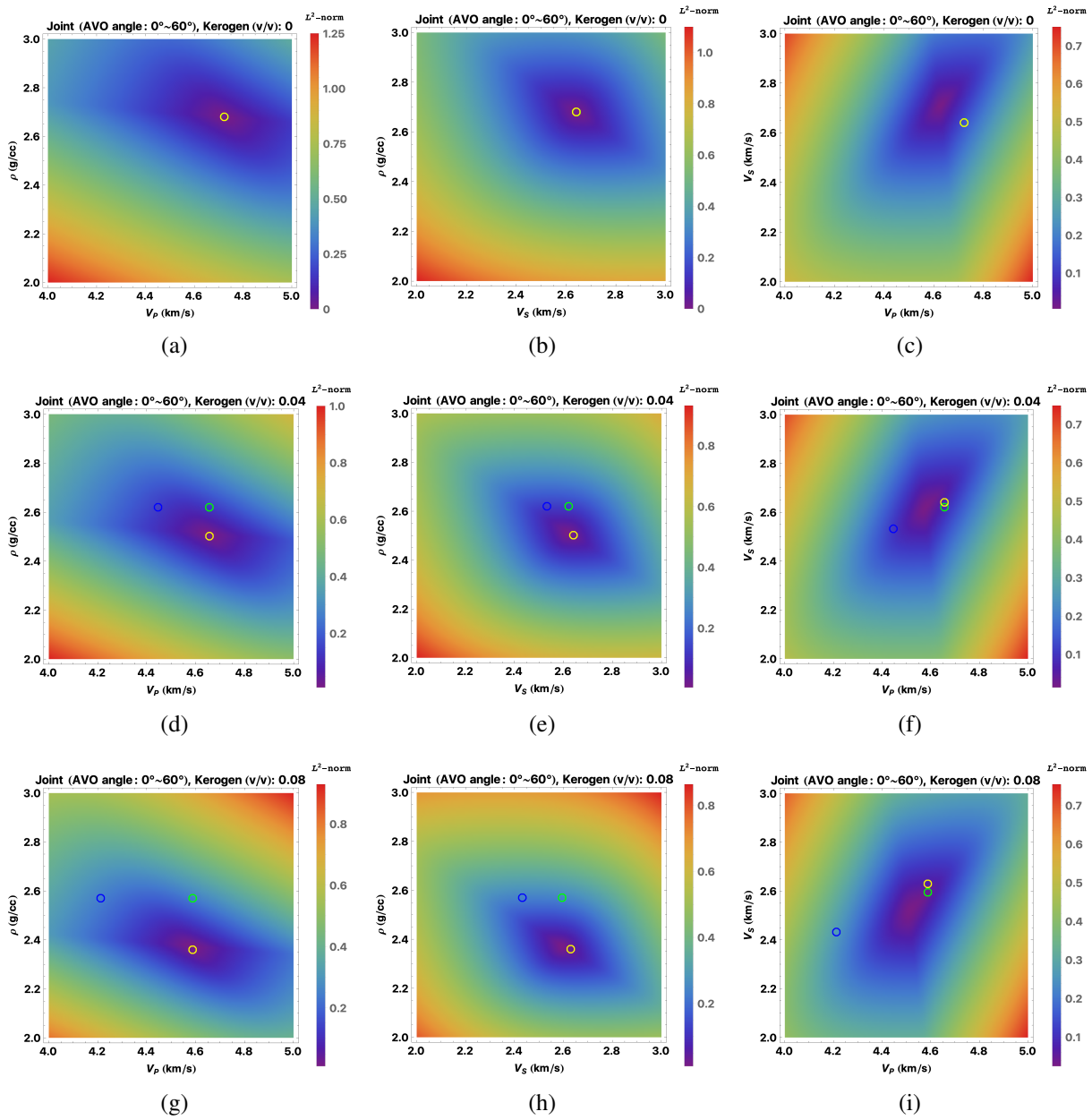

Figure B.3: Density Plot for L^2-norm in equation 3.4. ω is set as 0.5 in order to equally utilize both PP- and PS-reflection coefficients together, and each column shows the norm for a different pair of parameters. $0^\circ \sim 60^\circ$ AVO input range is applied for the computation. The green and blue circles correspond to horizontal and vertical model values for all the levels of kerogen content, respectively. The yellow circles indicate inversion results from the proposed nonlinear Zoeppritz AVO inversion with the joint approach.

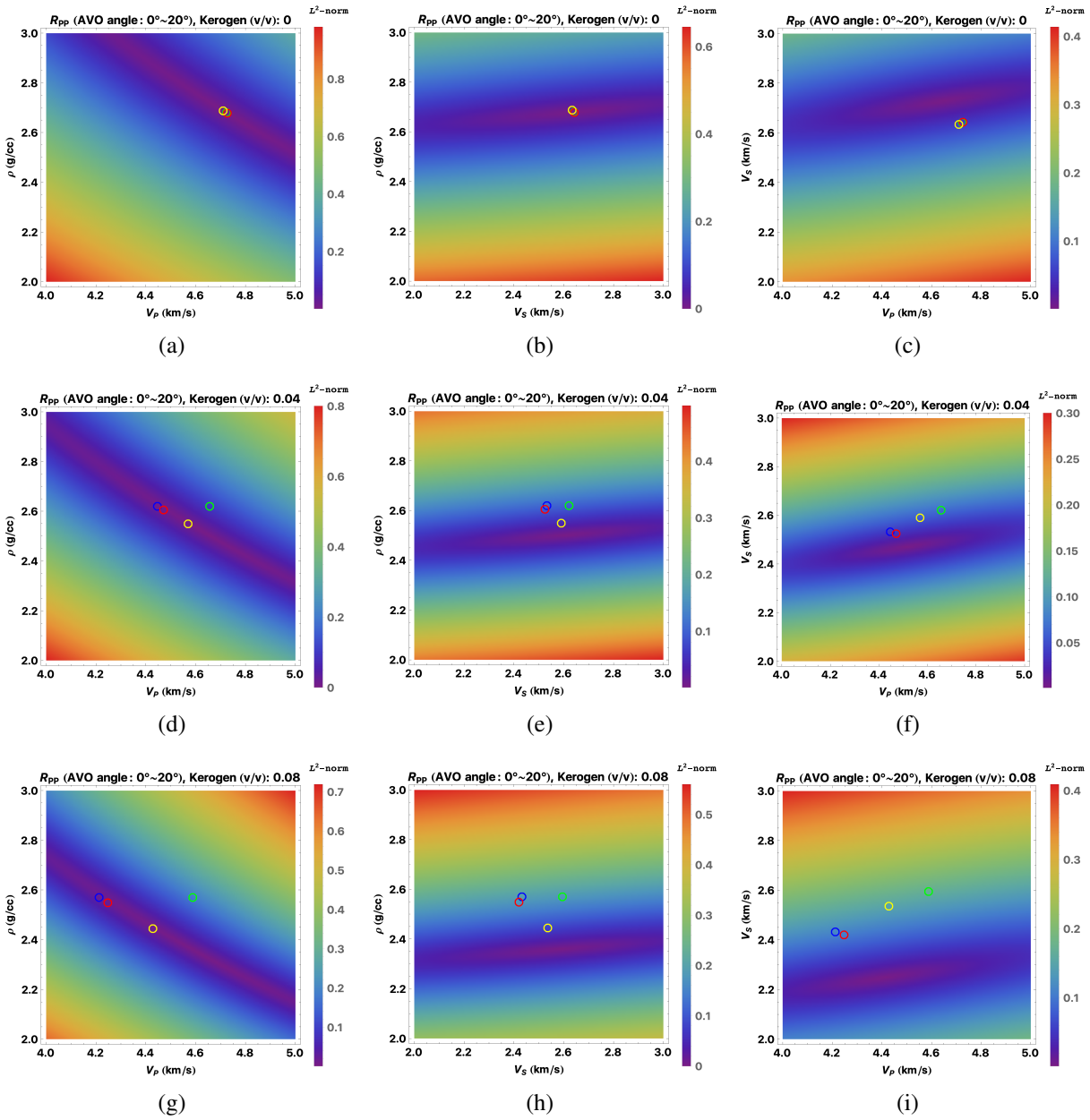

Figure B.4: Density Plot for L^2-norm in equation 3.4. ω is set as 1 in order to consider PP-reflection coefficient (R_{PP}) only, and each column shows the norm for a different pair of parameters. $0^\circ \sim 20^\circ$ AVO input range is applied for the computation. The green and blue circles correspond to horizontal and vertical model values for all the levels of kerogen content, respectively. The red circles indicate inversion results from the proposed nonlinear Zoeppritz AVO inversion using R_{PP} only (i.e., the case that ω is set as 1 in equation 3.4). The yellow circles show the results for join inversion of PP- and PS-reflection coefficients as emphasized in Figure B.6.

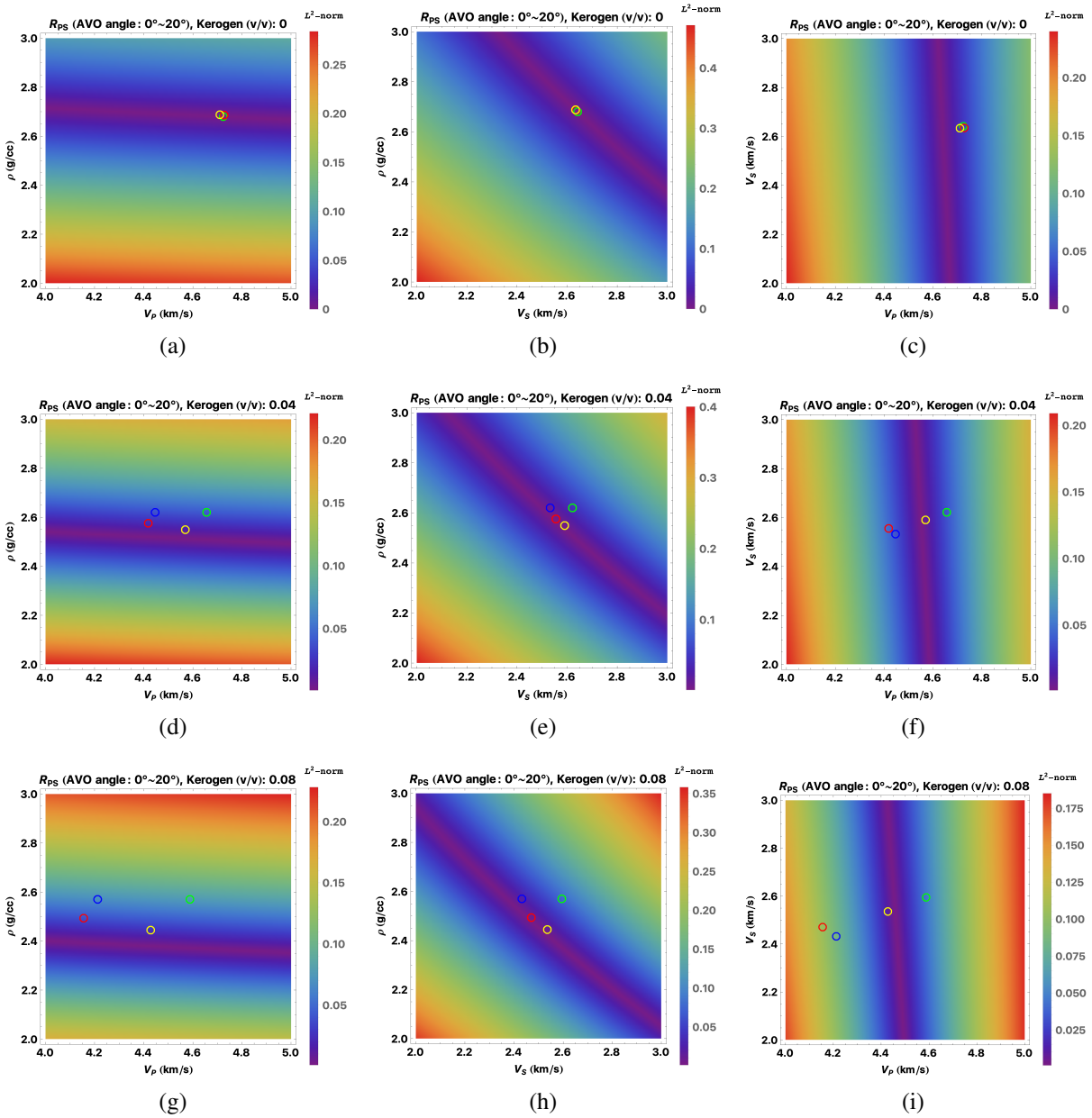

Figure B.5: Density Plot for L^2-norm in equation 3.4. ω is set as 0 in order to consider PS-reflection coefficient (R_{PS}) only, and each column shows the norm for a different pair of parameters. $0^\circ \sim 20^\circ$ AVO input range is applied for the computation. The green and blue circles correspond to horizontal and vertical model values for all the levels of kerogen content, respectively. The red circles indicate inversion results from the proposed nonlinear Zoeppritz AVO inversion using R_{PS} only (i.e., the case that ω is set as 0 in equation 3.4). The yellow circles show the results for join inversion of PP- and PS-reflection coefficients as emphasized in Figure B.6.

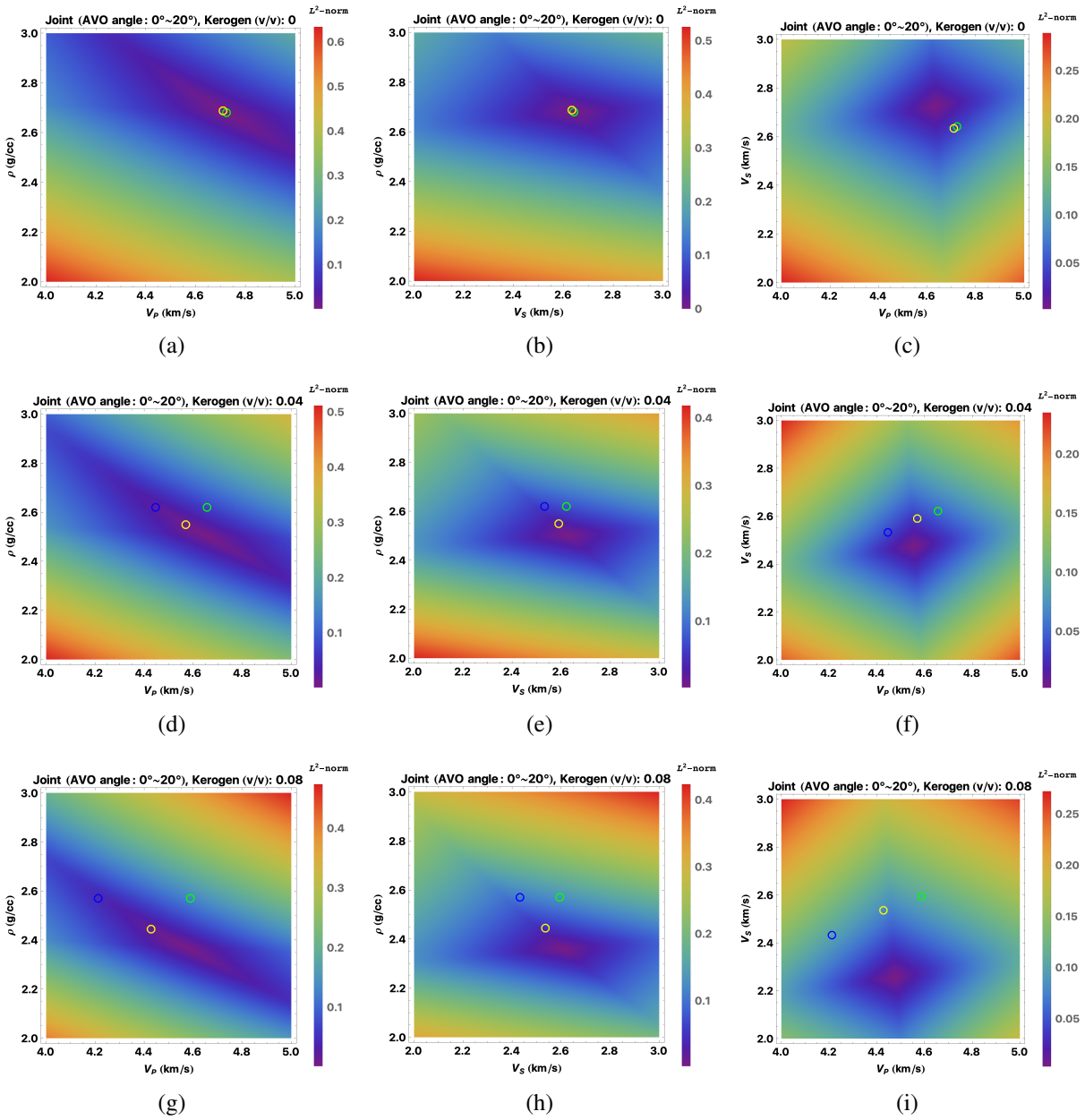

Figure B.6: Density Plot for L^2-norm in equation 3.4. ω is set as 0.5 in order to equally utilize both PP- and PS-reflection coefficients together, and each column shows the norm for a different pair of parameters. $0^\circ \sim 20^\circ$ AVO input range is applied for the computation. The green and blue circles correspond to horizontal and vertical model values for all the levels of kerogen content, respectively. The yellow circles indicate inversion results from the proposed nonlinear Zoeppritz AVO inversion with the joint approach.